UNIVERSITÀ DEGLI STUDI DI PALERMO

Dottorato in Scienze Fisiche
Dipartimento di Fisica e Chimica (DiFC)
Settore Astronomia e Astrofisica (FIS/05)

MHD modelling of plasma flowing in coronal magnetic channels

IL DOTTORE
Antonino Petralia

IL COORDINATORE
Prof. Gioacchino Massimo Palma

IL TUTOR
Prof. Fabio Reale

CICLO XXIX
ANNO CONSEGUIMENTO TITOLO 2017

Contents

Preface

This thesis is devoted to a study of fragmented and continuous flows in a magnetized corona. The corona is the outer part of the solar atmosphere. It is made of million degrees plasma, which is forced to flow along magnetic field channels. The corona is highly dynamic due to the interaction with the underlying photosphere. From this interaction, flows are often generated.

After an important solar eruption, downfalls of plasma onto the solar surface and brightenings around the impact regions have been observed in the EUV band with the Solar Dynamics Observatory. The impact of fragments in regions of weak magnetic field was taken as a template of how accretion flows from circumstellar disks hit the surface of protostars (Reale et al. 2013, Science) and the brightenings were explained by compression and heating of the plasma shocked by the impact. One target of the present thesis is instead to determine what happens to the fragmented flows that hit the surface where the magnetic field is stronger, i.e., nearby active regions. They are observed to be deviated and channelled by the magnetic field and to brighten the related magnetic channel well before they arrive at the surface. It is clear that the brightenings are caused by a different mechanism and that this mechanism is strongly related to the magnetic field.

However, the role of the field is not obvious, in addition to simple channelling. How does it contribute to the brightening? What is the role of the plasma already confined in the channel before the fragments arrive? The thesis addresses this issue, extending the study also to continuous flows propagating in closed coronal structures.

To this purpose, we set up a full 3D MagnetoHydroDynamic (MHD) model of a magnetized corona where flows are injected upwards or downwards. The model includes all the physical effects relevant for an exhaustive description of the plasma dynamics in a magnetized medium, i.e., thermal conduction along field lines, radiative losses, gravity and magnetic induction.

The model is able to reproduce the observation in most of the important aspects, like the partial fading of the falling material and the brightening of the magnetic channel ahead of the fragments. Moreover, with the exploration of the parameter space, the model allows us to probe the physical conditions of the ambient atmosphere in which the material fell. We found that the shocks heat and compress the plasma ahead of the fragments, rising the emission in the magnetic channel, as observed (Petralia et al. 2016, The Astrophysical Journal). An important side effect of the dynamics is that the fragments are completely disrupted by the magnetic field while they are channelled. This is a new issue, never explored before and different from other well-known MHD instabilities: the plasma motion untidily displaces the magnetic field lines which react back and mix the flow. The interplay between these two actions takes place whenever there is a misalignment between the flow velocity and the magnetic field, and the flow is able to perturb the field (Petralia et al. 2017, Astronomy & Astrophysics).

Through MHD modeling we found here that the misalignment also affects the dynamics of a continuous flow moving in a magnetized medium. It is strongly flattened by a curved magnetic field, it becomes laminar, and it is again frayed by the reaction of the field lines. These results are relevant for a wide variety of flows in various astrophysical contexts, from the Sun to the accretion in young stellar objects, and can also have implication in the framework of the solar and stellar winds.

Chapter 1

Introduction

1.1 The Solar Corona

The Corona is the outer part of the solar atmosphere (Fig. 1.1). The solar atmosphere can be generally described with hydrostatic equilibrium, which, on the large scale, determines an exponential pressure stratification. As a result, the pressure decreases with a typical scale height that depends on the local temperature. In turn, the temperature is determined by the local energy balance between heating and losses, where the radiative transfer or losses play an important role. In fact, the temperature falls from the photosphere through the lower chromosphere, before rapidly increasing with height (Fig. 1.2). The temperature of the solar surface detected in the optical band, *i.e., of the photosphere*, is ~ 5800 K. From the photosphere, the temperature grows rapidly with the height. For pressure balance to hold, the density must follow an inverse relation, it rapidly decreases.

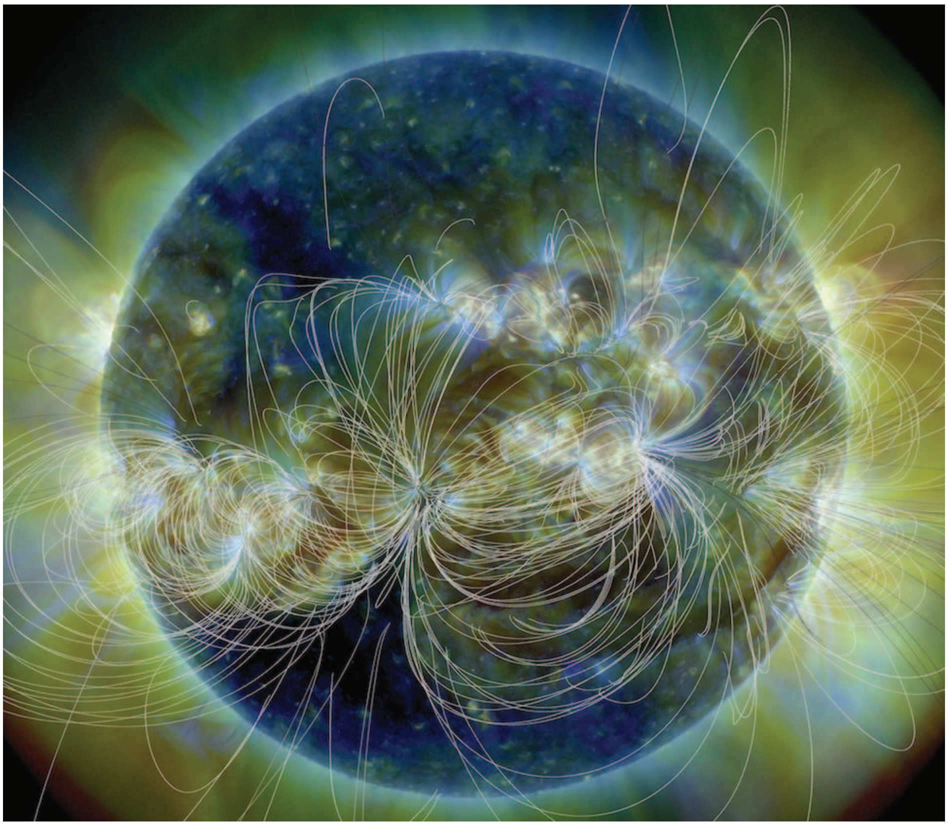

Figure 1.1: Image of the Solar Corona on 7 April 2014, obtained combining different SDO/AIA filter bands (211Å, 193Å, 171Å), in which the extrapolated magnetic field lines are shown (Reale 2014).

Typical values of the temperature are $\sim 10^4$ K in the chromosphere and 10^6 (and greater) in the corona, while the number density ranges between 10^{14} cm^{-3} in chromosphere and 10^9 cm^{-3} in corona. The temperature and the density change with a very steep gradient in a very thin layer of atmosphere, called *transition region*, that links the chromosphere to the corona.

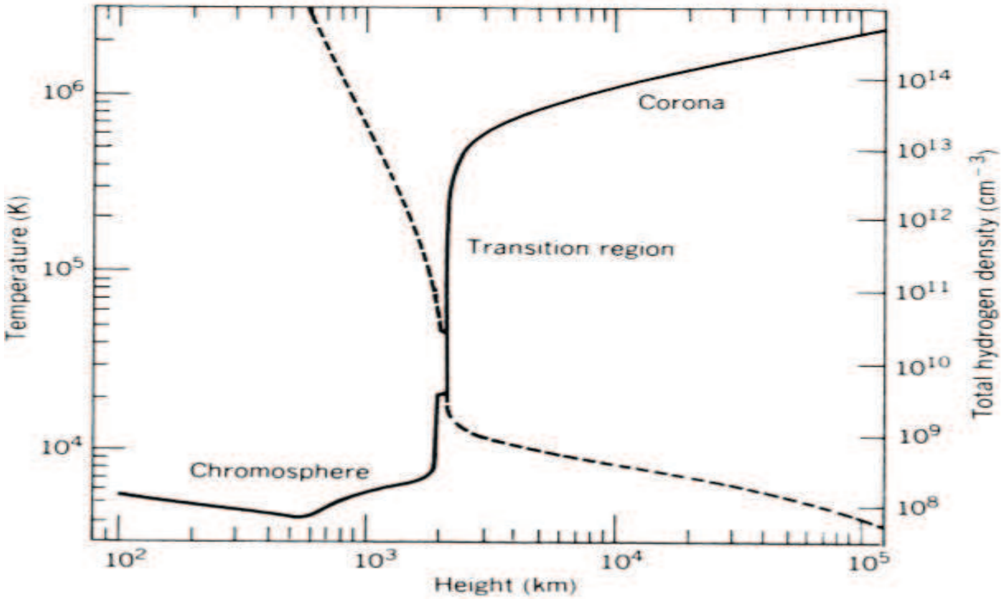

Figure 1.2: Profiles of temperature (solid curve) and density (dashed curve) in the solar atmosphere.

The matter that fills the corona is in a state called *plasma* (see Chapter 2). It is mostly composed by hydrogen whose atoms are fully ionized due to the high temperatures. However, heavier atoms are also present in a partial-ionized state. They are responsible for the emission lines that we observe in the EUV and X-ray energy bands. Observations of the Corona in these bands show that it is highly inhomogeneous due to the presence of the magnetic field. It organises the emission by forcing the plasma to move along its magnetic field lines. The emission comes mostly from closed and complex structures, *the active regions.* They are composed by arch-like magnetic channels anchored to the photosphere, called *loops* (Fig. 1.3). Open magnetic structures are also present.

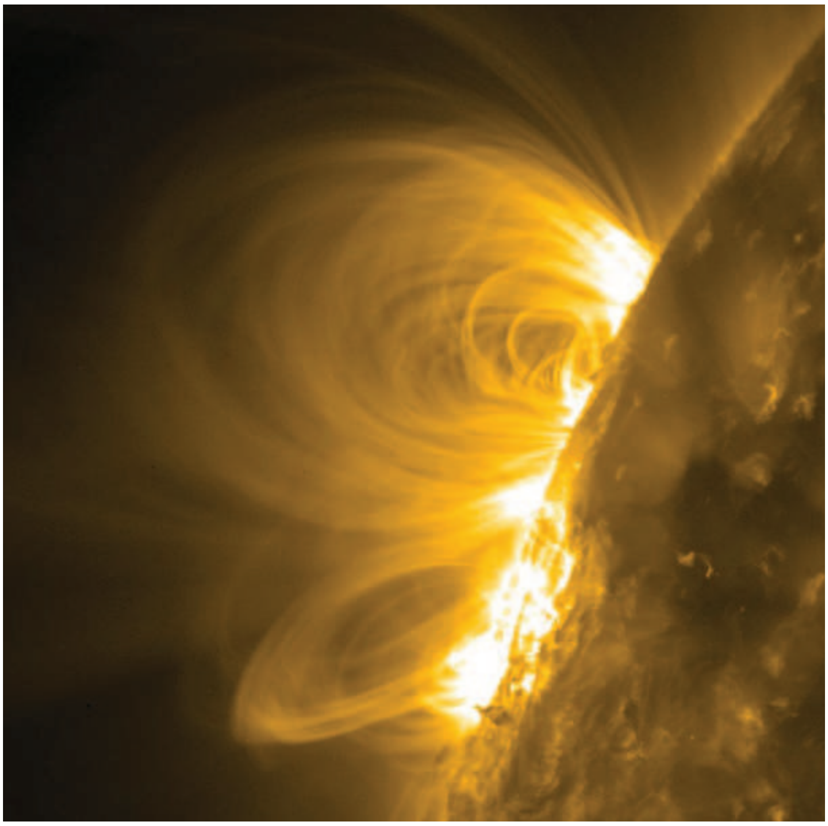

Figure 1.3: Coronal loops observed by SDO/AIA on 24 February 2011 (Reale 2014).

1.2 The dynamism of the Corona: flows

The Corona is not isolated but it interacts with the underlying atmosphere through the magnetic field. The convective motions perturb the magnetic channels and, consequently, the atmosphere above. The magnetic channels can be shifted and/or perturbed by mechanical stresses. This perturbation can drive many different dynamical phenomena by triggering pressure gradients or more violent mechanical 'kicks'. As a consequence, many different kinds of flow can be generated.

1.2.1 Siphon flows

Pressure gradients between the foot-points of loops can drive flows along magnetic channels by pushing upwards the cold and dense chromospherical material. If the gradients are strong enough, the flow, called *siphon flow* (Fig. 1.4), will fill completely the magnetic channel.

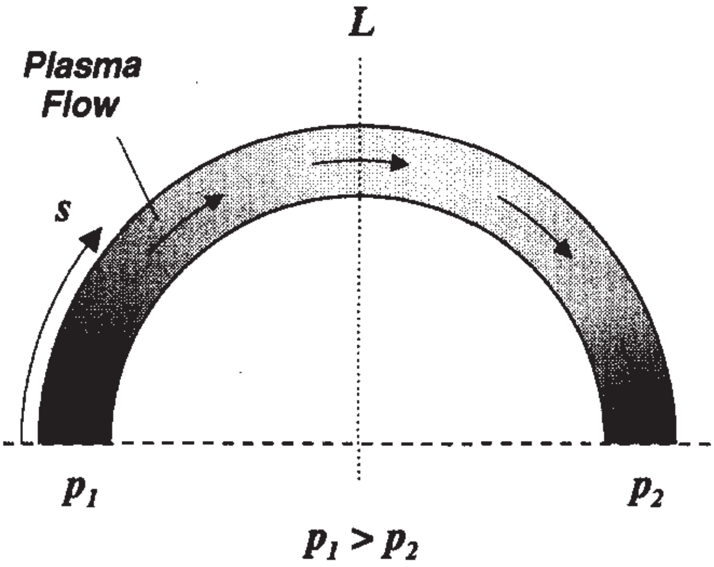

Figure 1.4: Schematic representation of a siphon flow propagating inside a loop (Orlando & Peres 1999).

By studying doppler shifts and images in different energy bands from infrared to EUV several authors reported siphon flows velocities from few km/s up to 130 km/s (Rueedi et al. 1992; Brekke et al. 1997; Mariska & Dowdy 1992; Winebarger et al. 2001, 2002; Teriaca et al. 2004). Siphon flows has been studied to analyse the stability and the properties of the coronal loops (Cargill & Priest 1980; Orlando et al. 1995a,b; Peres et al. 1992; Doyle et al. 2006).

1.2.2 Spicules

If the pressure gradients are small, instead, they can lead to impulsive flows like *spicules* (Beckers 1968; de Pontieu et al. 2007, Fig. 1.5). They are divided in two category, based on their different characteristics, type I and type II spicules. *Type-I* spicules have timescales of $3-7$ minutes, velocity between $10-40$ km/s (Hansteen et al. 2006; De Pontieu et al. 2007) and temperature below CaII (Langangen et al. 2007). *Type-II* spicules are much more dynamic: they last for $10-150$s and have a velocity of order $50-150$km/s (de Pontieu et al. 2007). They are cold (10^4 K) but a small fraction of them has been also observed at coronal temperatures (De Pontieu et al. 2011; Madjarska et al. 2011; Vanninathan et al. 2012). For this reason and because they are very frequent events, it has been proposed that spicules con-

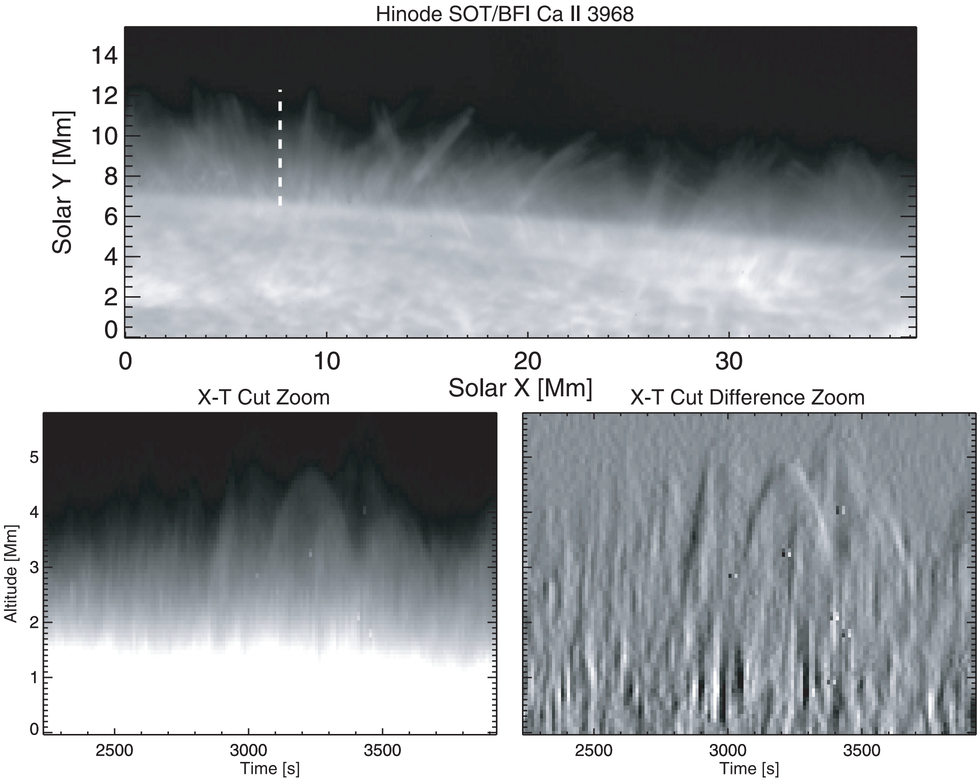

Figure 1.5: (Top) Spicules observed on 2006 November 22, in SOT/BFI Ca II H 3968 data. (Bottom) Space-time (xt) plots along the dashed line in the top panel. The vertical stripes mark the type II spicules while the parabolic paths mark the type I spicules (de Pontieu et al. 2007).

tribute substantially to sustain the high coronal temperatures (Beckers 1968; Pneuman & Kopp 1978; Athay & Holzer 1982; Tsiropoula & Tziotziou 2004; De Pontieu et al. 2009). However, theoretical studies suggested that they can only account for a small fraction of the hot coronal plasma (Klimchuk 2012; Tripathi & Klimchuk 2013; Patsourakos et al. 2014). Shocks have been proposed to explain the evidence of hot plasma associated to the type-II spicules (Petralia et al. 2014). The shocks can heat and compress the coronal ambient plasma ahead of the spicules. Therefore, the rise in the coronal density lead to a rise in the emission ahead of the flow that could explain the observational evidence of hot plasma associated with these events.

1.2.3 Coronal rain

Flows can be also generated by thermal instability (Parker 1953; Field 1965) in the so-called *coronal rain*. In this case, a strong heating at loop foot-points can lead to a high plasma density in loops and therefore to high radiative losses that exceed the heating and cause a catastrophic plasma cooling and condensation along the magnetic field lines.

The plasma condensates in small, dense and cold blobs. During an observation of the solar limb on 2009 May 10, Antolin & Rouppe van der Voort (2012) estimated an average widths and lengths of ~ 300 km and ~ 700 km, respectively, and average temperatures below 7000 K. From different observations, Antolin et al. (2015) estimated the blob densities to vary between 2×10^{10} and 2.5×10^{11} cm^{-3} while the velocity to vary in a broad range. It is limited by the free-fall speed from coronal heights, typical velocity of 60-70 km/s has been found, but greater velocity are also been observed, up to 200 km/s (on 2013 August 30 by Kleint et al. 2014).

1.2.4 Coronal Mass Ejections

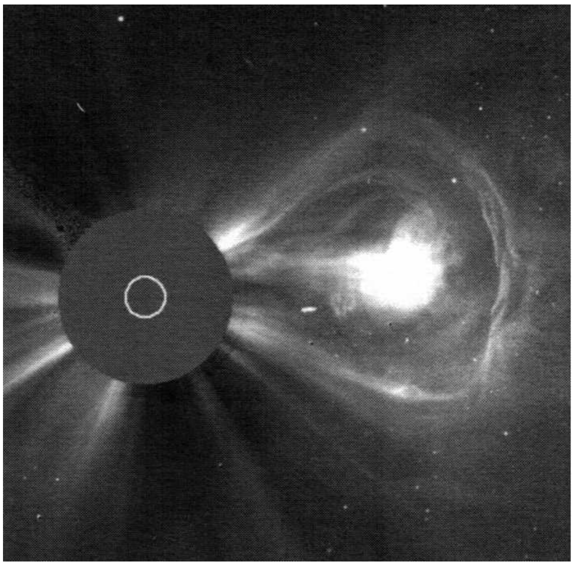

Figure 1.6: Coronal mass ejections observed in 5 July 2004 (Priest pag 64).

Magnetic reconnection can trigger violent solar eruptions that are able to push in the upper atmosphere a great amount of plasma. Depending on its speed, the upflowing plasma can be ejected outside the solar atmosphere in the so-called *Coronal Mass Ejections* (CMEs, Fig. 1.6) (Chen 2011;

Webb & Howard 2012), or it can fall back onto the solar surface.

In CMEs, the amount of the ejected plasma is typically in the range $10^{14} - 10^{16}$ g, while the velocities can be greater than 2000 km/s. CMEs generally are made of three components: an outer shell of fast plasma, a cavity within the shell, and a core where often an erupting prominence is located. The most of the upwarding plasma is in the core. Its density and temperature can vary in a very large range. As an example, the density and temperature diagnostics of a CME observation on 2008 April 9 (Landi et al. 2010), reported two upwarding components in the core in different physical conditions: a cold and dense one with a temperature (T) of $\sim 1.3 \times 10^5$ K and density (Ne) $\sim 10^{11}$ cm^{-3} , and a hotter and less dense one with respectively T $\sim 5 \times 10^5$ K and Ne $\sim 5 \times 10^8$ cm^{-3}. These two separate components are typical observed in these kind of events but with different size and shape (Kohl et al. 2006).

1.2.5 Downflows

In the case the plasma falls onto the solar surface, it can have very different physical properties. An example of downfalls is the back-falling of a large amount of plasma after a solar eruption on 07 June 2011. Authors reported on the density of the falling material to be in a range $1-10 \times 10^{10}$cm^{-3} while the velocities can reach 450 km/s (Carlyle et al. 2014; van Driel-Gesztelyi et al. 2014; Innes et al. 2012; Reale et al. 2013, 2014). While many fragments shown a parabolic path, typical of the free-fall, (Reale et al. 2013, 2014), others show a magnetic field guided motion during their flight (Innes et al. 2012; Carlyle et al. 2014; van Driel-Gesztelyi et al. 2014; Dolei et al. 2014). This variety reflects the highly structuring of the Solar Corona, fragments propagating in different regions can show a very different dynamics and, thus, emission properties. The impacts of fragments in region where the magnetic field is weak showed strong EUV brightenings (Reale et al. 2013, 2014). This emission comes from shells of the dense fragments that are shocked by a bounce back flow while they are still falling.

When the fragments fall near active regions, they show a different dynamics. They are channelled by intense magnetic fields that cause deviations of their trajectories from the parabolic paths. An interesting feature of this process is that the magnetic channels become bright during the channelling and well before the fragments impact the chromosphere. An explanation of this process has not been given yet.

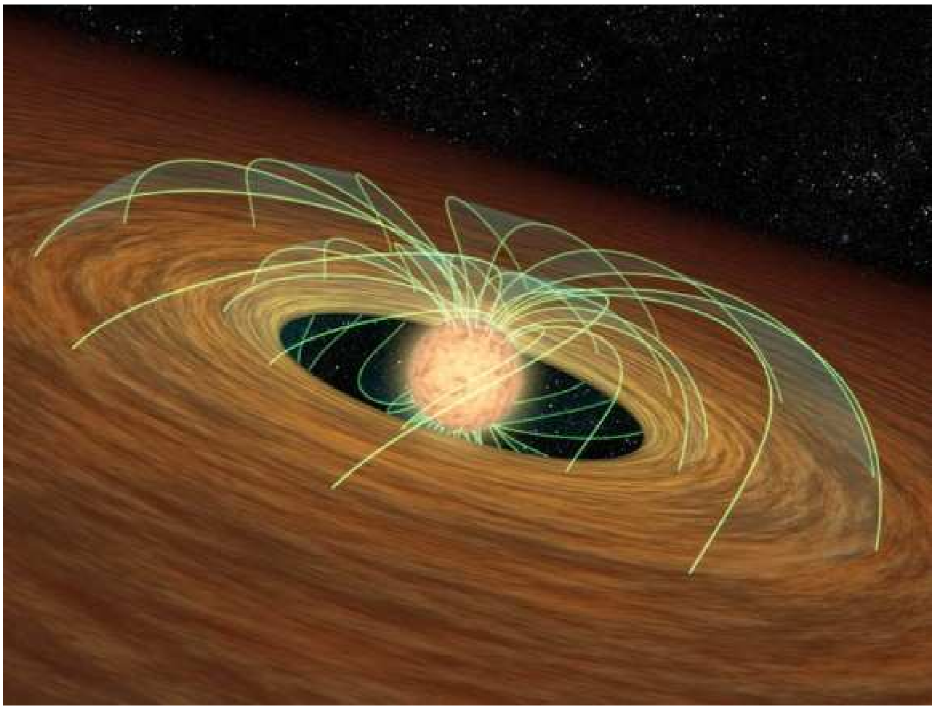

Figure 1.7: Cartoon of a Young stellar object surrounded by a disk, in which the magnetic field lines are shown. Credit: NASA/JPL-Caltech/R (http://www.universetoday.com/86920/slowing-down-stars/)

Downflows as template for the stellar accretion

These EUV brightenings observed when the plasma impacts the solar surface recall the excess of emission in EUV and soft X-ray energy bands observed in young stars. These stellar objects have a strong magnetic field that links a surrounding disk to the central star (Fig. 1.7). It's well accepted that the material from the disk flows along magnetic field channels until it impacts onto the stellar surface (Uchida & Shibata 1984; Bertout et al. 1988), with velocities in the range $\sim 200-600$ km/s.

Observations of these young stellar objects show that part of the emission comes from dense and cold plasma, with a density in the range $10^{11}-10^{13}$ cm^{-3} and a temperature in the range $2-6$ MK (Kastner et al. 2002; Telleschi et al. 2007; Argiroffi et al. 2007, 2011; Testa et al. 2004; Schmitt et al. 2005; Günther et al. 2006; Huenemoerder et al. 2007; Robrade & Schmitt 2007). Due to its higher density, this component can not be confined by the magnetic field in coronal closed structures and it has been proposed that this component is due to the shocks that are formed when the cold plasma hits the stellar surface. They heat up the accretion column to temperatures of few MK (Gullbring 1994; Lamzin 1998), as many observation suggest (Edwards et al. 1994; Calvet & Gullbring 1998; Gullbring et al. 2000; Ardila et al. 2002; Herczeg et al. 2005).

1D modelling is able to establish that the soft X-ray emission comes from the base of the accretion column where the shocks heats the dense material coming from the disk (Argiroffi et al. 2007; Koldoba et al. 2008; Sacco et al. 2008). All these 1-D models assume that the plasma moves and transports energy only along magnetic field lines. This hypothesis is valid if the stellar magnetic field in the proximity of the impact regions is strong. In case of stars with photospheric magnetic field of 1 kG (e.g. Johns-Krull et al. 1999), the field is strong enough to efficiently confine accretion shocks with particle density below 10^{13} cm^{-3} and the temperature around 5 MK. However, in some cases, the magnetic field can be much weaker, less than 200 G (Valenti & Johns-Krull 2004) and the plasma moves and transport energy across the field. Therefore, the magnetic field configuration can be influenced and can influence the dynamics of the accreting material and of the shocks. 2D MHD models (Orlando et al. 2010, 2013; Matsakos et al. 2013; Colombo et al. 2016) show that the accretion dynamics can be complex and the atmosphere around the impact region can be strongly perturbed by leaks at the border of the main stream (Fig. 1.8, Orlando et al. 2010), as observations suggest (Brickhouse et al. 2010; Dupree et al. 2012), leading to the need of more complex and 3D models.

Here we focus on fragments falling high from regions where the magnetic field is very weak and eventually channelled by the stronger lower field. This process cannot be modelled with a 1D channelling only. A 2D description, either cylindrical or cartesian, cannot account for discrete fragments which deviate while they travel. In this situation the only symmetry we have can be a reflecting one with respect to a plane perpendicular to the solar surface, and a fully 3D description is due. The extrapolation to stellar accretion is not trivial, but one can certainly imagine a loose confinement on the disk where the flow starts and the field is weak, and a much tighter one close to the impact region.

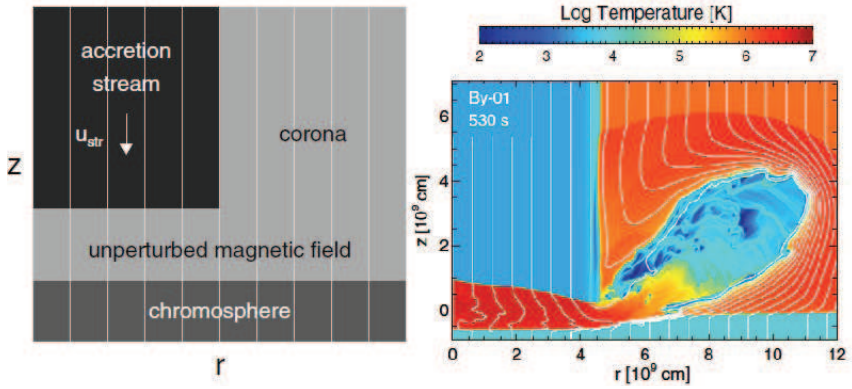

Figure 1.8: Simulation of impacts in young star objects (Orlando et al. 2010). Left: schematic view of an accretion stream impacting a stellar surface. Right: temperature map after the impact of the stream onto the dense chromosphere. The white lines are magnetic field lines. With this configuration and parameters, the impacting shocked material leaks at the base of the accretion column and strongly perturbs the surrounding stellar atmosphere.

1.3 Outline of the thesis

In this thesis, we study the propagation of cold and dense plasma in a magnetized medium. In general, We focus the attention on the downfalls of fragments of plasma near active regions and cold flows propagating in closed magnetic field structures. Thus, the core of the thesis is the study of the interaction between the magnetic field and the propagating plasma, and the way this interaction characterizes the dynamics of the plasma. During his PhD program, Antonino Petralia has spent two months at the University of St.Andrews, under the supervision of Prof. Alan Hood. There, A. Petralia had the opportunity to study the theory and modeling of MHD force-free equilibria (Chapter 2, section 2.3) and MHD instabilities in the framework of his PhD topics regarding coronal magnetized flows.

After a spectacular solar eruption in 2011, many dense fragments were observed to fall back onto the solar surface in a large region far from the eruption place. Many impacts produced brightenings in the EUV band detected with the Atmospheric Imaging Assembly on-board the Solar Dynamics Observatory. Previous works studied impacts in quiet Sun regions (e.g., Reale et al. 2013), in Chapter 3 we address the fragments of plasma that fall near active regions. These fragments show a different evolution and destiny. In particular, we no longer see bright impacts but the fragments are deviated, channelled and the whole final segment of the channels is activated into bright thinner filaments. It is clear from the observations that here the magnetic field plays a different and critical role in determining the evolution of the blobs and, thus, the mechanism that produces the excess of the emission is not necessary the same as in the case of the falling fragments in Quiet Sun, where the field is weak. So it is interesting to explore these cases in which the interaction of the blobs with the magnetic field is important. Our approach is similar to that of Reale et al. (2013) though here we included the description of an appropriate ambient magnetic field and therefore a full 3D magnetohydrodynamic model. The fragments do not follow a simple trajectory but they are deviated as they move deeper and deeper in the low corona, confirming a non-trivial interaction with the more and more intense magnetic field. Another different and fundamental ingredient is that the downfalling fragments are eventually forced to propagate inside an already dense and hot medium, that is the plasma confined inside active region loops. This plasma is strongly perturbed and activated by the infalling material, which then acts also as a probe for the ambient corona. This case represented a unique opportunity to probe active region conditions and their reaction to strong perturbations coming from outside. On the other hand, this is also closer to the conditions in star forming regions, where the flows coming from the circumstellar disk are believed to be funneled by the magnetic channels that link the disk to the young stars. The work presented in this Chapter is the subject of a publication in the Astrophysical Journal (Petralia et al. 2016).

The model presented in Chapter 3 shows that the interaction of the plasma with the field is not trivial. An interesting feature concerns the integrity and shape of the fragments. According to the model the plasma blobs are warped and further fragmented as soon as their interaction with the field becomes significant. It is clear that the plasma is conditioned by the field and the field by the plasma. In Chapter 4, we investigated the key conditions to trigger this interaction and to determine a significant disruption of the blobs. To this purpose, we compared two similar MHD simulations, one showing, the other not showing this effect. The main result of this work is that a significant disruption and fine structuring of the blobs flowing inside magnetic channels is determined whenever the speed of the blobs is not perfectly aligned to the field lines and the field is not very strong. In this case the field lines are bent out of equilibrium and shuffle back the plasma when they bounce back to restore the equilibrium. This is a new mechanism to disrupt plasma drafts, different from proper MHD instabilities, and is the subject of a publication in the Astronomy & Astrophysics (Petralia et al. 2017).

As a further extension of this work, in Chapter 5 we studied the propagation of continuous flows which travel all along closed magnetic channels. EUV observations (e.g. http://www.lmsal.com/hek/her?cmd=view-voevent&ivorn=ivo://helio-informatics.org/ERMET_KarelSchrijver_20151105_214937) showed some flows that end up in a flat hedge-like configuration and the explanation is not obvious. Also in this case it is interesting to investigate a possible role of the initial alignment or misalignment of the flow motion with respect to the field lines. We address this issue by modelling flows which are pushed upward from the chromosphere along closed magnetic flux tubes in the corona. We compared 3D MHD simulations of continuous flows which are either perfectly aligned to the field or not. These simulations showed that, while aligned flows move mostly undisturbed along the tube, misaligned flows are significantly flattened while they travel along the flux tube, thus providing a possible explanation of the observational evidence. This work will be the subject of a forthcoming article.

We used the state-of-art PLUTO MHD code (Mignone et al. 2007, 2012, see also Appendix A), developed at the University of Turin, and ran it on High Performance Computing systems, the FERMI and the MARCONI at CINECA, Italy, and the Pleiades at NASA/USA through approved peer-reviewed HPC projects (ISCRA B and C class) and on the local SCAN facility of the INAF - Osservatorio Astronomico di Palermo.

Chapter 2

Plasma physics

2.1 Plasma properties

The particular combination of temperature and particle density in the corona leads to the need, in most situations, to treat the gas as a *plasma*. This term is used to describe a state of the matter in which the neutral atoms are separated into charged components and the electromagnetic interaction between them must be considered. At the same time, the particle number is so great that the particles equations can be solved considering the assembly of particle as a fluid by taking averages of the physical variables.

2.1.1 The plasma approximation

There are two basic parameters that determine whether the treatment of the gas as a plasma is a good approximation: The *Debye length* and the *plasma parameter*. The former indicates the distance scale over which the plasma can readily adjust to a perturbation in the charge distribution, and the latter is a measure of the number of particles in a volume having a radius of the Debye length. If the this number is $\gg 1$ average values can be considered and the gas can be described as a fluid. The Debye length can be easily calculated considering that the potential of a charged particle in the fluid is modified, by the presence of the other charged particles, to

$$\phi(r) = \frac{a}{r} exp(-\frac{r\sqrt{2}}{L}) \tag{2.1}$$

where a is a normalization constant, and L is the Debye length given by

$$L = \lambda_D = \sqrt{\frac{k_B T}{4\pi n_e e^2}} [cm] \tag{2.2}$$

where k_B is the Boltzmann constant, T is the gas temperature, n_e is the electron density, e is the electron charge. This result shows that the charge distribution rearranges itself, in the presence of a small perturbation, such that the potential no falls exponentially, longer as $\frac{1}{r}$. This means that the Debye length can be considered as the length over which the potential is screened. If T is given in K, electron density in cm^{-3} and the Debye length in cm, then

$$\lambda_D = 6.9\sqrt{\frac{T}{n_e}} \quad [cm] \tag{2.3}$$

In coronal active regions, typical values for temperature and density are, respectively, 3×10^6K and 5×10^9 cm^{-3} (Keenan et al. 1996) and the Debye length is ~ 0.17 cm. For comparison, the smallest coronal structure currently resolved is of the order of 10^7 cm. Now the plasma parameter (Δ) can be obtained by consider

$$\Delta = n_e {\lambda_D}^3 \tag{2.4}$$

which is of the order of 10^7, in coronal active region, that is of course $\gg 1$.

An other important aspect is the comparison between the electromagnetic interaction (ω_{mag}) and collisions (ω_{col}) frequencies. When $\omega_{mag} > \omega_{col}$, the gas shows a collective behaviour (Chen 1984), and this is the case for the coronal plasma in which the ratio $\frac{\omega_{mag}}{\omega_{col}}$ is $\sim 10^8$. Moreover, typical coronal structures (the loops) are much larger than the mean free path for the single particle ($\sim 10^7$cm), therefore the plasma, in these structures, can be considered as in thermal equilibrium.

2.2 Magneto-Hydrodynamics Equations

Plasma in the confined corona can be described as a magnetized fluid. The related equations are the Magneto-Hydrodynamics (MHD) equations, here in the conservative forms in c.g.s.. They include the conservation of the mass

$$\frac{\partial \rho}{\partial t} + \nabla \cdot (\rho \mathbf{v}) = 0 \tag{2.5}$$

where ρ is the plasma density (g/cm^3) and $\mathbf{v}$ is the velocity, and t is the time.

The equation of momentum:

$$\frac{\partial \rho \mathbf{v}}{\partial t} + \nabla \cdot (\rho \mathbf{v}\mathbf{v}) = -\nabla p + \frac{\mathbf{j} \times \mathbf{B}}{c} + \rho \mathbf{g} \tag{2.6}$$

where $\mathbf{j}$ is the current density, $\mathbf{B}$ is the magnetic field, and $\mathbf{g}$ is the gravity in the solar atmosphere.

The energy equation:

$$\frac{\partial u}{\partial t} + \nabla \cdot ((u+p) \cdot \mathbf{v}) = \rho \mathbf{g} \cdot \mathbf{v} - n^2 Q(T) + H - \nabla \cdot \mathbf{F}_c + \frac{\mathbf{j} \times \mathbf{B}}{c} \cdot \mathbf{v} \tag{2.7}$$

where H is the function that describes the heating input, Q(T) is the radiative losses function, $\mathbf{F}_c$ is the conduction flux and u is the energy density given by

$$u = \frac{1}{2}\rho v^2 + \frac{p}{(\gamma - 1)} \tag{2.8}$$

where γ is 5/3, and p is given by the perfect gas law for a fully ionized plasma:

$$p = 2 n_e K_b T \tag{2.9}$$

where n_e is the electron density ($particles/cm^{-3}$), K_b is the Boltzmann constant and T is the temperature of the plasma, with n_e equal to the density number of hydrogen ions n_i.

To the previous equations, we add the Maxwell equations:

$$\nabla \times \mathbf{B} = \frac{4\pi}{c}\mathbf{j} + \frac{1}{c}\frac{\partial \mathbf{E}}{\partial t} \tag{2.10}$$

$$\nabla \cdot \mathbf{B} = 0 \tag{2.11}$$

$$\nabla \times \mathbf{E} = -\frac{1}{c}\frac{\partial \mathbf{B}}{\partial t} \tag{2.12}$$

$$\nabla \cdot \mathbf{E} = 4\pi\rho^* \tag{2.13}$$

where $\mathbf{E}$ is the electric field and ρ^* is the charge density. Moreover, we have to consider the Ohm law:

$$\mathbf{j} = \sigma(\mathbf{E} + \frac{\mathbf{v} \times \mathbf{B}}{c}) \tag{2.14}$$

where σ is the electrical conductivity of the plasma. Combining opportunely the previous equations we can write the induction equation

$$\frac{\partial \mathbf{B}}{\partial t} = \nabla \times (\mathbf{v} \times \mathbf{B}) + \eta\nabla^2\mathbf{B} \tag{2.15}$$

where η is the magnetic resistivity, given by $c^2/4\pi\sigma$. In the right hand side of this equation there are two terms. The former is the advective term, while the latter is the diffusive term. To determine the relative importance of the two terms, one can introduce a parameter, the magnetic Reynolds number:

$$R_m = \frac{l_0 v_0}{\eta} \tag{2.16}$$

where l_0 e v_0 are respectively the characteristic length and the velocity of the system. When $R_m >> 1$ the diffusive term can be neglected, alternatively, when $R_m << 1$ it is the advective one that can be neglected (Priest 2014). In the solar corona $R_m \sim 10^{14}$ (Spitzer 1962), the plasma is perfectly conductive and the Alfvén theorem holds, by which the plasma is frozen to the magnetic field lines (Alfvén 1942) and the current density $\mathbf{j}$ can be written as

$$\mathbf{j} = \frac{c\nabla \times \mathbf{B}}{4\pi}. \tag{2.17}$$

2.3 Magneto-statics

Observations of coronal loops (Reale 2014) show that these magnetic field structures are often stable/static. In active regions, the magnetic field is so strong that it dominates over other forces such as pressure or gravity, so it can be considered static if the Lorentz force vanishes, i.e. $\mathbf{j} \times \mathbf{B} = 0$, where $\mathbf{j}$ is given by eq. 2.17. The fields that satisfy this condition are called *force-free*, while in the particular case in which j is 0 they are called *current-free* or *potential fields*. In general, in force-free fields, the current density $\mathbf{j}$ is parallel to the magnetic field and using eq. 2.17, one can obtain

$$\nabla \times \mathbf{B} = \alpha \mathbf{B} \tag{2.18}$$

where α is a constant, equal to 0 in current-free fields. This difference gives different geometrical properties as we show in Fig. 2.1.

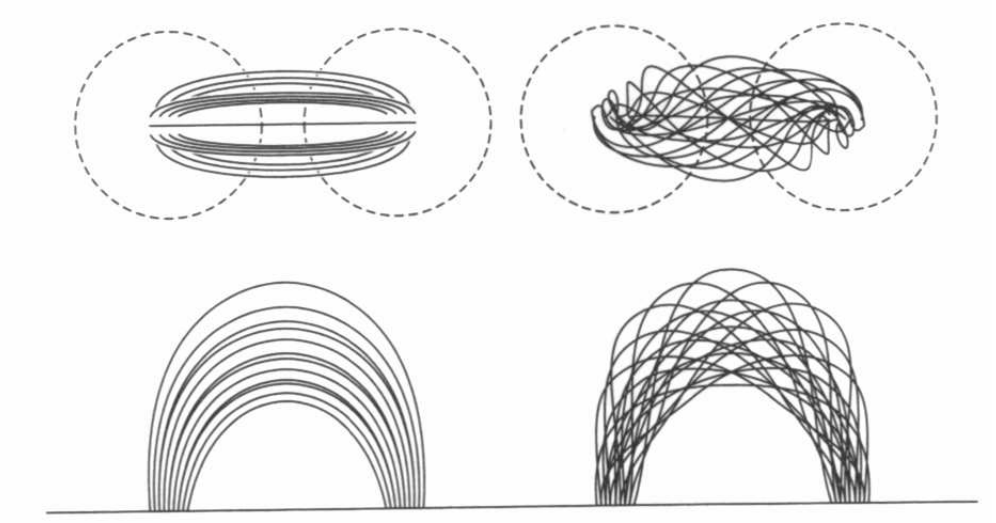

Figure 2.1: Schematic view of a loop in which the magnetic field is current-free (left) and force-free (right) (Priest 2014).

2.3.1 Magneto-static conditions

Equation 2.18 can be solved analytically (Priest 2014, and references therein) or numerically (e.g. Finn et al. 1994; Mackay et al. 1999, and references therein).

An example of a simple and analytical current-free solution is the Dipole magnetic field whose the expression is given by

$$\mathbf{B}(\mathbf{r}) = \frac{\mathbf{m} \times \mathbf{r}}{r^3} \tag{2.19}$$

where $\mathbf{m}$ is the magnetic moment and $\mathbf{r}$ is the distance from the center of the dipole. As an example of the numerical approach, we propose the method introduced by Mackay et al. (1999). It derives a magnetic field configuration closed inside a cubic box $(-L < X, Y, Z < L)$. To achieve such field, it solves equation 2.18 in terms of vector magnetic potential $\mathbf{A}$ ($\mathbf{B} = \nabla \times \mathbf{A}$)

$$\nabla^2 \mathbf{A} + \alpha \nabla \times \mathbf{A} = 0. \tag{2.20}$$

It requests that the gradient of the perpendicular components of A to the box boundaries is zero ($\nabla A_\perp = 0$) as well as for the parallel components ($A_\parallel = 0$) except for the bottom boundary of the box ($Z = -L$). At this boundary, the parallel component is evaluated by supplying the Z component of magnetic field. The last condition and the fact that α is a tunable parameter make the method flexible in deriving any desired (closed) magnetic field configuration. In Fig. 2.2 we show an example of magnetic field topology that can be obtained by this method.

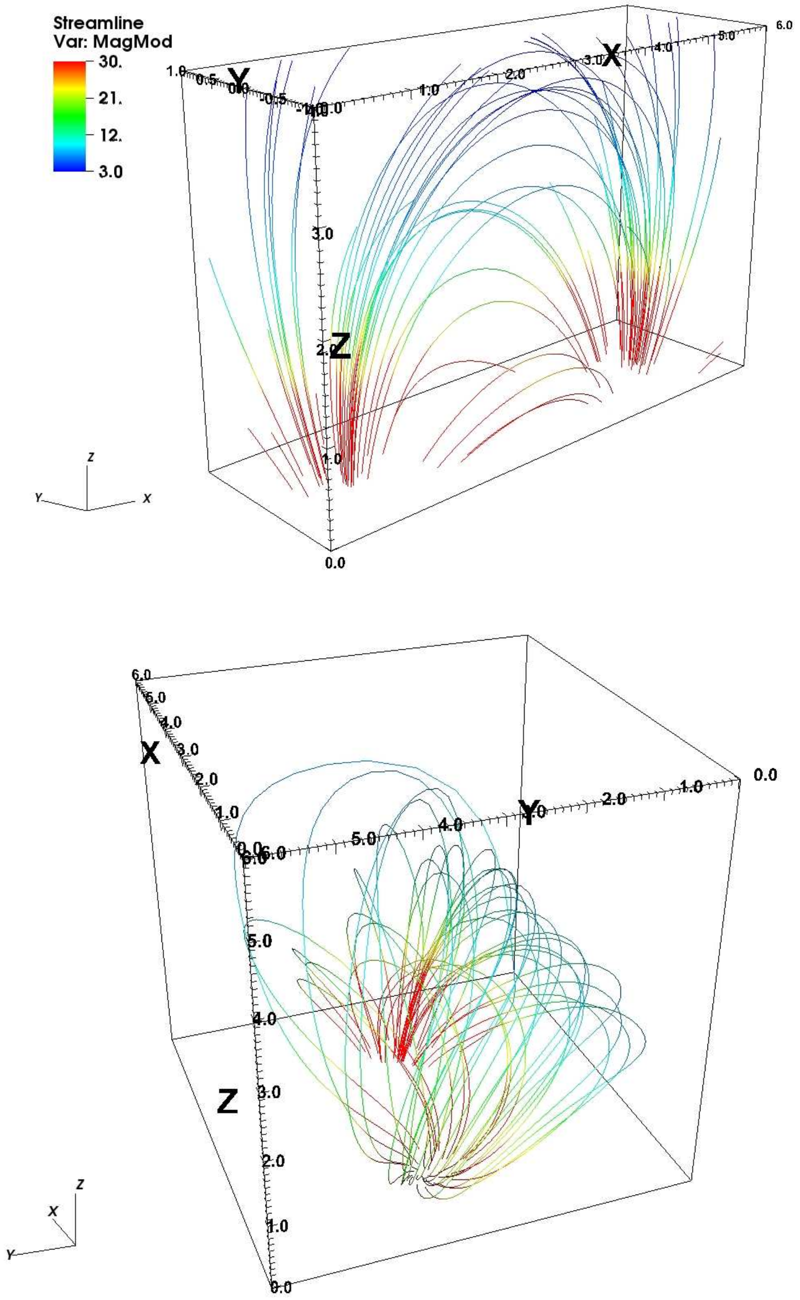

Figure 2.2: Magnetic field lines of a current-free field (top panel, analytical expression for a magnetic dipole) and a force-free field (bottom panel, numerical solution obtained through the method of Mackay et al. (1999)).

2.4 Thermal Conduction

The conductive flux can be written as

$$\mathbf{F}_c = -\mathbf{k}\nabla T \tag{2.21}$$

where **k** is the thermal conduction tensor. The presence of the magnetic field allow us to split the divergence of the conduction flux in two terms,

$$\nabla \cdot \mathbf{F}_c = \nabla_{\parallel} \cdot (k_{\parallel}\nabla_{\parallel}T) + \nabla_{\perp} \cdot (k_{\perp}\nabla_{\perp}T) \tag{2.22}$$

where the subscripts $\parallel$ and $\perp$ refer to the magnetic field direction. For a fully ionized hydrogen plasma, the conduction along the magnetic field is primarily by electrons (Spitzer 1962)

$$k_{\parallel} = k_0 T^{\frac{5}{2}} = 1.8 \times 10^{-10}\frac{T^{\frac{5}{2}}}{ln\Delta} \quad Wm^{-1}K^{-1}. \tag{2.23}$$

Typical values of k_0 are, respectively, 4×10^{-11}, 10^{-11},9×10^{-12} for photospheric, chromospheric and coronal regions. The conduction across the magnetic field is mainly by the protons, depending on the product $\Omega_i\tau_{ii} = 1.63 \times 10^{15} BT^{\frac{3}{2}}/(nln\Delta)$ of the ion gyro-frequency Ω_i and the ion-ion collision time τ_{ii}. In most solar applications, the ions spiral many times between collisions, so that $\Omega_i\tau_{ii} \gg 1$ and Spitzer gives $k_{\parallel}/k_{\perp} = 2 \times 10^{-31}\frac{n^2}{T^3B^2}$, with B in Tesla. However, in the lower chromosphere and photosphere, Hydrogen is largely neutral. In these partially ionized regions, neutral Hydrogen atoms make an important contribution to the conducted heat flux and electron heat conduction can be essentially negligible. In these regions, energy transport by radiative transfer becomes important. By contrast, in coronal active regions, the plasma is fully ionized. The magnetic field is strong enough to give $k_{\parallel}/k_{\perp} \gg 1$, therefore the conduction is mainly along the magnetic field line and the heat conduction term can be approximated by $\nabla_{\parallel} \cdot (k_{\parallel}\nabla_{\parallel}T)$.

2.5 Radiative loses

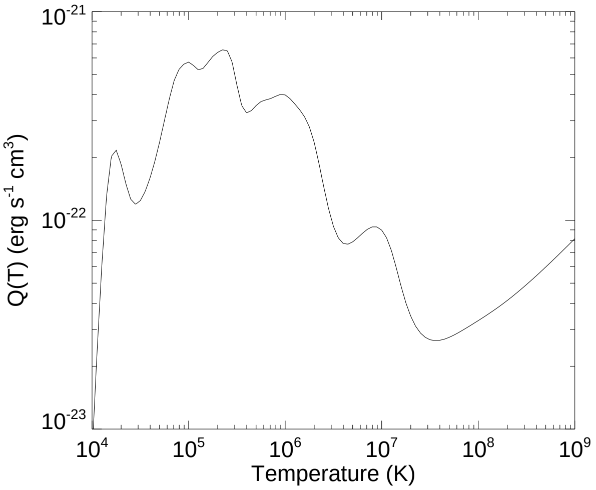

Figure 2.3: Optically thin radiative losses as a function of the temperature for coronal abundances, computed using CHIANTI code (Version 7) (Landi et al. 2012), assuming a density of 10^9 cm^{-3} and ionization equilibrium according to Dere (2009).

For the optically thin part of the atmosphere ($T > 2 \times 10^4$K above the photosphere), the radiative losses can be written as

$$L_r = n_e n_H Q(T) \tag{2.24}$$

where n_e and n_H are, respectively, the electron and the hydrogen ion density (with $n_e = n_H$ in the fully ionized approximation for the hydrogen), and $Q(t)$ depends on the atomic abundances and it includes all the radiative processes at a given temperature.

2.6 Shocks

When a body propagates in a medium with a speed greater than the wave speed it generates a particular class of waves, called shock fronts. This kind of wave rises because the crest of the wave moves faster than its leading or trailing edge and the front of the wave becomes steeper and steeper as the crest catches up until it creates a discontinuity between the trail of the wave and the unperturbed medium ahead of it (Fig. 2.4).

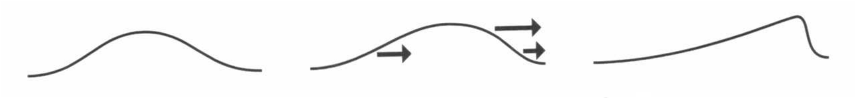

Figure 2.4: Formation of a shock wave by the steepening of a wave profile (Priest 2014).

The shock front is this discontinuity, so it is a very thin transition layer between the perturbed and the unperturbed medium.

One way to model a shock front is to consider it as the layer that separates an unperturbed medium (ahead of the shock), denoted by subscripts (1) and a perturbed one (behind, 2). The speed of the shock and shocked medium are in a frame at rest, respectively, U, U_2 ($< U$, Fig. 2.5 (left)). A more convenient

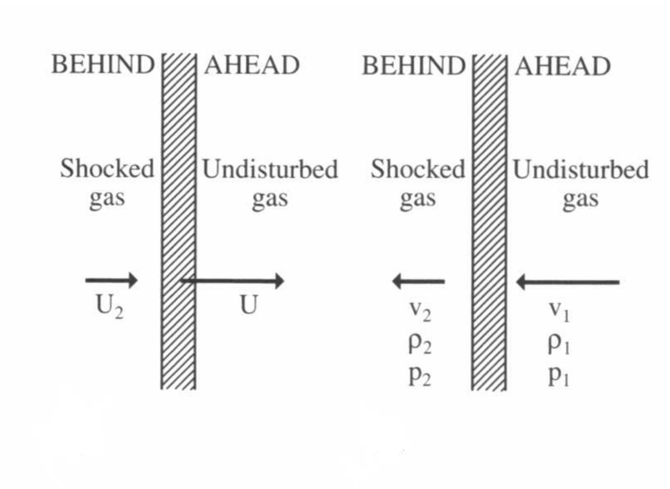

Figure 2.5: A rightward propagating shock viewed from the fluid at rest (left) and from a reference system moving with the shock (right). The subscripts 1 and 2 denote the variables, respectively, in the unperturbed and perturbed medium (Priest 2014).

way to describe it is to consider the frame of reference that moves with the shock front (Fig. 2.5 (right)). In this frame, the unperturbed medium has a speed

$$v_1 = U, \tag{2.25}$$

and the perturbed one

$$v_2 = U - U_2. \tag{2.26}$$

Since U_2 is positive, one can derive that

$$v_2 \leq v_1. \tag{2.27}$$

We now present a set of jump conditions that relate the properties on both sides of the shock front without describing the shock front itself. These conditions can be obtained by applying the conservation of mass, momentum and energy at the shock front interface.

First of all, we present the conditions in the hydrodynamics case, then, in the general magneto-hydrodynamics case. At the end, we present the general properties of the particular case in which the velocity of the shock is perpendicular to the magnetic field.

2.6.1 Hydrodynamics shocks

Consider a steady plane shock propagating into an ideal and stationary gas. In the frame of reference moving with the shock front, the unperturbed plasma is characterized by a density ρ_1, a pressure p_1 and a velocity v_1, while the shocked plasma has a density ρ_2, a pressure p_2 and a velocity v_2.

We can determine the variables of the shocked plasma (ρ_2, p_2, v_2) applying the conservation laws at the shock front and we obtain

$$\rho_2 v_2 = \rho_1 v_1 \tag{2.28}$$

$$p_2 + \rho_2 v_2^2 = p_1 + \rho_1 v_1^2 \tag{2.29}$$

$$p_2 v_2 + (\rho_2 e_2 + \frac{1}{2}\rho_2 v_2^2) v_2 = p_1 v_1 + (\rho_1 e_1 + \frac{1}{2}\rho_1 v_1^2) v_1 \tag{2.30}$$

where e is the internal energy per unit of mass that in our case (i.e. perfect gas) is $e = \frac{p}{(\gamma-1)\rho}$. By substituting it in eq. 2.30 and using eq. 2.28 we obtain the more compact form

$$\frac{\gamma p_2}{(\gamma-1)\rho_2} + \frac{1}{2}v_2^2 = \frac{\gamma p_1}{(\gamma-1)\rho_1} + \frac{1}{2}v_1^2 \tag{2.31}$$

These are called *Rankine-Hugoniot* relations. By playing with substitutions one can derive the ratio between variables across the shock front

$$\frac{\rho_2}{\rho_1} = \frac{(\gamma+1)M_1^2}{2+(\gamma-1)M_1^2} \tag{2.32}$$

$$\frac{v_2}{v_1} = \frac{2+(\gamma-1)M_1^2}{(\gamma+1)M_1^2} \tag{2.33}$$

$$\frac{p_2}{p_1} = \frac{2\gamma M_1^2-(\gamma-1)}{(\gamma+1)} \tag{2.34}$$

where $M_1 = \frac{v_1}{c_{s1}}$ is the so-called *Mach number*, with $c_{s1} = \sqrt{\gamma \frac{p_1}{\rho_1}}$ is the sound speed.

We can derive some important properties of shocks from these expressions. If we insert the condition $v_2 \leq v_1$ in eq. 2.33 we obtain that $v_1 \geq c_{s1}$ (or $M_1 \geq 1$), so the speed of the shock must exceed the sound speed, and $v_2 \leq c_{s2}$. This means that the gas is subsonic behind the shock and it is supersonic ahead of it, so the information can not be transmitted ahead of the shock but can catch it up from behind.

Since $v_2 \leq v_1$, the ratio $\frac{\rho_2}{\rho_1}$ is > 1 as well as for $\frac{p_2}{p_1}$. This means that the shocked plasma is being compressed by the shock.

We also can derive a condition between the temperature ahead and behind the shock, substituting the perfect gas law in the energy equation. We obtain that $T_2 \geq T_1$. This condition tells us that shock slows down the plasma and heats it up, so it converts kinetic energy to thermal energy.

Finally, we can consider the limits of these relations in terms of the Mach number. If we consider the case in which $M_1 = 1$, we have no shock and we obtain $p_2 = p_1$,$\rho_2 = \rho_1$,$v_2 = v_1$, so we start to have shock only if $M_1 > 1$, greater the Mach number greater the compression and the heating. While the ratio in pressure can grow without limit, the ratio in density is limited to the range

$$1 \leq \frac{\rho_2}{\rho_1} < \frac{\gamma+1}{\gamma-1} \tag{2.35}$$

from which we derive the theoretical limit of 4, with $\gamma = \frac{5}{3}$ (i.e. mono-atomic gas). As a consequence, the temperature in the post shock region can grow without limit.

2.6.2 MHD shocks

Now we present the *Rankine-Hugoniot* conditions in the general case in which the magnetic field and the velocity of the plasma are both inclined respect the shock front (i.e. *oblique shocks*, Priest 2014). The conditions are written in terms of the compression ratio (ρ_2/ρ_1), the sound speed ($c_{s1} = \sqrt{\gamma p_1/\rho_1}$) and the Alfvén speed ($v_{A1} = \sqrt{B_1^2/(4\pi\rho)}$)

$$\frac{v_{2x}}{v_{1x}} = X^{-1} \tag{2.36}$$

$$\frac{v_{2y}}{v_{1y}} = \frac{v_1^2 - v_{A1}^2}{v_1^2 - Xv_{A1}^2} \tag{2.37}$$

$$\frac{B_{2x}}{B_{1x}} = 1 \tag{2.38}$$

$$\frac{B_{2y}}{B_{1y}} = \frac{(v_1^2 - v_{A1}^2)X}{v_1^2 - Xv_{A1}^2} \tag{2.39}$$

$$\frac{p_2}{p_1} = X + \frac{(\gamma - 1)Xv_1^2}{2c_{s1}^2}(1 - \frac{v_2^2}{v_1^2}) \tag{2.40}$$

where X is the solution of

$$\begin{aligned}&(v_1^2 - Xv_{A1}^2)^2 Xc_{s1} + \frac{1}{2}v_1^2 cos^2\theta[X(\gamma-1) - (\gamma+1)] + \\ &\frac{1}{2}v_{A1}^2 v_1^2 sin^2\theta Xx[\gamma + X(2-\gamma)]v_1^2 - Xv_{A1}^2[(\gamma+1) - X(\gamma-1)] = 0.\end{aligned} \tag{2.41}$$

θ is the inclination of the upstream magnetic field to the shock normal.

The three solutions of this equation give three different class of waves: slow-mode, intermediate waves and fast-mode shocks. These solutions are differentiated in the velocity and the compression ratio X. While the slow- and fast-mode shocks are compressive, the intermediate waves are not. In the former cases, the velocity of the shock is, respectively, $v_1 \leq v_A (< Xv_A)$ and $v_1 \geq Xv_A (> v_A)$, while in the latter case is $v_1 = v_A$.

We now present, as an example, the simplified case in which $\theta = 0$, called *perpendicular shock* (i.e. the shock propagates perpendicularly to the magnetic field).

2.6.3 Perpendicular shocks

In this case the eq. 2.41 becomes

$$f(X) = 2(2-\gamma)X^2 + (2\beta_1 + (\gamma-1)\beta_1 M_1^2 + 2)\gamma X - \gamma(\gamma+1)\beta_1 M_1^2 = 0. \tag{2.42}$$

where β_1 is the ratio between thermal and magnetic pressure in the unperturbed medium. Considering that f(X) is a quadratic function of X, the conditions of compressive shock leads to the condition $f(1) \leq 0$ or $v_1^2 \geq c_{s1}^2 + v_{A1}^2$. The latter condition states that the shock speed must exceed the magneto-acoustic speed ahead of the shock (i.e. $\sqrt{c_{s1}^2 + v_{A1}^2}$), therefore, in the MHD case, the magneto-acoustic speed plays the same role of the sound speed (c_{s1}) in the HD case. The compression factor X has the same limit as in the HD case, and the magnetic field suffers the same condition

$$1 < \frac{B_2}{B_1} < \frac{\gamma+1}{\gamma-1} \tag{2.43}$$

thus, the value of the magnetic compression is limited, for a mono-atomic gas, between 1 and 4.

Chapter 3

Downflows

3.1 The observation

In this Chapter, we study the interaction of downfalling fragments of plasma, spread onto the solar surface by a solar eruption after an M-class flare in 7 June 2011. The event was observed by the Atmospheric Imaging Assembly (AIA) (Lemen et al. 2012) on board the Solar Dynamics Observatory (SDO) (Pesnell et al. 2012), in the ultraviolet (UV) and extreme-ultraviolet (EUV) narrow-band channels. The AIA instrument provides data with a high cadence of ($\sim$ 12 s) and high spatial resolution of ($\sim$ 0.6 arsec per pix). In this event, a dense and cold filament is broken into many fragments erupting in all directions. Part of them fall back onto the solar surface, far from the eruption location.

Some fragments fall outside of active regions, where the magnetic field is weak, so they show ballistic trajectories until they hit the solar surface. In the proximity of the impact region, a brightening is observed (Reale et al. 2013). Other fragments instead fall close or inside active regions, and here we focus on one of these active regions (the one whose center is [580,280] arcsec from the disk center). Fig. 3.1a shows the entire trajectory of one of these fragments (tracked with an automatic detector of local emission minima; Reale et al. 2013). The fragment follows a ballistic motion as long as it is far from the active region, but close to it, it is deviated, as is clear from the final part of the path shown in Fig. 3.2a. Fig. 3.1b shows images at three subsequent times of the fragment final evolution in the AIA 171 Å channel. A brightening is observed already as it is being channelled by the magnetic field, before impacting the solar surface. This bright front precedes this fragment (and others) and propagates ahead of it along the entire magnetic flux tube. The fragment disappears once it is completely channelled. During the fall, before they are channelled, the fragments are dark in all of the AIA EUV channels. They change shape but remain small, compact blobs.

Since the blobs fall ballistically until the interaction with the magnetic field causes a change in the trajectory, their velocity component perpendicular to the solar surface can be estimated by the simple formula,

$$v_{ff} = \sqrt{2 g_\odot D} \sim 240\ km/s \tag{3.1}$$

where $g_\odot \sim 2.74 \times 10^4$ cm s^{-2} is solar gravity and $D \sim 10^{10}$ cm is the maximum height reached by the blobs above the surface. This height has been estimated as the distance of the apex from the line connecting the footpoints. Therefore, we are assuming that, since the event is close to the solar limb, we are seeing the trajectory in Fig. 3.1a face-on and with no other

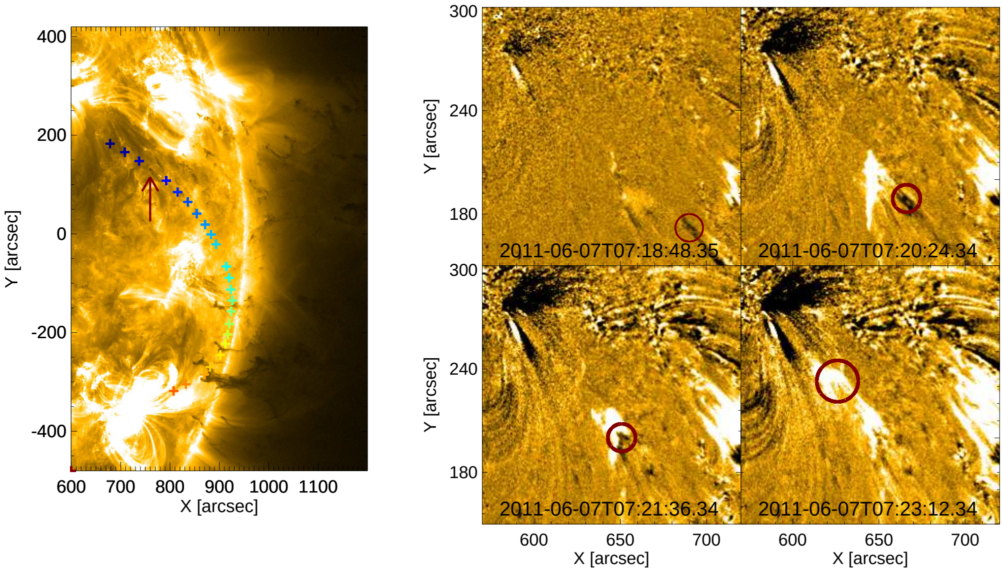

(a) (b)

Figure 3.1: (a) Time increases from red to blue (crosses are spaced by ~ 120 s): path followed by a fragment of the erupted plasma from the flaring active region to the impact active region. Time progresses from red crosses (6:30 UT) to blue crosses (7:19 UT). The background image is taken in the AIA 171 Å channel at time 7:13 UT (the position of the fragment at this time is indicated by the arrow). (b) Images (subtracted from the one at 7:18 UT) of the final evolution of the fragment in (a), marked by red circles, impacting the solar surface in the proximity of the active region at subsequent times.

tilting. Moderate differences from this assumption do not lead to substantial variations of v_{ff} (for a tilted trajectory of $\sim 30^o$ the error is $\sim 10\%$). To estimate the velocity component parallel to the solar surface, we make the rough assumption that, in the very final part of the trajectory (Fig. 3.1b), we detect mostly the motion projected on the solar surface. We measure a projected length of $\sim 4 \times 10^9$cm that is covered in a time of ~ 200 s, which corresponds to a horizontal speed of $v_h \sim 200$km/s. The total velocity of the blobs is then estimated to be $v_{tot} = \sqrt{v_{ff}^2 + v_h^2} \sim 300$km/s.

Along the final part of the trajectory, we have also defined a strip and divided it into approximately square sectors. In each sector, we have evaluated the average emission and subtracted the value at an early time (7:10 UT). Fig. 3.2b shows the resulting emission profiles along the path as a function of time (600 s, from 7:14 UT to 7:24 UT). The blob is dark at early times, when it is still far from the active region. After $t \sim 200$ s, it begins to fade away and for $t > 400$ s it turns into a bright feature. The bright features at position $\sim 5 \times 10^4$km ($t > 300$s) and 1.4×10^5km ($t \sim 200$ s) are not moving ones. Fig. 3.2c show profiles of the emission zoomed close to the active region and in the final stage of the evolution. The fronts move from right to left and become increasingly bright, with an emission rate in the range $50 - 150$ DN/s/pix.

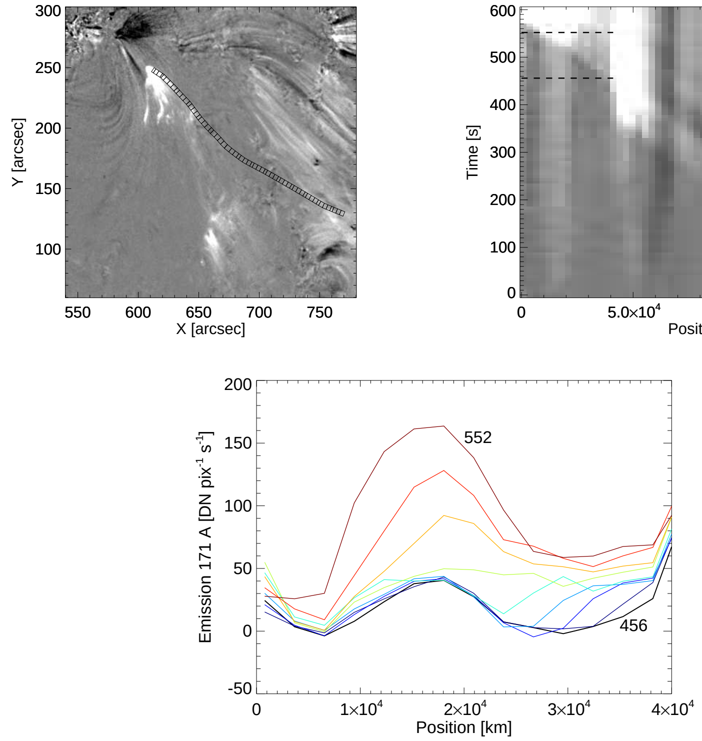

Figure 3.2: 171 Å difference image at 7:24 UT, after subtracting the first in the sequence (7:10 UT), in which we track the position of the falling blob. A clear change in the trajectory can be seen at $\sim (680, 180)$ arcsec, approaching the active region. (b) 171 Å emission along the strip in panel (a) as a function of time, between 7:14 UT and 7:24 UT. The gray scale is in the range of [-100,100] DN pix^{-1} s^{-1}. The dashed line bounds the time and space range of panel (c). (c) 171 Å emission along the strip in panel (a) zoomed in on the space and time range between the dashed lines in panel (b). The lines are spaced by 12 s, with the time increasing from blue to red. The initial and final curves are at the labelled times (s).

Before brightening, the blobs are dark. From the amount of absorption, one can estimate their density as described in Landi & Reale (2013). We obtain a density ranging between 1 and 4×10^{10} cm^{-3}. For our simulation, we assume 2×10^{10} cm^{-3} as the blob density of our reference case, but in other cases we consider a blob density of 10^{10} cm^{-3} (see section 3.2).

3.2 MHD Modelling

We study the evolution of the downfalling fragments in the magnetic field with detailed modelling of template blobs. In particular, we describe the evolution of four downfalling blobs across a magnetized and relatively dense corona. Our model solves numerically the magneto-hydrodynamic equations presented in Chapter 2 which are the conservation of mass, momentum, energy, and the induction equation. The model considers the important physical effects of gravity, thermal conduction, radiative losses and the heating of the solar corona. We assume energetic equilibrium in the chromosphere and inside the initial cold blobs, therefore they are not heated and do not emit. We use the astrophysical code PLUTO to run the simulations (see Appendix A).

3.2.1 Initial and boundary conditions

The ambient magnetic field is not aligned to the initial direction of blob's downfall, however, we assume a symmetric magnetic field with respect to a plane perpendicular to the surface and crossing the middle of the domain and of the blobs. The blobs will not acquire average motion components in the horizontal direction across the magnetic field although later effects due to the magnetic field are expected during the dynamics. Therefore, we need a full 3D description, but we do not need a large domain extension in that direction, which we assume to be the Y direction.

To approach the configuration of a loop-populated active region, but still keeping it manageable and simple, we consider a combination of three magnetic dipoles, so that the magnetic field is symmetric with respect to the side boundaries and is closed in the low region close to the chromosphere. The analytical expression (Bx,By,Bz) of the magnetic field is given by

$$
\begin{aligned}
Bx &= 3d(\frac{x(z-z_d)}{R^5} - \frac{(x-x_d)(z-z_d)}{R_1^5} - \frac{(x+x_d)(z-z_d)}{R_2^5}) \\
By &= 3d(\frac{y(z-z_d)}{R^5} - \frac{y(z-z_d)}{R_1^5} - \frac{y(z-z_d)}{R_2^5}) \\
Bz &= \frac{d}{R^3}(\frac{3(z-z_d)^2}{R^2} - 1) - \frac{d}{R_1^3}(\frac{3(z-z_d)^2}{R_1^2} - 1) - \frac{d}{R_2^3}(\frac{3(z-z_d)^2}{R_2^2} - 1)
\end{aligned}
$$

where d is the intensity of the magnetic dipole, which is equal between dipoles but it is varying between the models we explored (see below), x_d is equal to 8×10^9 cm, z_d is equal to -2.5×10^9 cm, R, R_1, R_2 are distances from the center of the dipoles, located at $(0,0,z_d)$, $(x_d,0,z_d)$ and $(-x_d,0,z_d)$.

The computational box is three-dimensional and cartesian (X, Y, Z) and extends over 4×10^9 cm in the X direction, 1.2×10^9 cm in the Y direction and 6×10^9 cm in the Z direction. The Z direction is perpendicular to the solar surface. The mesh of the 3D domain is uniformly spaced along the three directions with $512 \times 128 \times 512$ cells, giving a cell size of $\sim 80 \times 90 \times 120$km. This provides a good compromise to have both good resolution in all directions (the domain is larger along Z) and reasonable computational times. The blobs are sufficiently well resolved (their diameter ranges of 30-40 cells) and the resolution allows for a steady initial atmosphere.

In this box, we consider an ambient relatively dense corona linked to a much denser chromosphere through a steep transition region. The corona is a hydrostatic atmosphere (Rosner et al. 1978) that extends for 10^{10} cm. The chromosphere is hydrostatic and isothermal at 10^4 K with a density at the base of $\sim 10^{16}$ cm^{-3}. The atmosphere is made plane-parallel along the vertical direction (Z).

Our simulation strategy is to freeze the parameters of the falling blobs (except for their density in one case), which are constrained from the observation, and to consider a few different conditions of the background atmosphere and magnetic field. In general, the topology of the magnetic field, combined with the atmosphere conditions, ensures that the blobs propagate in a medium in which the β parameter of the plasma is highly varying, i.e. increasing while approaching the chromosphere.

We take as 'reference model' (here after RM) the configuration in which the pressure of the background atmosphere ranges between 0.05 dyn cm^{-2} at the top of the transition region and 0.014 dyn cm^{-2} at $Z = 6 \times 10^9$ cm. In this case, the ion density is $n_0 \sim 5 \times 10^7$ cm^{-3} and the temperature is $T_0 \sim 1 \times 10^6$ K at $Z = 6 \times 10^9$ cm. The magnetic field intensity is $\sim$ 170G at the top of the transition region and $\sim$ 15 G at the initial position of the blobs (see below), which values lead to a plasma β $(\rho v^2/(B^2/8\pi)) \sim 4$ and an Alfvén Mach number $(v_{flow}/v_{Alfven}) \sim 0.03$.

We explore three other configurations that differ from the RM, either for the background atmosphere or for the magnetic field intensity. The second and third case, which are the 'dense model' (hereafter DM) and the 'cool model' (hereafter CM), differ from the RM for the hydrostatic conditions. The pressure ranges between 0.29 and 0.14 dyn cm^{-2} (DM) and between 0.01 and 0.0009 dyn cm^{-2} (CM), respectively. The ion density and the temperature are, respectively, $\sim 3 \times 10^8$cm^{-3} and $\sim 1.9 \times 10^6$K (DM) and $\sim 6 \times 10^6$cm^{-3} and $\sim 5 \times 10^5$K (CM), at $Z = 6 \times 10^9$cm. The plasma β is ~ 2 and the Alfvén Mach numbers are, respectively, ~ 0.06 and ~ 0.01. The fourth case is a 'weak field model' (hereafter WM) which differs from the DM for the magnetic field intensity, which is about an order of magnitude lower, i.e., 1 G at the initial position of the blobs and 10 G at the top of the transition region. In this case, the plasma β and the Alfvén Mach number are, respectively, ~ 500 and ~ 0.13. In all the models the position of the transition region varies between $Z = 0.6 \times 10^9$cm and $Z = 1 \times 10^9$cm. In Fig. 3.3 we present the profiles of density and temperature of the ambient medium along the Z direction.

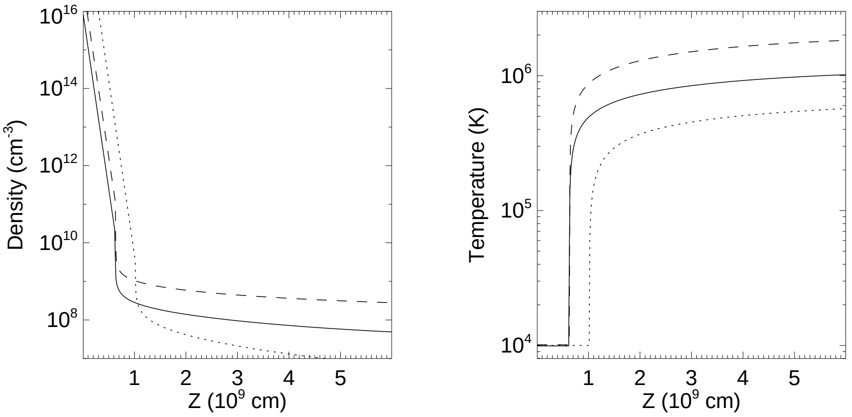

Figure 3.3: Density (left) and temperature (right) profiles of the reference (RM, solid line), cool (CM, dotted), and dense (DM, dashed) model atmospheres in the vertical direction (Z).

In all cases, four blobs are initially put at a height in the range between $\Delta Z = 3.5 \times 10^9$ cm and $\Delta Z = 4.5 \times 10^9$ cm above the chromosphere, and at a distance in a range between $\Delta X = 2.5 \times 10^9$ cm and $\Delta X = 4 \times 10^9$ cm from the left boundary side, close to the upper right corner. These length scales are in agreement with the path length that we measured in the observation (see section 3.1). For the sake of simplicity, we considered spherical blobs. Their radii are different, around the value we estimated from the data ($1.4 - 2 \times 10^8$ cm). The blobs have an initial downward vertical speed of $v = 300$km/s and a temperature of $T = 10^4$K. The initial temperature of the blobs is not very important because their evolution is much faster than any pressure readjustment with the ambient medium and we assume that they initially do not emit radiation. The blobs have a density of 2×10^{10}cm^{-3} in the RM, and 10^{10}cm^{-3} in the other cases. The different density is not critical, but the choice provides the best match with the data for the reference case (RM, see Section 3.3.5).

Boundary conditions are reflective at the left end of the X axis, the magnetic field is forced to be perpendicular to the boundary at the right end of the X axis, but, for the other variables, zero gradient has been set. Fixed conditions have been set at the lower end of the Z axis, and zero gradient at the upper end, with the exception of the magnetic field that is fixed. The same conditions are set at the far end of the Y axis. The computational domain is symmetric to a plane in $Y = 0$, so we simulate half domain and set reflective conditions at the lower end of the Y axis.

3.3 The simulations

The RM is our best model. We now describe the evolution for the RM and then we discuss separately how the other cases differ from this one.

3.3.1 The Reference Model (RM)

We present relevant snapshots of the density and temperature in a cross-section $X - Z$ at the center of the domain, at the beginning and at eight later times in Fig. 3.4 and Fig. 3.5. The blobs start to fall vertically by the gravity (see $t = 49$ s), because their ram pressure ($p_r = \rho v^2$) largely exceeds the surrounding magnetic pressure ($p_m = B^2/8\pi$) and the buoyancy is small:

$$p_r \sim 40 \;\; dyn\ cm^{-2} >> p_m \sim 10 \;\; dyn\ cm^{-2} \tag{3.2}$$

During this vertical motion, which lasts for ~ 60 s, the blobs compress the magnetic field lines below them (as evident in the figure [1]), and the magnetic

---

[1] Some field lines are apparently not frozen to the plasma. This is an artifact of the 2D mapping of the field line reconstruction. The actual lines do not differ so much than the ones displayed.

pressure increases there. During this process, the magnetic field progressively brakes the blobs in the direction perpendicular to the field lines, until the magnetic pressure fully balances the ram pressure, and the blobs move only along the field lines.

In this phase, the blobs are being compressed too, due to the braking by the magnetic field and to the interaction with a relatively dense ambient plasma, becoming slabs at higher density (5×10^{10} cm^{-3}), but temperature still close to the initial value (10^4K). Behind these compressed blobs, wakes develop, with coronal density, but with a temperature that is not as high ($T \sim 6 \times 10^5$K).

After the initial compression, the magnetic field overexpands back to eventually reach an equilibrium close to the initial condition. The blobs are then stretched out perpendicular to the magnetic field lines by the expansion of the field. The final result is that the blobs spread out into a highly fragmented flow (Figs. 3.4-3.6).

This effect can be explained as follows: each blob falls, compressing the field lines ahead of it. At the same time, it drags the field lines that cross it. This field line shifting is not uniform, because of the shape of the blob and of the presence of other nearby blobs, and creates a differential stress back on the blobs. This stress becomes complex with the back-expansion of the field. Thus, the expansion of the field acts as a mixer that fragments the flow. The possible development of MHD Rayleigh-Taylor instabilities has also been taken into account. However, the intense magnetic field suppresses them (see Appendix B).

The field line shifting also perturbs the footpoint of the magnetic channel, leading to a rapid change of its section close to the chromosphere. These changes produce pressure gradients that trigger spicule-like upflows, not investigated in this paper.

After $t \sim 100$ s the expansion of the field ends and the initial magnetic field configuration is fully restored. The fragments continue to flow along the field lines with only a fraction of the initial velocity (~ 100 km/s). The cool and dense plasma appearing after the blobs are channelled (Figs. 3.4-3.5) is not caused by thermal instability, as in Fang et al. (2015); Xia et al. (2014), and Xia & Keppens (2016). Instead, this is part of the fragments that, while falling and distorting, occasionally cross the 2D plane of the figure.

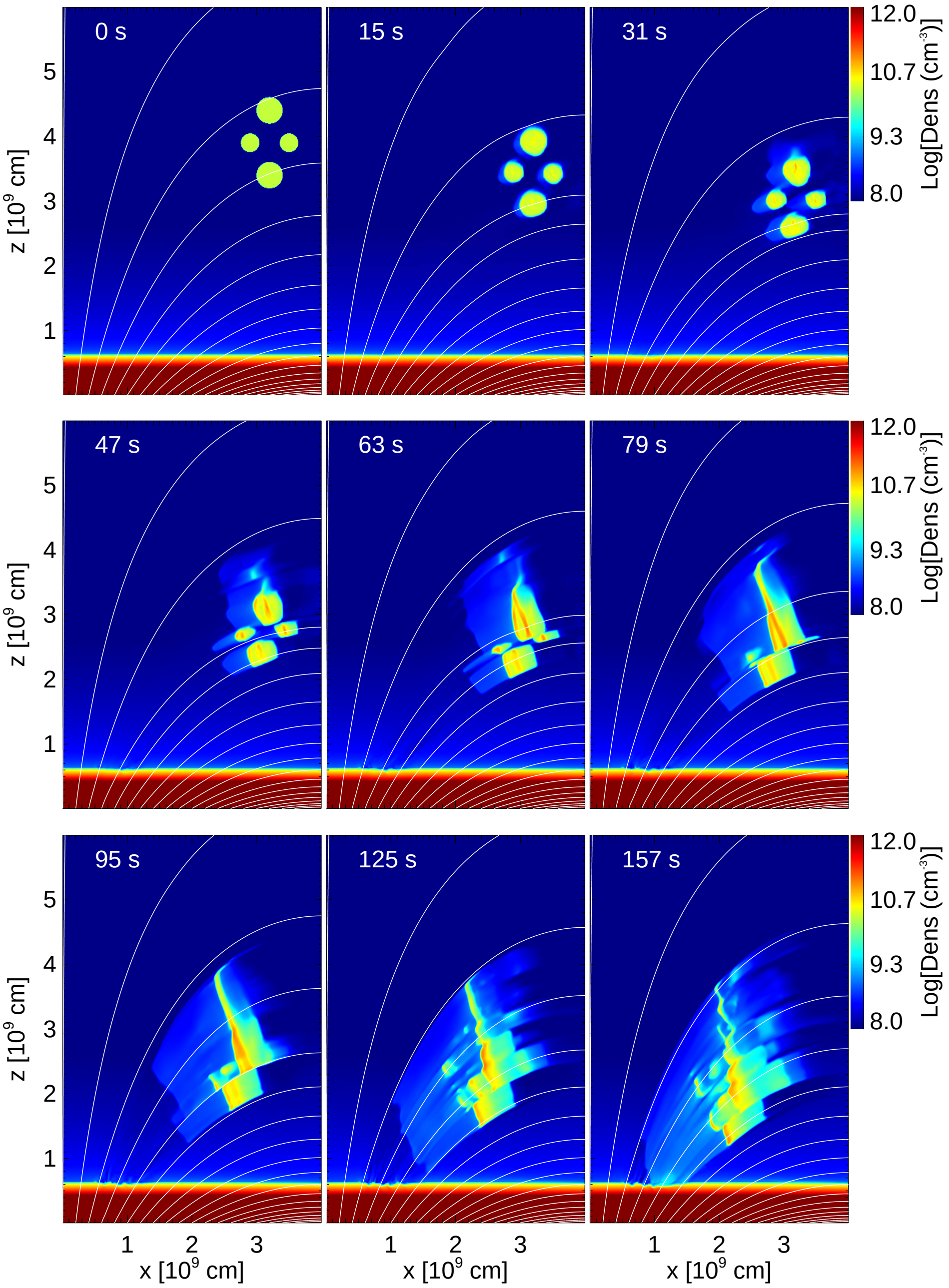

Figure 3.4: Reference simulation (RM): density in the central cross-section $X - Z$ of the domain, at nine different times, in logarithmic scale. In all panels, magnetic field lines are shown. The color scales are saturated in the range of the palette.

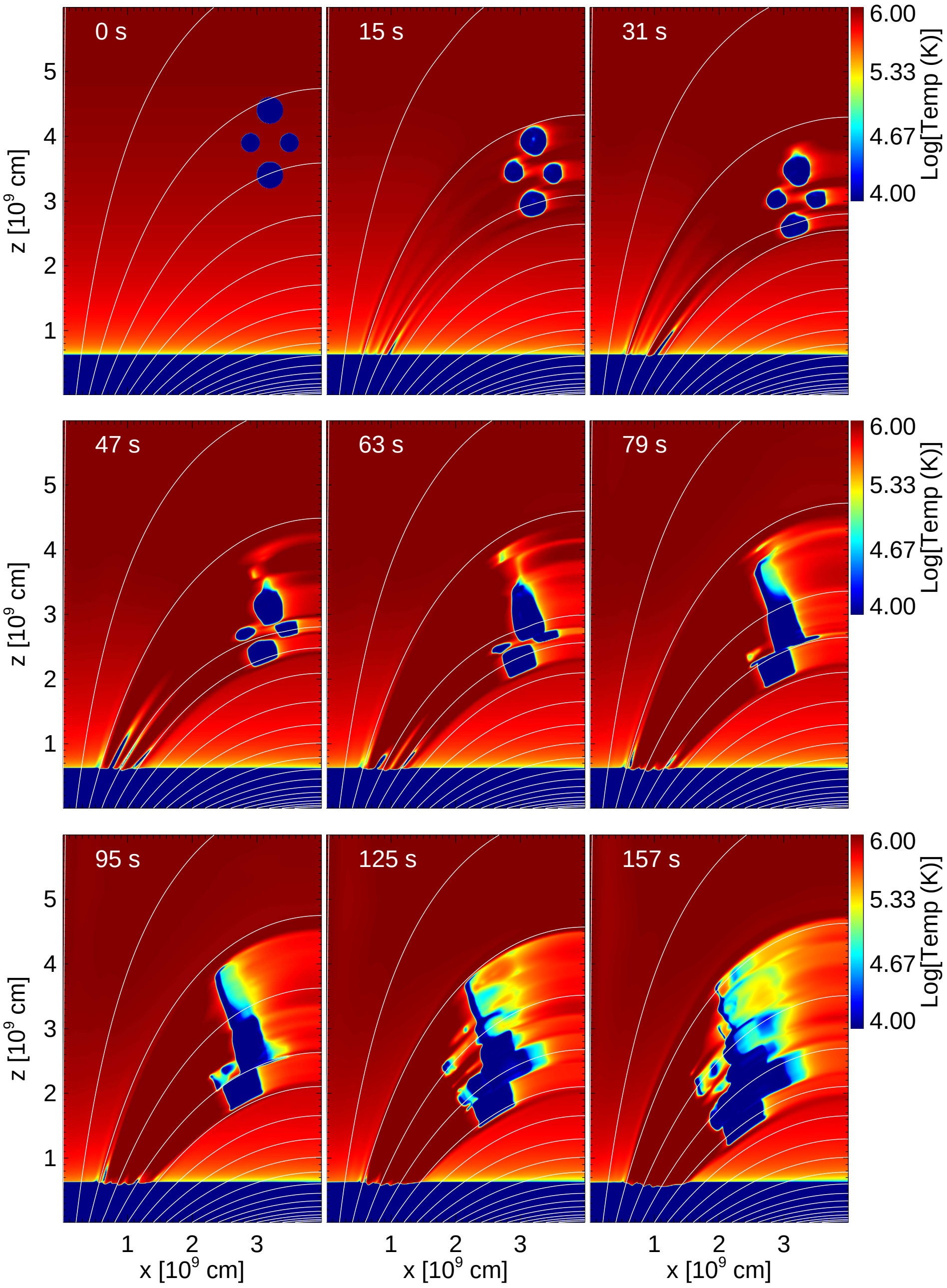

Figure 3.5: Reference simulation (RM): temperature in the central cross-section $X-Z$ of the domain, at nine different times, in logarithmic scale. In all panels, magnetic field lines are shown. The color scales are saturated in the range of the palette.

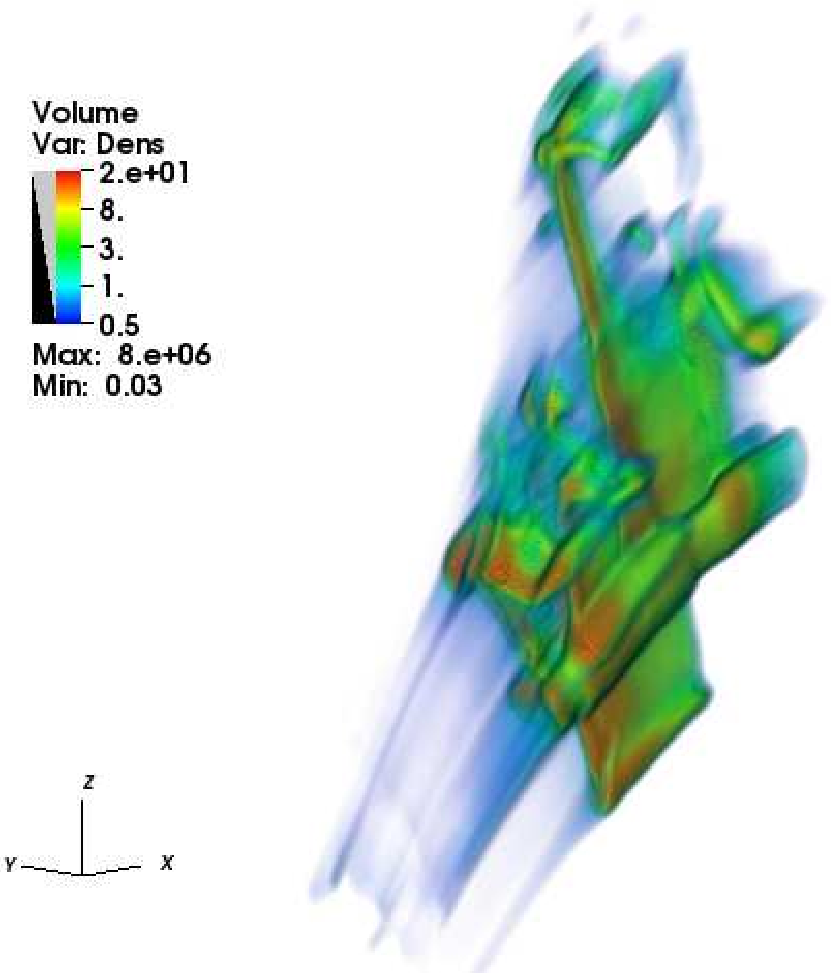

Figure 3.6: Rendering of the density (in units of 10^9 cm^{-3}) of the blobs at 100s. The blobs are denser (green-red) than the shocked plasma (blue).

The initial velocity of the blobs along the field lines is $\sim$ 100 km/s, due to a relative inclination of $\sim 70^o$. This velocity is comparable to the sound speed in the corona (c_s):

$$c_s = \sqrt{\frac{p}{\rho}} = \sqrt{\frac{2k_BT}{\mu m_H}} \sim 100\ km/s \tag{3.3}$$

where we assume isothermal shocks. Therefore, shocks propagate ahead of the blobs. These shocks compress and heat the coronal material between the blobs and the chromosphere to temperatures of $T \sim 1 - 2 \times 10^6$K. An estimate of the shock speed (v_{sh}) can be evaluated considering that they move along a path of $\delta l \sim 4.3 \times 10^4$ km until they hit the chromosphere for a time $\delta t \sim 140$ s:

$$v_{sh} = \frac{\delta l}{\delta t} = \frac{4.3 \times 10^4}{140} \sim 300 \quad km/s \tag{3.4}$$

or by the Rankine-Hugoniot formula for isothermal shocks:

$$\frac{\rho_2}{\rho_1} = \frac{v_1^2}{c_s^2}, \quad v_1 \sim 300 \; km/s \tag{3.5}$$

where ρ_2 and ρ_1 are the density of post- and pre-shock medium, respectively (Fig. 3.7), c_s is the sound speed, and v_1 is the velocity of the pre-shock medium in the reference frame of reference the shock (so it is the velocity of the shock in our reference frame). The shocks stream along the field lines, because the Alfvén speed ($v_A = B/\sqrt{4\pi\rho} \sim 1000$ km/s) is much higher than the shock speed v_{sh} (e.g., Priest 2014). These shocks are slow-mode shocks. In the vertically descending phase, the blobs are compressed in the direction perpendicular to the local magnetic field. The compression and the solar gravity together accelerate the leftward expansion of the blobs along the magnetic field lines, which generates and drives these slow-mode shocks.

For a more quantitative grasp of the structure and dynamics of the fragments, Fig. 3.7 shows plots of the density, pressure, and temperature all along a magnetic field line that crosses the lowest blob at the initial position, at three different times. The blob is a squared bump in the density and pressure, and a dip in the temperature at time $t = 0$s. At $t = 50$s, the blob has moved leftward along the line by $\sim 10^4$ km, while being highly spread out and deformed. The shock front is clearly visible ahead of it in the pressure and density, much less in the temperature due to the fact that thermal fronts in corona propagates faster than shocks, so they are almost isothermal (the relative speed of these two phenomena can be triggered by changing the factor ϕ in the saturated thermal conduction, Orlando et al. 2005). At $t = 100$s the front density peak has declined while the central peak has not moved leftward by much. The reason for this apparent rest is that the field line has significantly stretched between 50 and 100 s (by $\sim 20\%$), because of the magnetic field back-expansion. So the distance from the chromosphere at t=100 s should be scaled as well. On the other hand, in spite of this effect, the shock front has moved leftward, by 10^4 km. The temperature has clearly increased to a peak of $\sim$ 2MK.

From the velocity of the shocks one can derive their ram pressure. Considering that the post-shock plasma is at density $n_{sh} \sim 6 \times 10^8 cm^{-3}$:

$$p_{ram\_sh} = n_{sh} \mu m_p v_{sh}^2 \sim 1 \quad dyn\ cm^{-2} \tag{3.6}$$

their ram pressure is much lower than the ambient magnetic pressure ($p_m \sim 10$ dyn cm^{-2} at the blobs initial position).

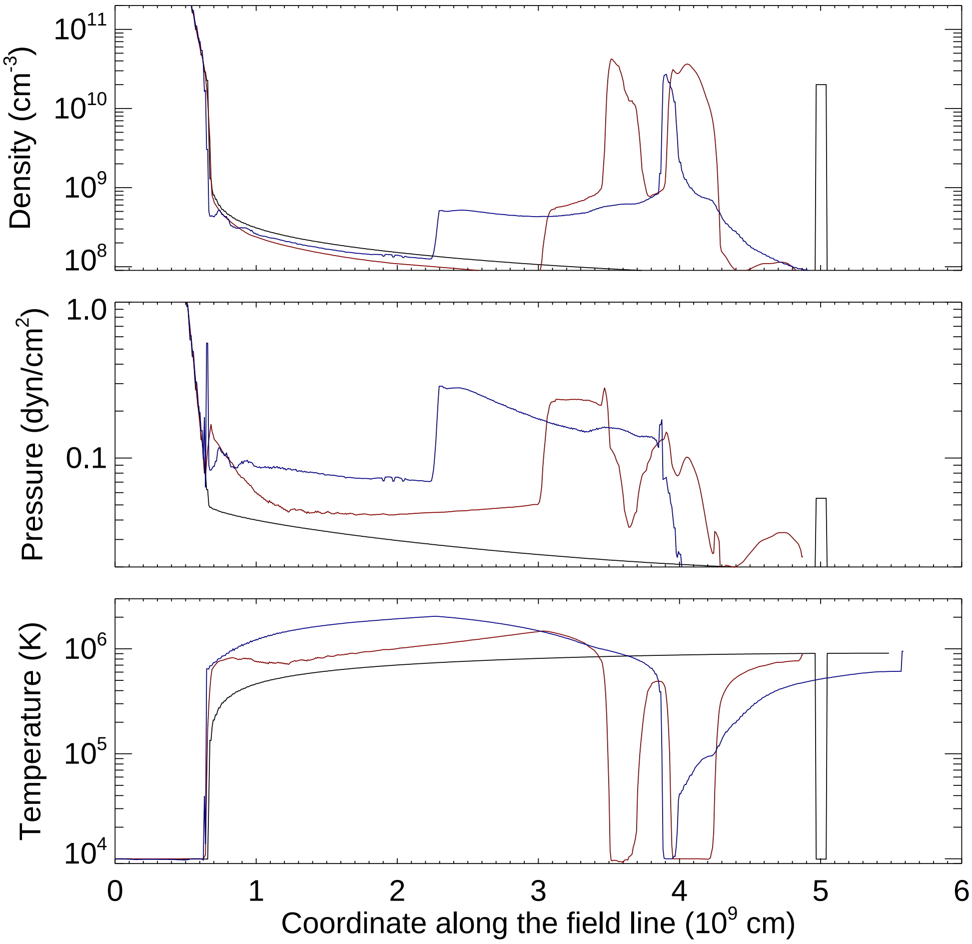

Figure 3.7: Profiles of density, temperature, and thermal pressure along a magnetic field line that encounters one of the blobs at the initial time. The profiles are taken at time t = 0 s (black line), 50 s (red), and 100 s (blue). The chromosphere is at the left-hand side.

3.3.2 Dense model (DM)

In the DM model, the ambient medium is denser and the blobs have half the density as in the previous case. As a consequence of the lower density contrast, the blobs are channelled sooner along the magnetic field lines (Figs. 3.8-3.9), because the magnetic pressure has to balance a lower ram pressure than in the RM. The denser atmosphere affects the shape and the velocity of the blobs. In this case, the velocity is $v \sim 70$ km/s (to be compared with ~ 100 km/s in the RM), and the blobs appear to be thin slabs at higher density ($n \sim 10^{11}$ cm^{-3}) due to the fact that the initial density ratio between blobs and ambient atmosphere is a factor 4 greater than in the previous case. The atmosphere conditions affect also the ratio between post- and pre-shock regions that leads to a velocity of the shocks of 250 km/s. Moreover, the blob motion is much slower and the shocks are much fainter than in the RM.

3.3.3 Cold model (CM)

Overall, in this case, the blobs fragment less than in the previous ones. While they move toward the chromosphere, the blobs are still highly deformed but not squashed into slabs, essentially because the initial density ratio between the blobs and ambient medium is a factor of 20 higher than in DM (Fig. 3.10-3.11). The effect of the dynamics on the magnetic field is the same as in the previous cases, because DM and CM share the same magnetic field configuration and blob density, so Eq. (3.2) still holds. The change in the atmosphere instead affects the residual velocity of the blobs after the magnetic field expansion, which in this case is 120 km/s, and the velocity of the shock, which is 180 km/s.

3.3.4 Weak field model (WM)

In the WM simulation, the magnetic pressure never balances the ram pressure of the blobs, even if it increases because of the falling blobs similarly to the previous cases. Therefore, Eq. (3.2) holds at all times and the blobs fall vertically until they impact the chromosphere, as shown in Fig. 3.12. The shock ahead of the blobs is very weak and rapidly damped by the compressed magnetic field that envelopes the blobs during the falling. This simulation is quite similar to those shown in Reale et al. (2013), but quite different from the observed evolution. Therefore, it puts a lower limit to the ambient magnetic field intensity (~ 1 G), but we will no longer discuss it in the following.

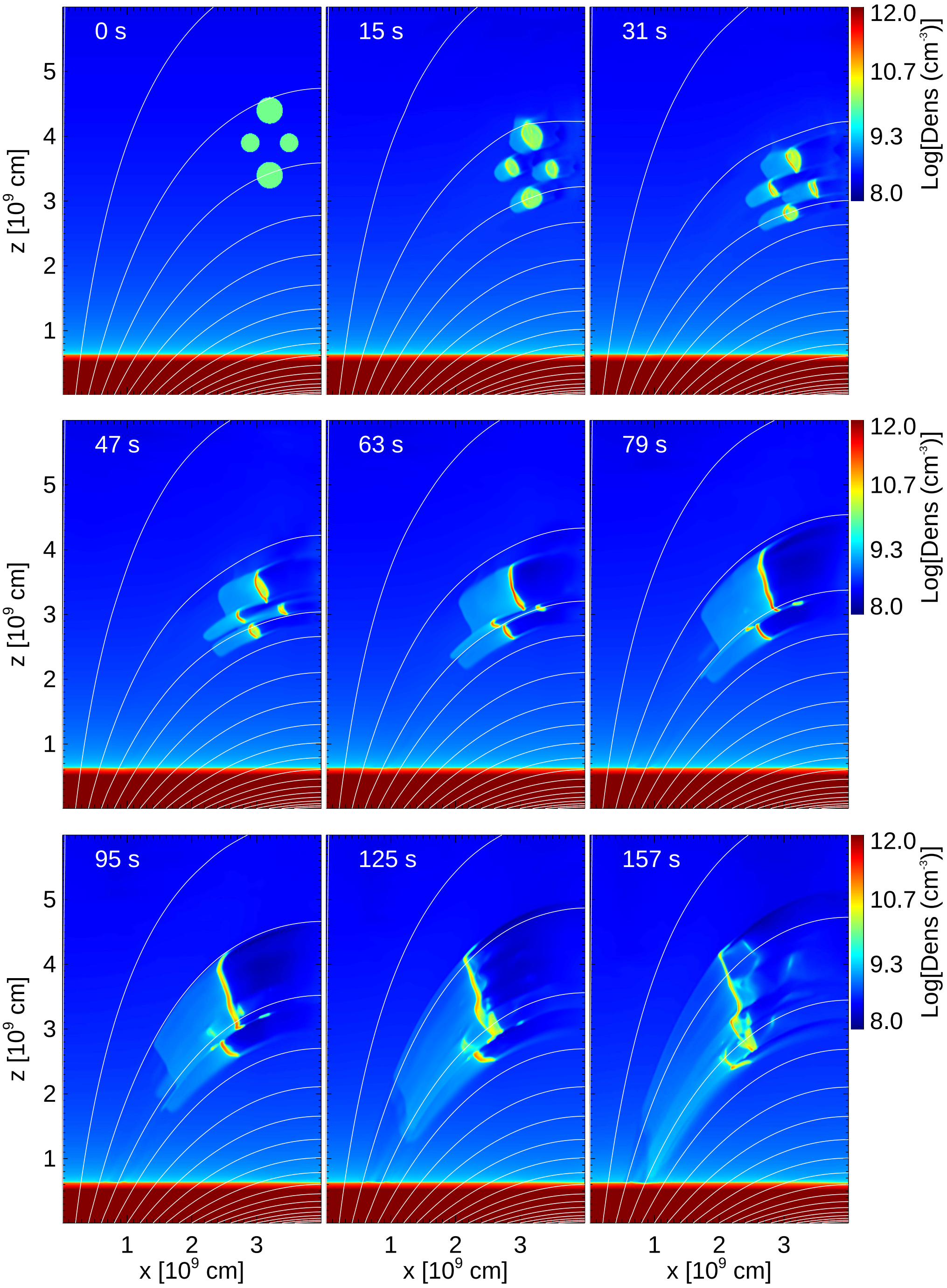

Figure 3.8: Same as in Fig. 3.4 but for the Dense Model (DM).

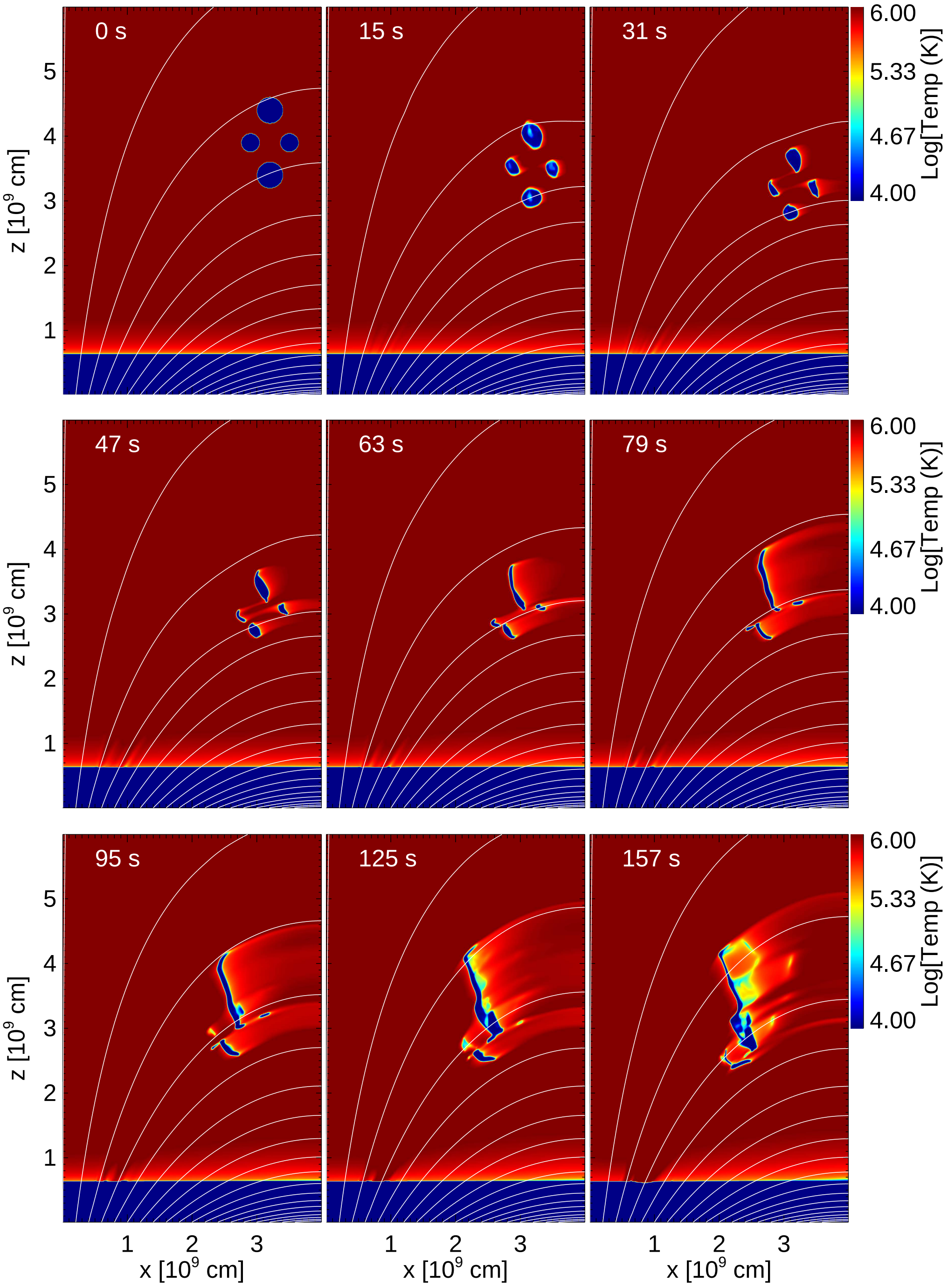

Figure 3.9: Same as in Fig. 3.5 but for the Dense Model (DM).

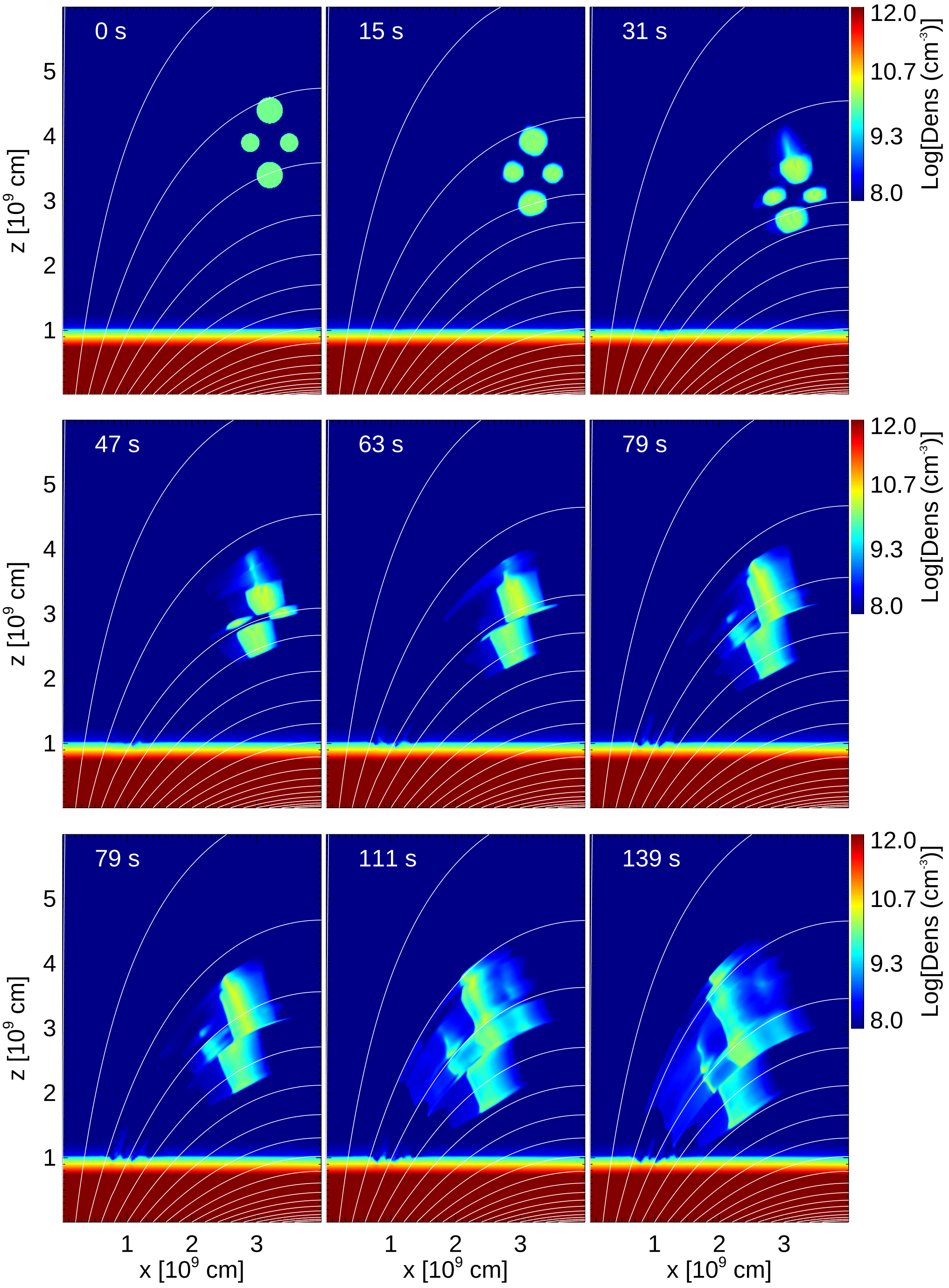

Figure 3.10: Same as in Fig. 3.4 but for the Cold Model (CM).

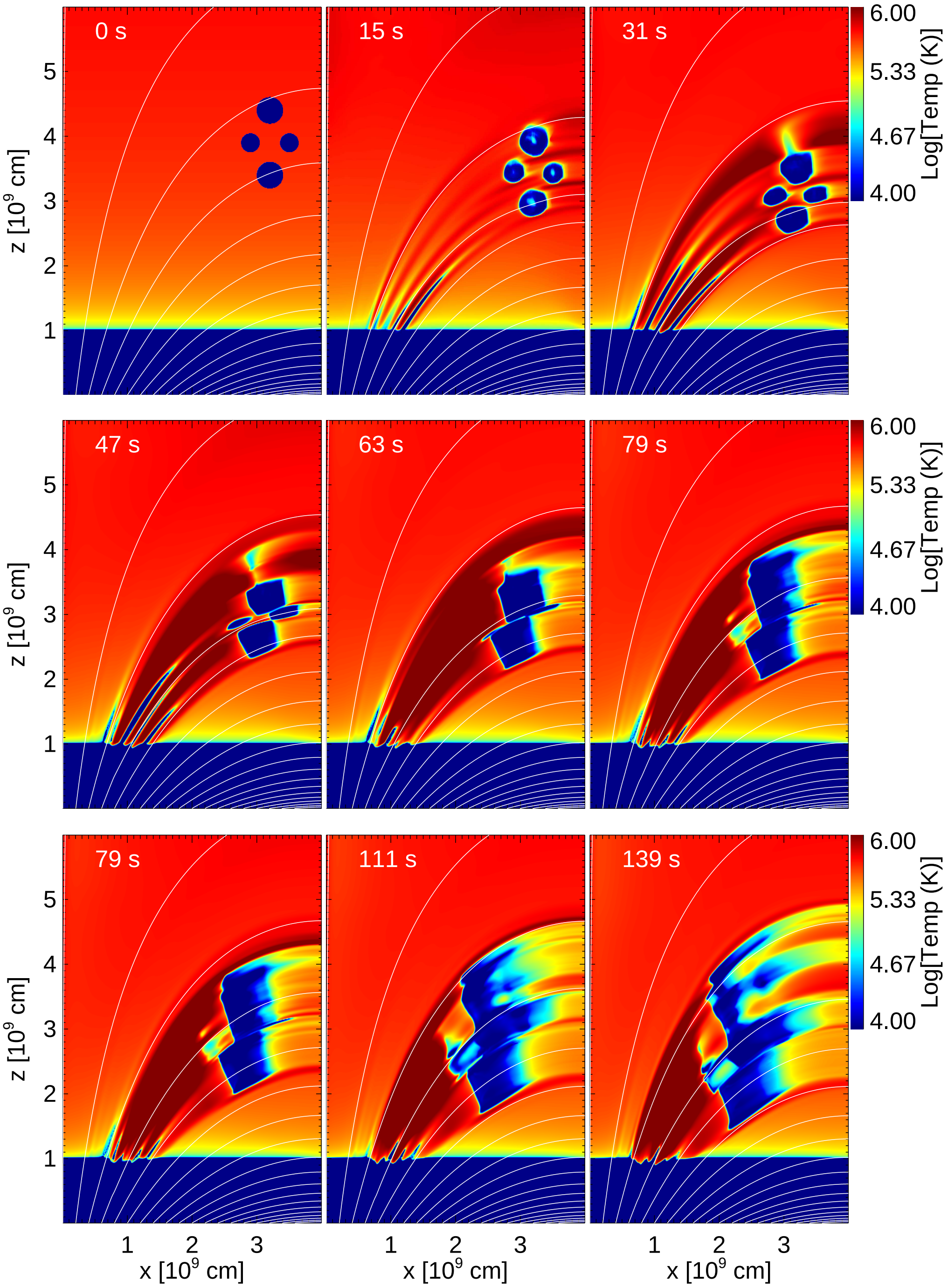

Figure 3.11: Same as in Fig. 3.5 but for the Cold Model (CM).

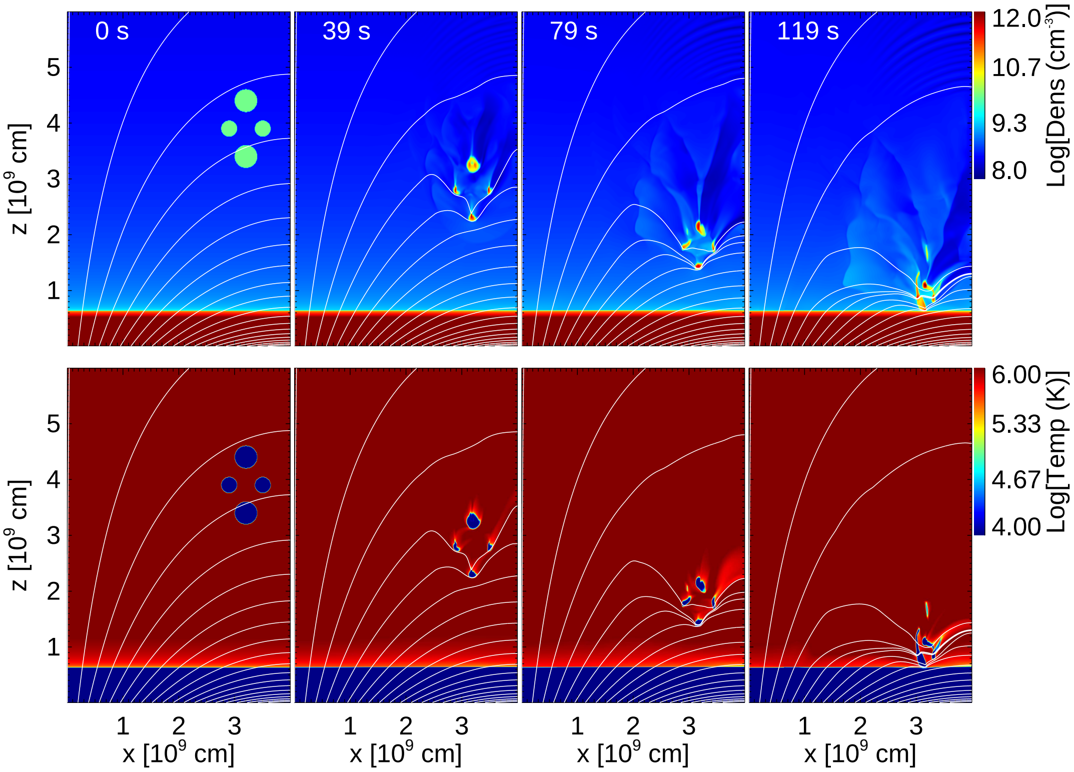

Figure 3.12: Same as in Fig. 3.4 (top panel) and Fig. 3.5 (bottom panel) but for the Weak-field Model (WM).

3.3.5 Synthetic emission

To compare the results of the simulations with the observations, from the output of the simulations, we have synthesized the emission in the AIA 171 Å channel. The filterband of this channel includes a strong Fe IX line with a temperature of maximum formation of $\sim 10^6$ K. We have calculated the emission in each cell of our 3D computational domain as

$$I_{171}(x, y, z) = G_{171}[T(x, y, z)]n_e^2(x, y, z) \tag{3.7}$$

where G_{171} is the response of the channel as a function of the temperature of the emitting plasma (available from the SolarSoftware package). Then, we have integrated $I_{171}(x, y, z)$ along two possible lines of sight, i.e., along Z and along Y. To account for absorption from optically thick plasma, we have neglected the emission from cells with a density greater than $10^{10} cm^{-3}$ (Reale et al. 2013) and beyond, along the line of sight.

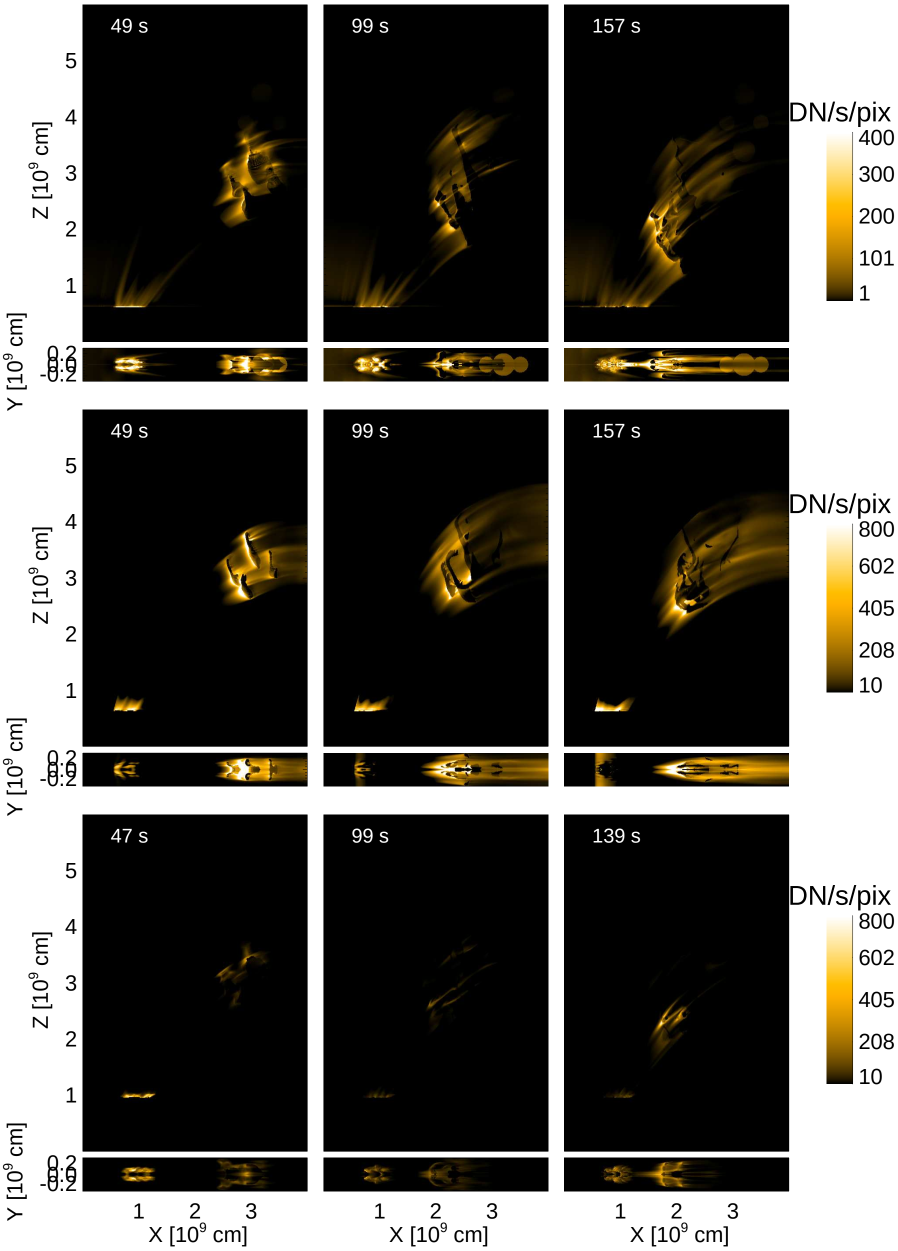

Figure 3.13: Images of the integrated emission (square root color scale) in the AIA 171 Å channel, at the labelled times from top to bottom, respectively, for RM, DM, and CM. Each panel includes both the map integrated along Y (top) and along Z (bottom).

For the DM simulation, the background atmosphere is at the same time relatively dense and hot and it fills the whole computational domain, which is much larger than the volume involved in the dynamics driven by the falling fragments. For this reason, the atmosphere is very luminous in the selected AIA channel, and, when we integrate it along the line of sight, it dominates over the emission excess produced by the fragments. Since in the observation the volume of the background atmosphere is not so large and its emission is not important for our analysis, only, for this case, we have decided to integrate only the emission through the flux-tube in which the blobs propagate.

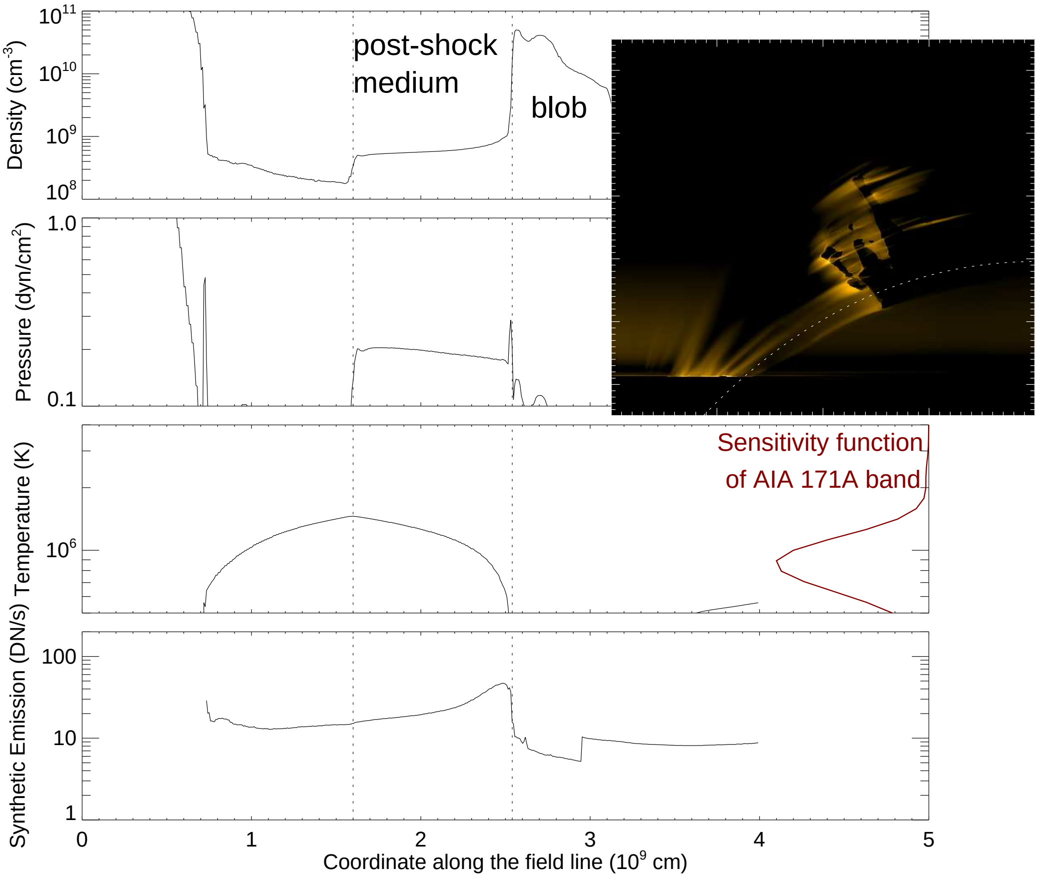

Figure 3.14: Density, temperature, pressure, and integrated emission along the white dashed line shown in the side image (which is taken at t= 100 s). The sensitivity function of the AIA 171 Å filter band is plotted (red line) on the right side of the temperature plot. The dotted vertical lines enclose the post-shock region.

Fig. 3.13 shows maps of the expected emission along both lines of sight, in a form similar to the observed ones shown in Fig. 3.1b.

In all of the models, as the blobs move, bright fronts develop ahead of them. Initially, they are thin shells just in front of the blobs, but later they extend much beyond them, in the form of elongated filaments.

To investigate where the emission comes from, in Fig. 3.14 we have related the evolution of the brightening to the dynamics by plotting density, pressure, temperature, and synthetic integrated (Y-line of sight) along a magnetic field line, at time t = 100 s, for the RM. We have selected a magnetic field line that intersects only one blob.

As shown in Fig. 3.14, the brightest emission comes from the post-shock medium ahead of the blobs. However, the high emission extends beyond the shock front down almost to the top of the chromosphere. The shock front is visible in the density profile, which is purely along the field line, but much less in the emission profile, which is integrated along the line of sight.

The shock fronts are not aligned to the line of sight, and therefore the integration along that line washes out any sharp front. The emission in the unperturbed medium beyond the shock is higher than it was initially. The reason is that the shock heats the medium in which it propagates. Therefore, a thermal front also develops, and it moves downward along the field line by pure thermal conduction. Even in the presence of saturation, we can estimate (e.g. Reale et al. 2014) that the conduction time scale over a length of $\sim 10^4$ km, a temperature ≥ 1 MK and a density of $\sim 10^8$ cm^{-3} is below 100 s, in agreement with the simulation result. As a consequence, the temperature rises up also below the shock to values in the range of higher sensitivity of the 171 Å channel. The emission in this channel therefore increases. Similar effects also occur in the other simulations (DM, CM), though with some quantitative differences.

Another interesting issue is the fact that the emission is finely structured into bright fibrils. To understand why, Fig. 3.15 compares the maps of the emission with transversal maps (YZ) of density and temperature at an X position across the filaments, i.e. across the post-shock region in front of the blobs.

The transversal maps show that the shocked medium is highly sub-structured inside the magnetic channel. For a continuous flow propagating along the field, we would expect a well defined shock-front propagating ahead of it, and therefore an emission uniformly increasing along the channel. Instead, we have four blobs that move initially not aligned to the magnetic field. As such, they are able to mix the magnetic field lines during the initial phase of the evolution, and the feedback from the field is untidy, leading to a further fragmentation similar to those typical of hydrodynamic instabilities. However, when the spatial resolution of AIA is taken into account (Fig. 3.16), these fine filaments are blurred into much thicker ones, as observed.

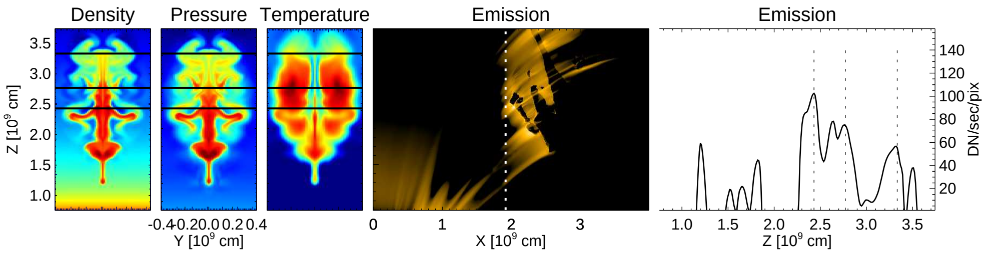

Figure 3.15: Density, pressure, and temperature (left three images) for the RM at time t = 100 s, in the plane perpendicular to that of the integrated AIA 171 Å emission (middle) passing through the dotted line, and plot of the integrated AIA 171 Å emission along the same line (right). The black lines on the left panel mark the position of the peaks in the plot on the right (dotted lines).

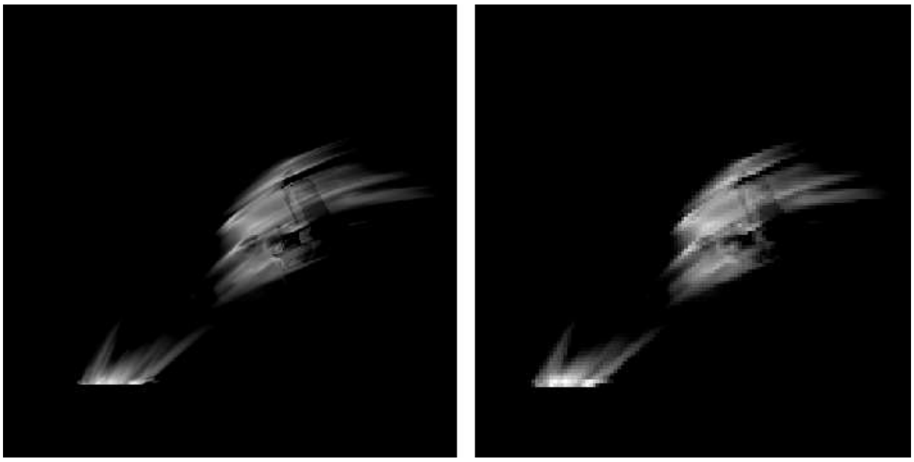

Figure 3.16: Images of the integrated emission in the AIA 171 Å channel for the CM at the full resolution of the simulation (left) and at the AIA resolution (right), at time t = 50 s.

Finally, in Fig. 3.17, we show synthetic emission profiles from simulations RM, DM, and CM to be compared with the observed ones in Fig. 3.2c. We remark that our simulations describe only the phase in which the blobs brighten the magnetic channel, which corresponds to the time and space between the dashed lines in Fig. 3.2b. As we did for the observation, we extract emission profiles along a strip, with the same width as the one marked in Fig. 3.2a. As we did for the observation, we subtracted the emission of the initial frame.

The height and shape of the profiles are different from one case to the other. In the DM, the temperature of the post-shock region exceeds the range in which the 171 Å channel is sensitive, and only a small fraction of the post-shock region near the blobs is able to emit efficiently in that band, leading to an emission with many spikes, which largely exceed the observed count rate. Instead, both in RM and CM, a larger fraction of the post-shock region emits in the channel and the emission appears to be smoother. In both cases, we also clearly see bright fronts moving to the left, i.e. to the solar surface and a growing emission when approaching the surface. The different intensity of the emission, instead, is related to the different ambient density where the shocks propagate. Overall, we find that the RM case has the best agreement with the observations, and is able to reproduce both the growing emission peak toward the end of the path and a similar DN rate.

3.4 Discussion

We studied the downfall of blobs of plasma channelled by the magnetic field toward an active region. These blobs were erupted by an M-class flare event on 7 June 2011, and showed a ballistic motion while still far from the active region. We see the blobs in absorption and we constrain their density to be around $1-2\times10^{10}$ cm^{-3}, according to the method in Landi & Reale (2013). As the interaction with the magnetic field becomes strong, they are deviated from their trajectory and channelled by a magnetic flux channel. During the channelling, the flux tube brightens in the 171 Å EUV channel of the AIA instrument, and the blobs disappear. We investigated the channelling process with the aim to explain the brightening of the magnetic channel.

We considered a model of a magnetized atmosphere with a curved topology of the magnetic field and a complete solar atmosphere from the chromosphere to the corona, and included all the physical terms of interest, in particular, gravity, radiative losses, thermal conduction along the field lines, and magnetic induction. The model solved numerically the magnetohydrodynamic equations in 3D Cartesian geometry, implemented in the PLUTO parallel code. The blobs are modelled as spheres with a downward velocity of 300 km/s not aligned with the magnetic field, different radii ($1.4-2\times10^{8}$ cm), density ($1-2\times10^{10}$ cm^{-3}), and a temperature of 10^4 K. We tested the role of the atmosphere as well as of the magnetic field by exploring an ambient atmosphere with three different ambient densities and two different

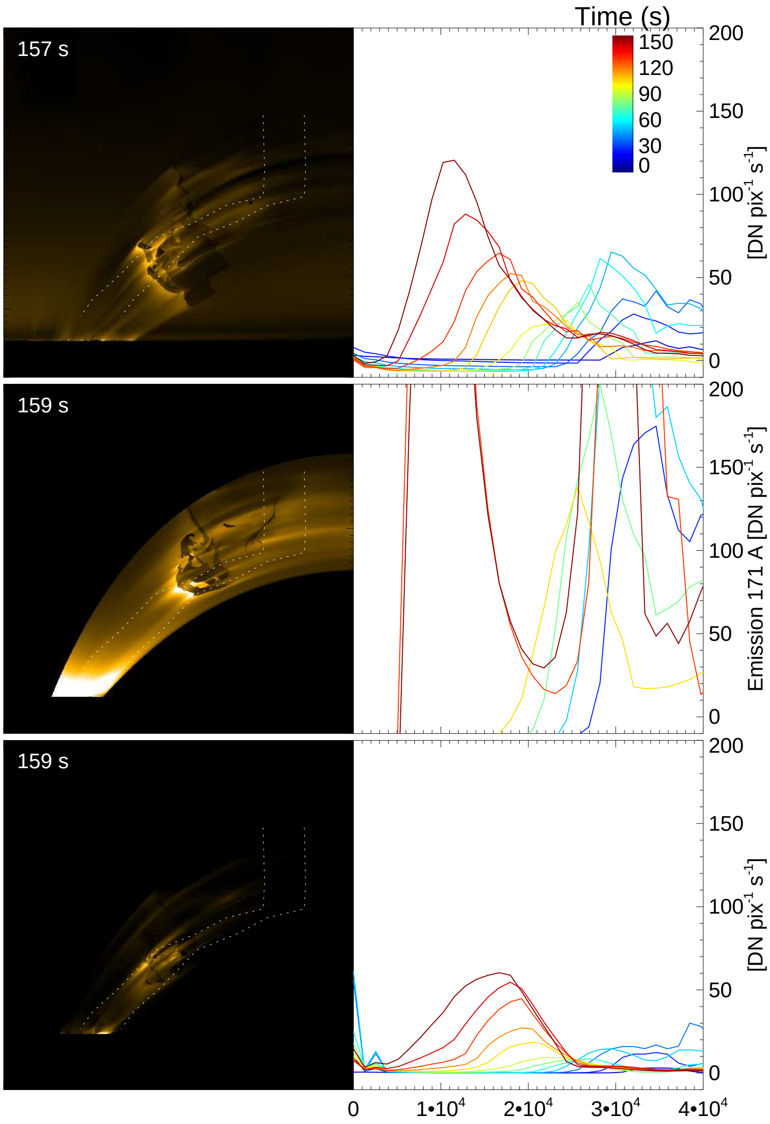

Figure 3.17: *Left*: same integrated emission images as in Fig. 3.13(top) for RM (top), DM (middle), and CM (bottom). Inside the strips (dotted lines) we compute emission profiles for comparison with the observed ones in Fig. 3.2c. *Right*: emission profiles along the strips marked in the left panels, with the same format and resolution as in the observed ones shown in Fig. 3.2c. The profiles are sampled at intervals of 12s for the RM and CM, and 24s for the DM (for the sake of clarity), at a series of times (from blue to red) to t = 150 s. The width of the strip is comparable to that in Fig. 3.2a.

magnetic field intensities, with the same topology.

The blobs started to fall vertically in all the models, but only in the case in which the magnetic field is strong (170G in the transition region and 15G at the initial blob's position) they are channelled and deviated from their trajectory. In the case of weak magnetic field, the blobs simply fall without any deviation, similar to Reale et al. (2013). This case is far from our target evolution and provides a lower limit to the conditions of the ambient magnetic field.

The initial velocity of the blobs largely exceeds the ambient sound speed, so shocks are generated. The behaviour of these shocks depends on the physical condition of the model explored, but with a common dynamics: they propagate ahead of the blobs inside the magnetic flux tube, in which the blobs are channelled, along the field lines.

Another effect of the dynamics is that the blobs are strongly deformed, even further fragmented, during their motion. Two factors contribute to this effect: (a) the field lines are untidily displaced downward and then back upward, thus being mixed and determining braiding and a differential stress on the blobs, and (b) the blobs are squashed in the direction of motion. The former effect is common to all the confined models, while the latter depends strongly on the density and pressure of the ambient atmosphere, the larger the density (pressure) the stronger the compression is, and it is also affected by the compression of the magnetic field lines in the initial stage of the evolution.

By synthesizing the emission in the 171 Å EUV band, we identified the post-shock region as the main source of the brightening ahead of the blobs. The emission depends on the density and temperature of the ambient atmosphere. The former heavily influences the intensity, because of the dependence on the square of the density, the latter acts more on the shape and size of the emission because of the narrow temperature range of channel sensitivity. As a consequence, for the simulation with high ambient density the intensity of the emission produced is too high and its profile along the field lines does not match what we observe. Instead, for the other two densities, the cooler and tenuous atmospheres give a shape and intensity that better agree with the observations, best for the one that we called RM.

The simulations show that the emission comes not only from the post-shock region, but the whole magnetic channel between the blobs, and the chromosphere is activated well before the shock arrives at the chromosphere. The reason is that the shock compresses and heats the medium it crosses, and the heat front propagates downward faster than the shock, making the unperturbed medium enter more in the AIA sensitivity range, with this assumption for ϕ for coronal condition (Orlando et al. 2005). This makes the emission contrast between the pre-shock and post-shock medium lower. More importantly, the shocks are ultimately never visible as well-defined fronts in our scenario, for another reason: each fragment or blob produces its own shock front, and, since the blobs are different and not aligned along the line of sight, the shock are also misaligned in time and space and washed out along the line of sight.

Overall, our RM provides the best match with the evolution of the channelled fragment that we selected in the observation. The parameters, i.e. size and density of the blobs that we assumed in this simulation are well within the constraints provided by the data analysis. Therefore, we obtain a self-consistent scenario. Moreover, within our limited exploration of space of the parameters, our modelling provides us with constraints on, and therefore probes, the ambient medium, and in particular on the ambient coronal magnetic field (~ 10 G) and density ($\sim 10^8$ cm^{-3}).

Several general considerations result from this study. We find that falling fragments are disrupted because of the complex interaction with a strong ambient magnetic field. The disruption occurs just when the fragments are deviated and channelled by the field. The ram pressure of the fragments differentially displaces and compresses the field lines, which react back and shuffle the blobs. Therefore, a misalignment of dense falling plasma with the local more intense magnetic field lead to a disruption of falling clouds. This evolution also becomes a signature of a strong local perturbation of the magnetic field. We considered simplified spherical blobs with homogeneous density, but in reality they can be highly inhomogeneous, thus making the mixing and fragmentation even more complex.

Regarding the emission, this study shows another mechanism that leads to an excess of emission in high energy bands. 1D/2D accretion models show higher emission due to a stationary shock produced by a continuous accretion column on the stellar surface (Orlando et al. 2010, 2013; Sacco et al. 2010). Reale et al. (2013, 2014) show that the impact of massive but isolated fragments also leads to hot brightenings. Here we show that falling fragments eventually channelled by the magnetic field do not brighten themselves, rather they activate the channel and make it bright, because of shock propagation and heating. This early further fragmentation and activation of the magnetic channel is certainly a considerable difference from the evolution studied in fragments that do not interact so strongly with the magnetic field. As described in Reale et al. (2013, 2014), in that case, the disruption of the fragments and the brightening are due exclusively to the impact on the dense chromosphere. One important implication for stellar accretion is that we might have emission excess also if the accretion flow interacts with a coronal magnetic field that is not strictly aligned to the flow, e.g. with a solar-like corona with intense active regions.

Chapter 4

Shuffling of magnetic downdrafts

In this Chapter, we study the propagation of plasma blobs inside a magnetized corona through detailed MHD modeling, either their motion is aligned or not to the magnetic field. We use the same model and code presented in the previous Chapter.

4.1 MHD Modelling

We describe the evolution of four blobs moving across a magnetized and relatively dense coronal atmosphere, with two simulations. *We compare a case in which the blobs are not fully channelled by the magnetic field to another in which they are.* We consider a typical coronal field configuration with closed arch-like lines anchored to the photosphere. This configuration has no special symmetry and a full 3D description is necessary. However, we can consider a symmetric magnetic field with respect to a plane perpendicular to the surface. Whatever the initial direction of the blobs, the field geometry and strength will prevent them from moving much across the field lines, therefore we will not need a large domain extension in that direction, which we assume to be the Y direction. To approach the configuration of a loop-populated active region but still keeping it manageable and simple, we consider a combination of magnetic dipoles, in a way that the magnetic field is symmetric with respect to the side boundaries and is closed in the low region close to the chromosphere. The computational box is three-dimensional and cartesian (X, Y, Z) and extends over 4×10^9 cm in the X direction, 1.2×10^9 cm in the Y direction and 6×10^9 cm in the Z direction. The Z direction is perpendicular to the solar surface. The mesh of the 3D domain is uniformly spaced along the three directions with $512 \times 128 \times 512$ cells, and a cell size of $\sim 80 \times 90 \times 120$ km. This provides a good compromise between resolution in all directions (the domain is larger along Z) and computational times. The blobs are sufficiently well resolved (their diameter ranges 30-40 cells) and with this resolution the initial atmosphere has been checked to be steady. In this box the ambient atmosphere is a stratified corona linked to a much denser chromosphere through a steep transition region. The corona is a hydrostatic atmosphere (Rosner et al. 1978) that extends vertically for 10^{10} cm. The chromosphere is hydrostatic and isothermal at 10^4 K and its density is $\sim 10^{16}$ cm^{-3} at the bottom. The atmosphere is plane-parallel along the vertical direction (Z). The pressure ranges between 0.29 dyn cm^{-2} at the top of the transition region and 0.12 dyn cm^{-2} at $Z = 10.5 \times 10^9$ cm. The ion density and the temperature are, respectively $\sim 2.2 \times 10^8$ cm^{-3} and $\sim 2 \times 10^6$ K at $Z = 10.5 \times 10^9$ cm. The physical parameters of the falling blobs and of the atmosphere are very similar to those of one the models listed in Chapter 3

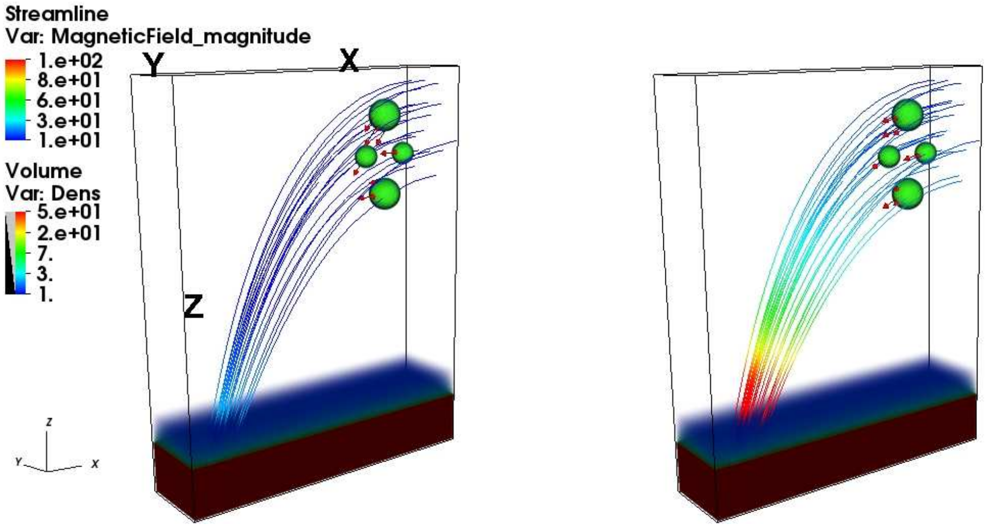

Figure 4.1: Initial conditions of the two case simulations. Rendering of the density (10^9 cm^{-3}, logarithmic scale) in which a bundle of magnetic field lines (Gauss) is shown. Blobs with initial velocity (*red arrows*) not aligned (*left*) and aligned (*right*) to the field lines.

("Dense Model"), which are constrained from the observation. The initial position of the four blobs is at a height in the range $3.5 < Z < 4.5 \times 10^9$ cm above the chromosphere, and at a distance in a range $2.5 < X < 4 \times 10^9$ cm from the left boundary side, close to the upper right corner.

Fig. 4.1 shows the initial conditions of the blobs and their initial velocity. For the sake of simplicity, we considered spherical blobs, with a radius in the range $1.4 - 2 \times 10^8$ cm, typical of those in the eruption of 7 June 2011. The temperature of the blobs is $T = 10^4$ K and their density is 10^{10} cm^{-3}. The initial temperature of the blobs is not very important because their evolution is much faster than any pressure readjustment with the ambient medium and we assume that initially they do not emit radiation. All the blobs have an initial speed of $v = 300$ km/s. In one simulation, the motion of all of them is aligned to the field. The intensity of the ambient magnetic field is ~ 170 G at the top of the transition region and $\sim$ 15 G at the initial position of the blobs. In the other simulation, the speed of the blobs is not totally aligned to the field but it lies in the XZ plane: two have a horizontal initial direction, the other two have an inclination of 45^o downwards. The magnetic field is weaker here, i.e., ~ 35 G and ~ 3 G, respectively.

Boundary conditions are reflective at the left end of the X axis, the magnetic field is forced to be perpendicular to the boundary at the right end of the X axis. For the other quantities zero gradient has been set. Fixed conditions have been set at the lower end of the Z axis, and zero gradient at the upper end, except for the magnetic field that is fixed. The same conditions are set at the far end of the Y axis. The computational domain is symmetric with respect to a plane in $Y = 0$, so we simulate half domain and set reflective conditions at the lower end of the Y axis.

4.2 The simulations

We now describe the evolution of the flowing blobs in the two different cases. We start from the propagation with an initial speed not aligned with the magnetic field. This case is more similar to those illustrated in Chapter 3, where the blobs were crossing a closed magnetic field while falling. The propagation along the field lines is presented for comparison and shows a striking qualitative difference from the other one, which is the main motivation for this work.

4.2.1 Simulation with blobs motion misaligned to the magnetic field

Fig. 4.2 shows the propagation of blobs with a motion misaligned to the magnetic field lines. The initial speed of the blobs ($v = 300$ km/s) is not far from a typical free-fall speed from large heights and larger than the local coronal sound speed ($c_s = \sqrt{\gamma p/\rho} \sim 200$ km/s), so shocks are generated immediately. These are slow mode shocks that do not perturb the magnetic field and propagate along the magnetic field lines ahead of the blobs. This was discussed in detail in Chapter 3. However, the blobs themselves do not move parallel to the the magnetic field and perturb it strongly in a few seconds. Their initial ram pressure is strong enough to drag the field lines, and force them to follow their dynamics. The ram pressure carried by the blobs is $p_{ram} = \rho v^2 \sim 20$ dyn cm^{-2}, much larger than the field pressure $B^2/8\pi \sim 0.3$ dyn cm^{-2}; the magnetic tension gives the field enough stiffness to channel the blobs. The net effect is that the motion of the blobs produces a tailspin that travels along the field lines. Measuring the distance and time taken to arrive at the chromosphere, the speed of this perturbation is ~ 700 km/s. The perturbation is an Alfvén wave that moves ahead of the blobs at an average Alfvén speed ($v_A = B/\sqrt{4\pi\rho}$) in a medium with density 7×10^8 cm^{-3} and magnetic field ~ 10 Gauss. These look as reasonable average conditions for the medium where the perturbation is propagating. No MHD instabilities develop, the magnetic field is strong enough to suppress them (see Appendix B). While dragging the field lines, the misaligned and

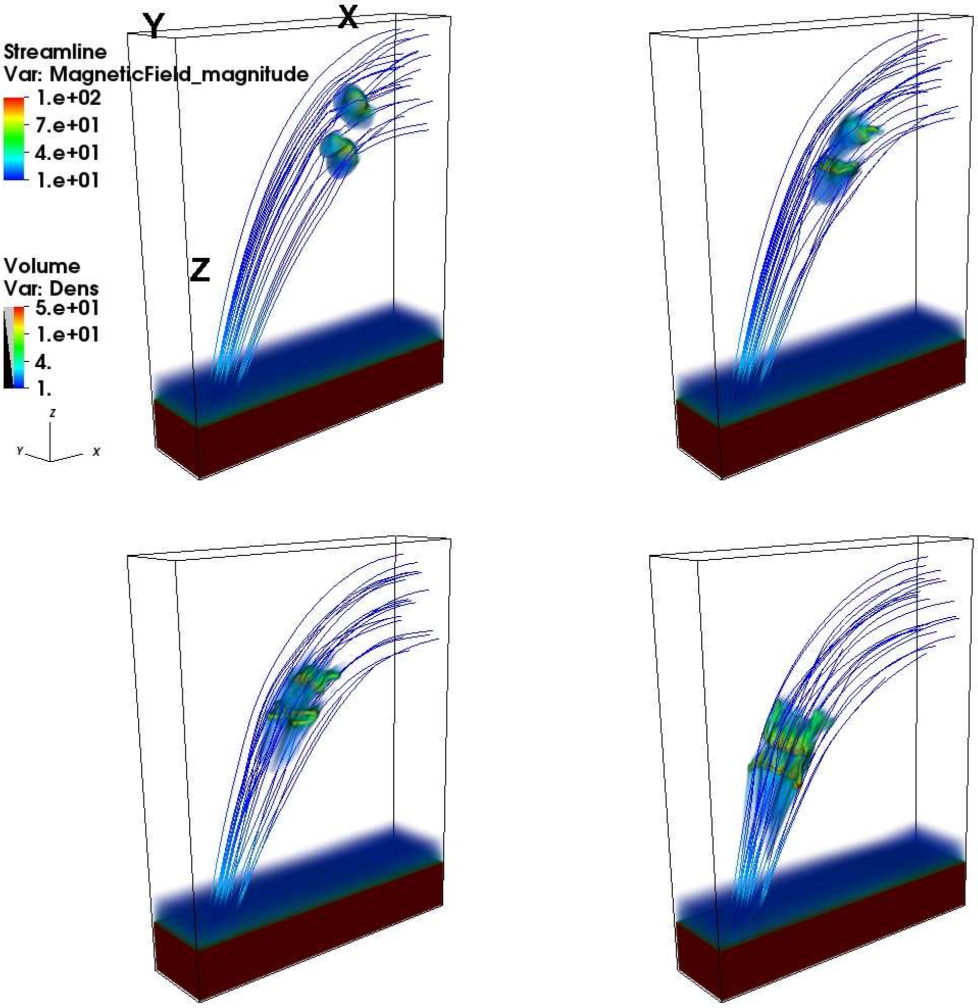

Figure 4.2: Simulation of blobs with initial velocity not aligned to the field lines: Rendering of the density at times t=20,40,60,100s as in Fig. 4.1.

non-uniform motion of the blobs mixes them, and, as metal chords, they soon have a feedback on the blobs mixing them in turn. As a result, they rapidly lose their initial shape and even their single identity. They first form two separate conglomerates in the initial 30s, which travel along the tube. These are progressively squashed and elongated into a waterfall-like shape and in about 2 minutes they practically coalesce into a single blurred and filamented cloud, as shown in Fig. 4.2. In the meantime, they still flow along the magnetic tube toward the chromosphere. Also the return wave from the chromosphere contributes to further disrupt and mix the downflowing cloud.

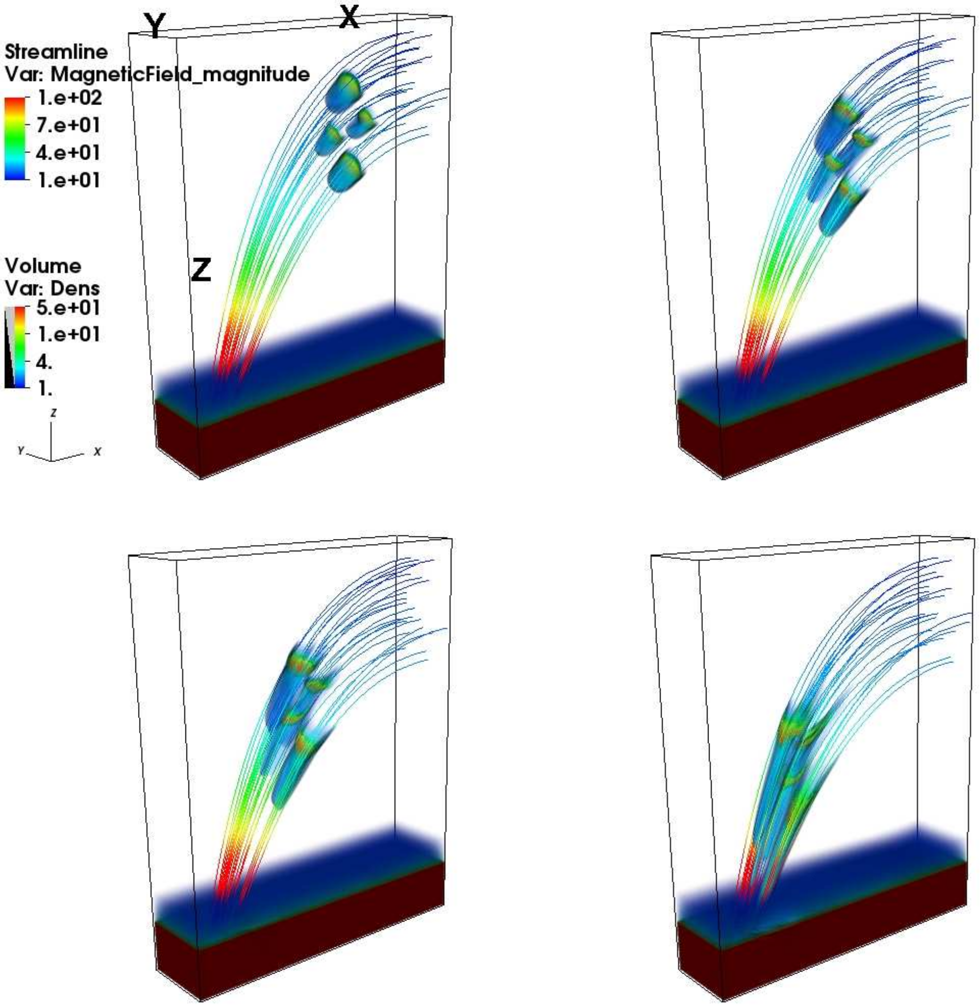

Figure 4.3: Same as Fig. 4.2 but for the simulation of blobs with initial velocity aligned to the field lines.

At the end of the shuffling, the identity of the blob is completely lost, what remains is a highly inhomogeneous flow structured into filaments that move untidily along the field lines until they hit the surface in ~ 200s.

We have checked that we obtain a similar evolution both for blobs with diverging velocities and for a single blob with an initial speed not aligned to the magnetic field lines, i.e. the blobs are shuffled by the field and are disrupted.

4.2.2 Comparison with motion aligned to the magnetic field

Fig. 4.3 shows the propagation of blobs with a motion that is initially strictly aligned to the magnetic field lines. The velocity and the atmosphere conditions are equal to the previous case, so the generation and propagation of the slow mode shocks are the same: once they are generated, they propagate along the magnetic field lines. In this case, the magnetic field intensity is five times greater than in the previous case, thus the magnetic field efficiently channels the blobs, by suppressing any component perpendicular to the field lines, and it is not perturbed significantly. The blobs simply flow along the magnetic field lines as well as the slow mode shocks. No magnetic perturbation mixes the blobs, and they remain compact during the motion. Their shape varies only because the magnetic channel changes its cross-section and direction along the propagation. The blobs do not merge and therefore do not lose their identity during the propagation, as clearly shown in Fig. 4.3. Fig. 4.4 emphasises the difference between the evolution of the misaligned and aligned motions. It shows cross-sections of two density maps (Figs.4.2 and 4.3) in vertical YZ planes. The images are taken at slightly different times, i.e., $t = 100$ s and 90 s, respectively, when the blobs are located approximately in the same Z range (the velocity component along the field lines is slightly different in the two cases). The two panels of this figure show very clearly how different is the evolution: a single but structured cloud versus three distant and separate blobs.

4.3 Discussion

In this work we study how different can be the propagation of fast plasma fragments flowing parallel to a coronal magnetic field from others flowing with a tilted direction, through detailed 3D MHD modeling. Here we use the same model as in Chapter 3 to describe the propagation of dense and cold blobs of plasma moving in a magnetized and complete solar atmosphere (including both the chromosphere and the corona). The model includes the effect of the gravity, radiative losses, thermal conduction along the field lines, and magnetic induction. We use the PLUTO parallel code to solve numerically the magneto-hydrodynamic equations in 3D Cartesian geometry.

We compare two similar simulations of blobs flowing inside a magnetic field anchored in the solar surface. In one, their motion is fully channelled by the magnetic field, in the other it is only partially, because of the initial direction of the motion and of the intensity of the field. The evolution that

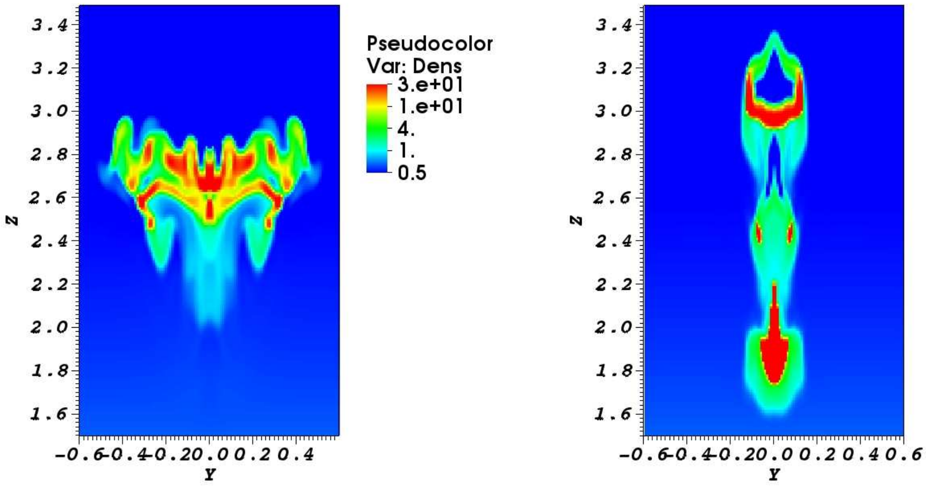

Figure 4.4: Density (10^9 cm^{-3}, logarithmic scale) in a plane YZ across the blobs in the case of misaligned blob's motion (left panel) at $t = 100$ s, and in case of aligned blob's motion (right panel) at t=90s.

we find is strikingly different. In the fully aligned case, the blobs and the slow mode shocks flow along the field lines and do not perturb the intense magnetic field. The blobs remain compact and move, as well as for the shocks, inside independent magnetic channels. In the misaligned case, the shuffling of the field lines driven by the blobs has a feedback on the blobs themselves and mixes them, and the shocks as well. At the same time, the conglomeration is structured into thinner filaments. In this case it is impossible to establish what was the native channel or their initial shape, they lose completely their identity. Misaligned propagation is also an efficient way to excite fast Alfvén wave fronts, which travel ahead of the cloud.

In summary, this work highlights the possible back-effect of the confining magnetic field on the propagation of fragmented flows inside it. If they are perfectly channelled, plasma fragments keep their identity as single blobs with no mixing, and the magnetic is left unchanged as well. If there is some misalignment, the magnetic field can react with a shuffling of the field lines that mixes and merges the fragments, thus changing completely the plasma configuration.

This represents a very effective mechanism of plasma mixing in the presence of a magnetic field, different from standard shear-like instabilities. The field lines can be effectively shuffled by irregular plasma motion and its feedback to the plasma is naturally untidy. One may wonder which is the most usual situation, whether aligned or misaligned fragment motion. We expect that if the plasma is confined since the beginning and the magnetic field does not change much along the track, e.g., coronal rain, the motion should be mostly aligned to the field. On the other hand, downfalling from large distances through a significantly changing magnetic field might result into misaligned fragment motion. Such kind of situation may occur in the accretion onto young protostars from circumstellar disks, both at the flow origin (disk) and close to the flow impact, where the magnetic field of the star might become very complex. This process might therefore lead to further mixing of downflows and to increase their fine substructuring.

Chapter 5

Guided flows in coronal loops

In this Chapter, we address the possible role of the initial alignment or misalignment of a continuous flow with respect to the field lines by studying the dynamics of a flow of plasma along magnetic flux tubes in a coronal atmosphere. We use the same model and code presented in the previous Chapters.

The idea to investigate this issue in continuous flows has been suggested by recent solar EUV observations (Fig. 5.1). The material ejected by a solar eruption fell into the solar surface in thin and elongated strands of dark material and it ends up in a row configuration near the impact region. There is no clear explanation to this morphology but the work presented in the previous chapters suggest that the magnetic field can play an important role in determining the dynamics.

We address this issue by modelling flows which are pushed upward from the chromosphere along closed magnetic flux tubes in the corona by means of a 3D-MHD model that is able to capture all the physics behind the process and to take into account other important effects, such as the natural expansion of the magnetic channel cross section with the height and its effect on the dynamics, or possible transversal motions of the flow. We use the same model and numerical code used for the work presented in the previous chapters (see also Appendix A for information on the PLUTO code).

5.1 The Model

We study a flow injected upwards and confined into a closed coronal magnetic flux tube. We consider two slightly different flow directions, one perfectly aligned to the field and the other slightly inclined with respect to the field lines. This recalls closely the dynamics of the siphon flows (Chapter 1). We will call the former 'Aligned Flow' and the latter 'Misaligned Flow'.

The closed magnetic loop has been obtained by setting a single dipole magnetic field (see Chapter 2) centered on the solar surface. The misaligned flow propagates in the quasi semi-circular flux tube that has a distance between the footpoint $\sim 4 \times 10^9$cm and a height of 2.5×10^9cm above the chromosphere. The field intensity is ~ 30G at the top of the chromosphere and rapidly decreasing with the height (Fig. 5.2). The field confines the flow but can be perturbed by it, indeed the ratio between the ram pressure carried by the flow and the magnetic pressure is $\frac{\rho v^2}{B^2/8\pi} \sim 0.7$ at the top of the transition region. This might be typical of an active region loop. We consider the same ambient atmosphere as the 'Dense Model' described in Chapter 3, that combined to the field intensity gives an Alfvén speed of ~ 2000 km/s at the top of the chromosphere close to the footpoint of the loop.

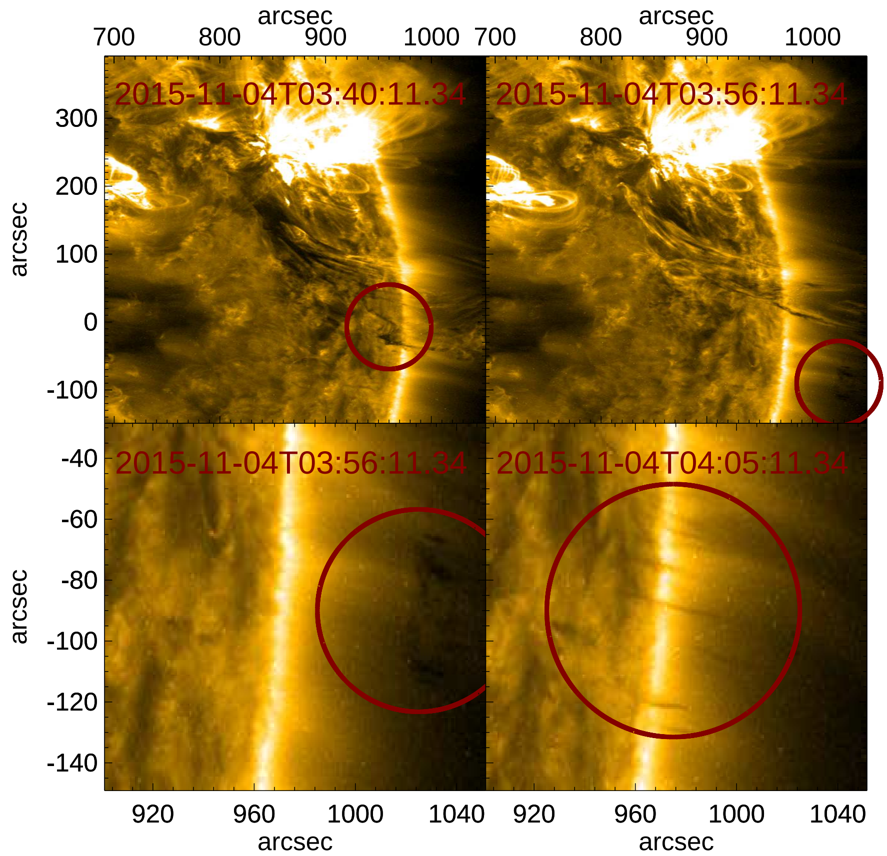

Figure 5.1: Images of the evolution of the falling material in the 171 Åband of the SDO/AIA instrument, in which the red circles mark the material position (http://www.lmsal.com/hek/her?cmd=view-voevent&ivorn=ivo://helio-informatics.org/ERMET_KarelSchrijver_20151105_214937).

The flow is injected upwards from a localized area of the chromosphere. It is modelled as a cylinder with a radius R of 2×10^8cm, a height of 10^9cm, with homogeneous density and temperature of, respectively, $3 \times 10^{10}\text{cm}^{-3}$ and 4×10^4K. Since the thickness of the chromosphere is $\approx 7 \times 10^8$ cm, the tip of the jet protrudes in the corona already from the beginning.

The velocity of the flow is uniform along the Z direction $v = 200$km/s in a circular area with radius $R = 10^8$cm, and then linearly decreasing to zero outside this shell (Fig. 5.3), to a radius $R = 2 \times 10^8$cm. This initial velocity is such that the misaligned flow has enough kinetic energy to reach and surpass the apex of the flux tube. The aligned flow is injected at a distance $X = 0.9 \times 10^9$cm from the left boundary, where the magnetic field lines are nearly open and thus vertical because closer to the magnetic pole and aligned with the vertical direction of the flow. This flow will propagate much higher along a flux tube (Fig. 5.3). The misaligned flow is injected at a distance $X = 1.3 \times 10^9$cm from the left boundary where the magnetic field lines rapidly curve and leads to a misalignment of the flow.

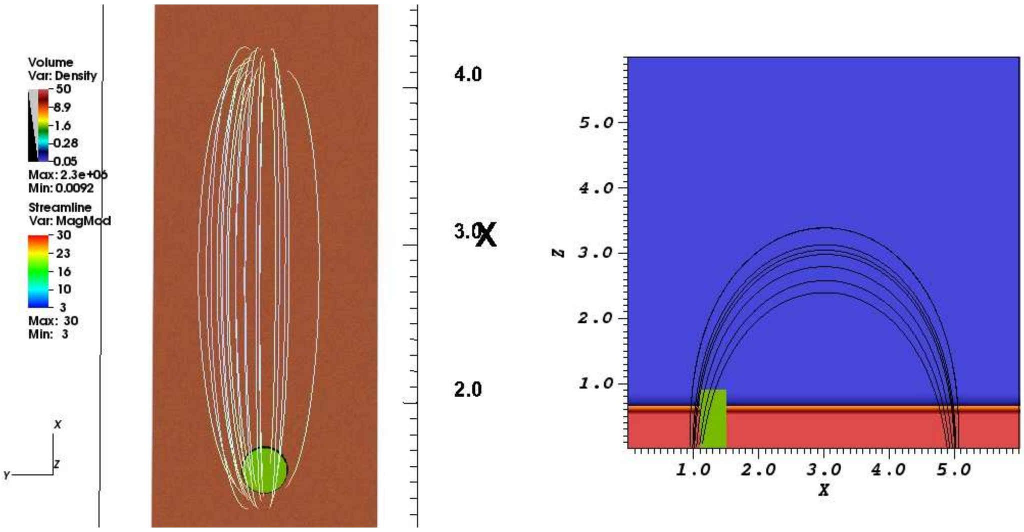

Figure 5.2: Initial condition of the model in the misaligned flow. Rendering of the density (2×10^{10}cm^{-3}, logarithmic scale) viewed from above in the Z axis (left panel) and density map in the central frame of the domain, i.e. a XZ plane (right panel). A bundle of magnetic field lines is shown.

The computational box is three-dimensional and Cartesian (X, Y, Z) and extends over 6×10^9 cm in the X direction, 1×10^9cm in the Y direction and 6×10^9 cm in the Z direction, that is perpendicular to the solar surface. The mesh of the 3D domain is adaptively refined to strong gradient of density. The roughest level has $120 \times 20 \times 120$ number of cells and it is refined up to 3 levels. Each level refines locally the mesh by a factor of two, giving a cell size of $\sim$ 60 km at the higher level of refinement. The geometry of the system is symmetric with respect to the $Y = 0$ plane, allowing us to simulate only a half of the domain by imposing reflecting condition at the slice boundary. The magnetic field is fixed at all other boundaries while, for the other physical variables, we impose outflow conditions in all other boundaries except for that one located at the bottom of the chromosphere (i.e. at the beginning of Z axis), where we impose fixed conditions and zero velocity outside the flow, and inflow condition for the flow.

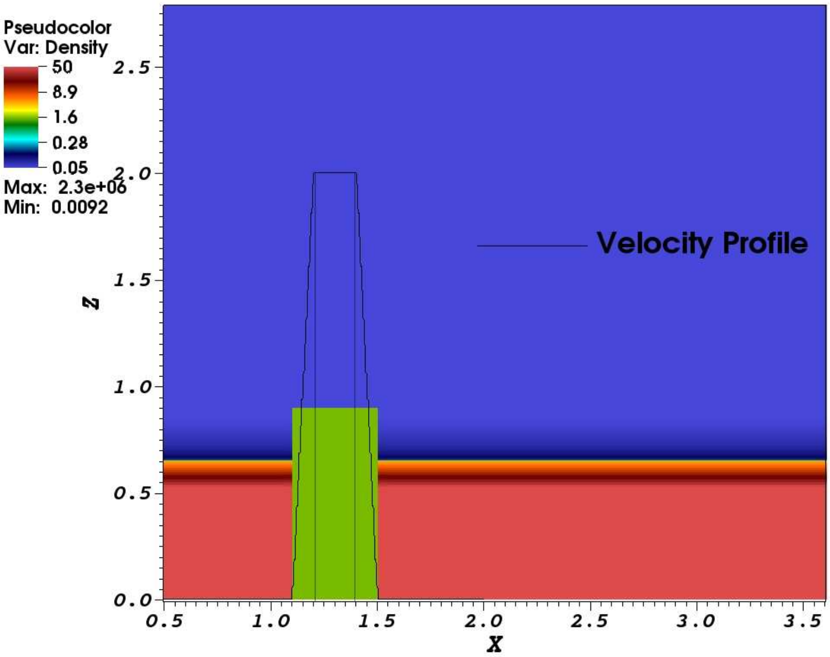

Figure 5.3: Same density map as in Fig. 5.2 in which we show the initial profile of the velocity of the flow.

5.2 Results

5.2.1 The aligned flow

Fig. 5.4 shows four snapshots of the evolution of the aligned flow. The flow propagates in a flux tube that is almost vertical at the injection site; therefore, it reaches a maximum height and eventually falls back onto the chromosphere.

The jet is initially uniform along the vertical direction, while the surrounding atmosphere is not. So the flow is not in pressure equilibrium with the ambient atmosphere: it has an overpressure at its tip, but at the lower boundary, the ambient chromosphere is very dense, and the thermal pressure ($p_{chrom} > 10^4$ dyn cm^{-2}) is much larger than inside the flow ($p_{flow} \sim 10^{-1}$ dyn cm^{-2}, $p_{mag} \sim 4 \times 10^2$ dyn cm^{-2}). Therefore, at its origin, both the flow and the magnetic field inside it are rapidly squeezed by the outside pressure and the injection of the flow is totally suppressed after $\sim$ 40s of evolution.

Since the initial speed of the flow (v_{flow} = 200km/s) exceeds the sound speed ($c_s = \sqrt{\gamma \frac{2K_bT}{\mu m_p}} \sim 150$km/s, with $T \sim 10^6$K), a shock is generated and moves ahead of the flow with the same dynamics as described in Chapter 3 and in Chapter 4 (see subsection 5.2.2 for an estimation of the shock velocity).

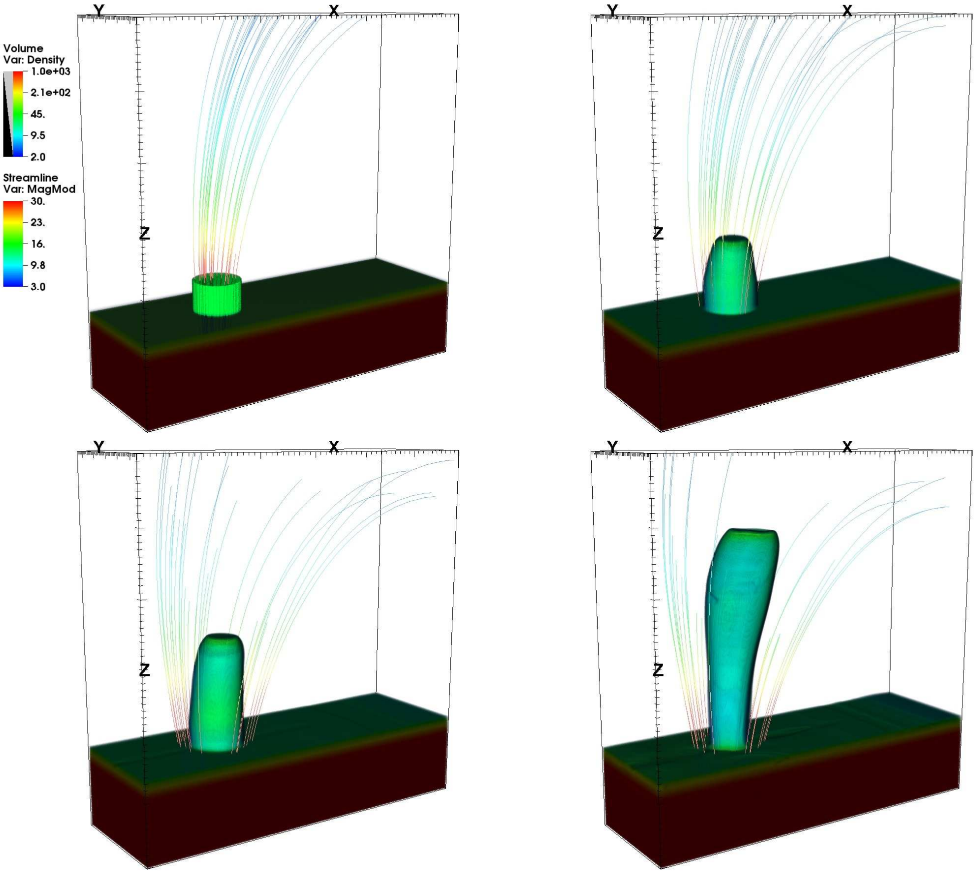

Figure 5.4: Simulation of the aligned flow: Rendering of the density (10^9cm^{-3}, logarithmic scale) at times t=0, 20, 40, 100s in which a bundle of magnetic field lines are shown.

The flow moves upwards without deviating from the initial direction and as a uniform cylinder. Since its thermal pressure is much greater than that of the surrounding corona, the flow expands and pushes apart the magnetic field where it propagates. However, the magnetic field is tightly anchored at the footpoint of the flux tube and its expansion rapidly stops (with Alfvénic time scales) and the tension constrains back the flow. As a result, a thin shell of overdense plasma forms all around the head of the flow, as shown in Fig. 5.9 and Fig. 5.10, which is progressively smoothed out. Overall, the flow keeps its uniformity and cylindrical symmetry while it propagates upwards.

5.2.2 The misaligned flow

We present some snapshots of the flow evolution in Figs.5.5-5.7. Although overall the flow still moves along the magnetic flux tube, the detailed evolution is very different from the one of the strictly aligned flow. Again a shock is again generated and moves ahead of the flow along the tube and the injection is quenched from below.

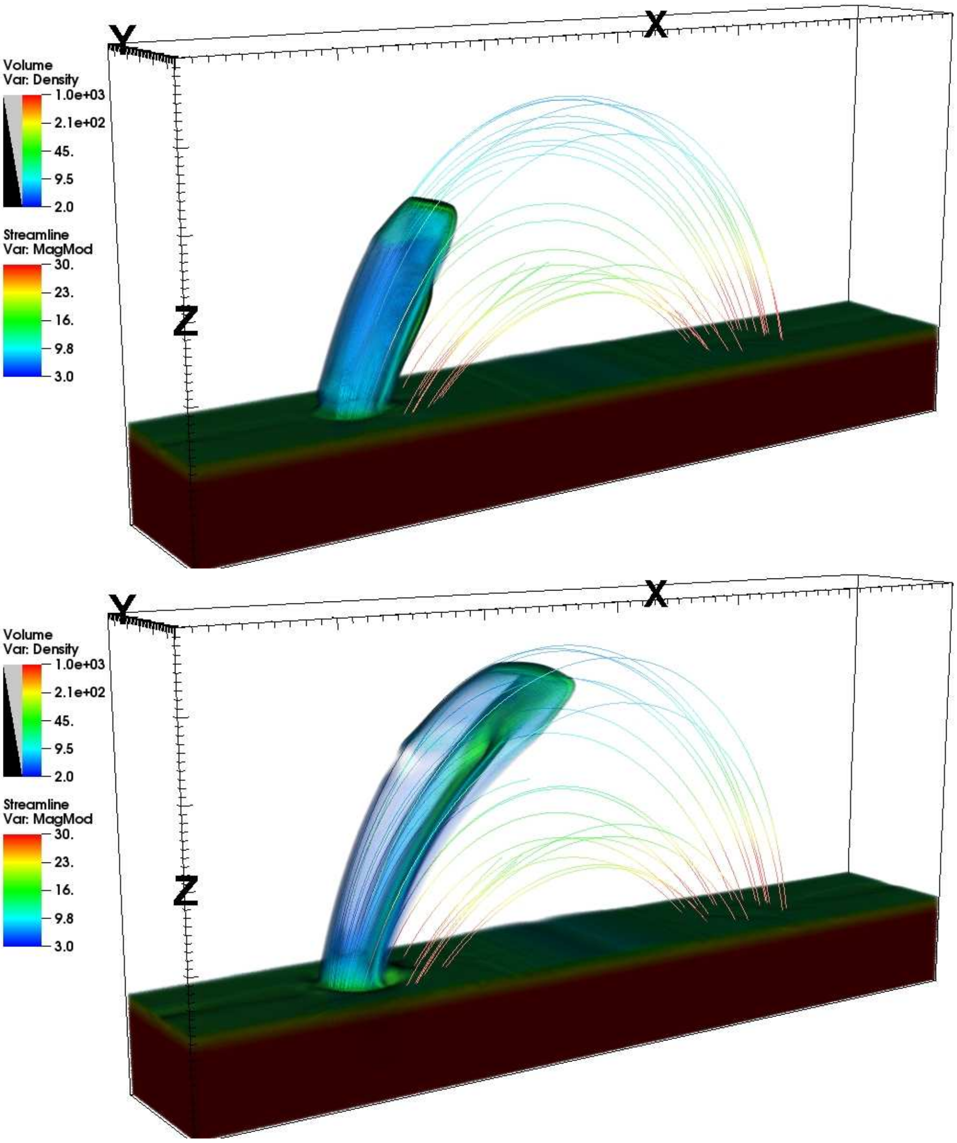

Figure 5.5: Simulation of the flow in the misaligned flow: Rendering of the density (10^9cm^{-3}, logarithmic scale) at times t=80, 160s in which a bundle of magnetic field lines is shown.

Since the flux tube curves back to the chromosphere, the shock hits the other foot-point of the magnetic channel, at t=260s (when the flow has just crossed the apex of the magnetic channel). Its average speed is therefore $v_{sh} \sim 220\text{km/s}$.

Already at the beginning, the velocity of the flow has a small component perpendicular to the magnetic field. This component determines a deformation of the field above the chromosphere. The flux tube still expands, but the expansion is no longer symmetric.

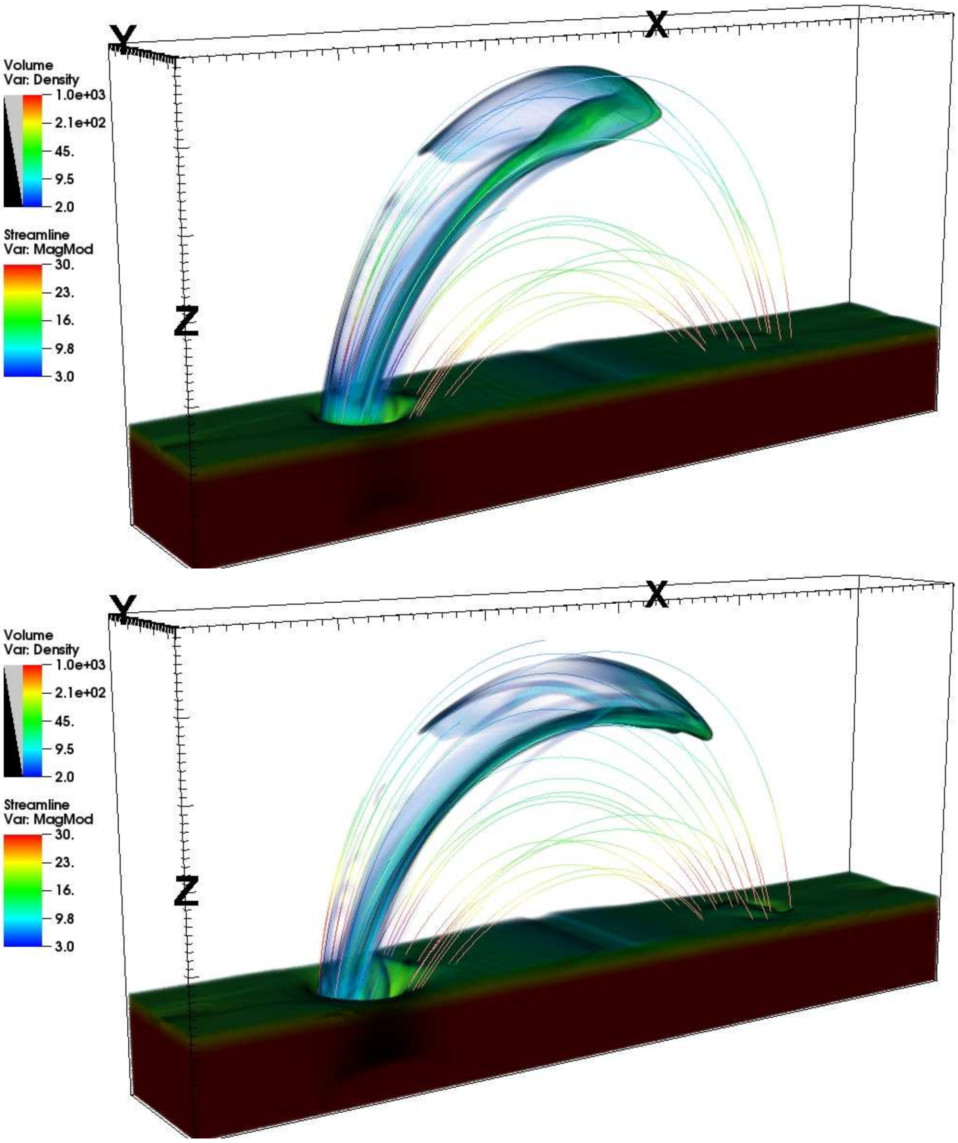

Figure 5.6: Same as for Fig. 5.5 but at times t=240, 320s.

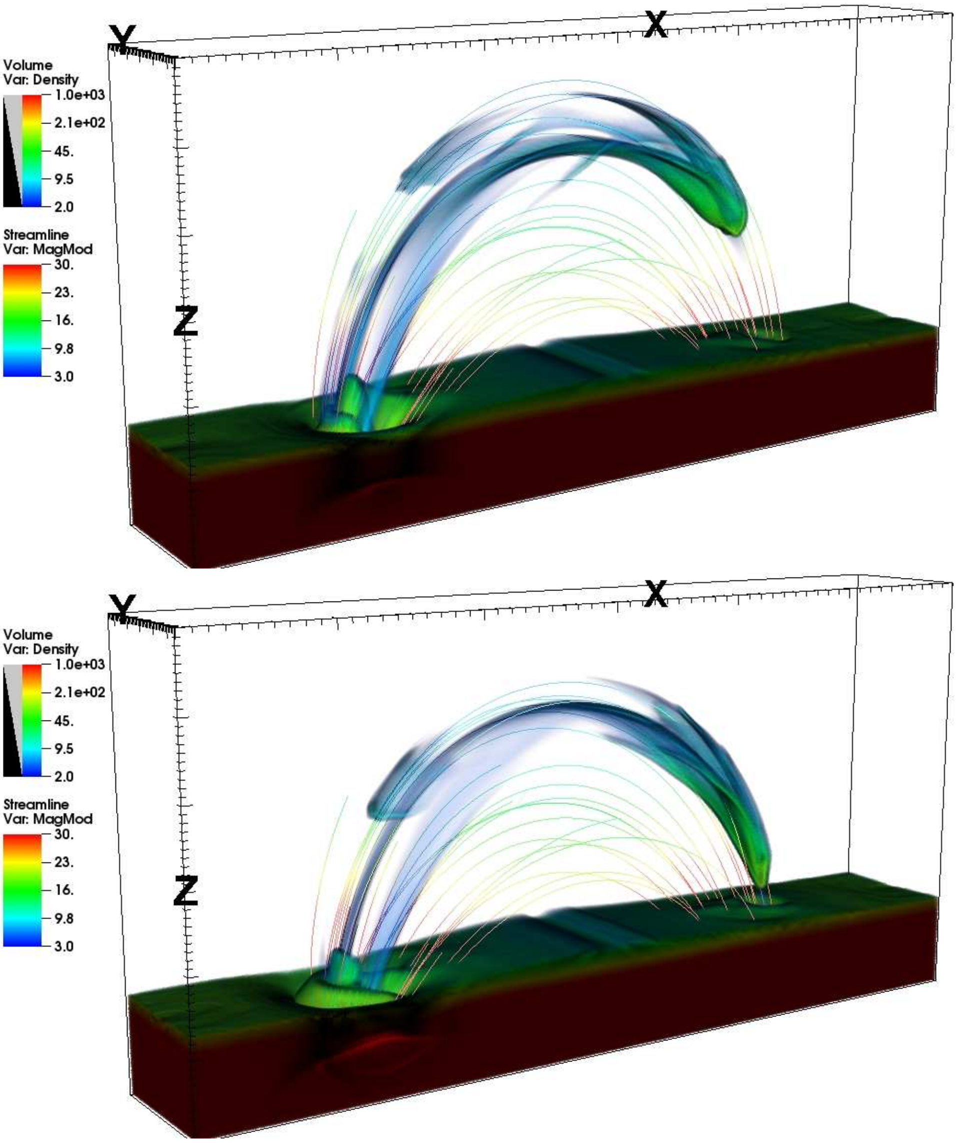

Figure 5.7: Same as for Fig. 5.5 but at times t=400, 480s

However, the deformation of the field causes a substantial deviation of the flow toward the tube curvature, already at $t = 20$s, as we can see in Fig. 5.9. Since the dense plasma is forced to flow in a direction different from the initial one, its structure becomes asymmetric. It converges and thus is squashed on the side of the curvature, where the magnetic field offers more resistance to deformation.

The interplay between the magnetic back-effects (magnetic pressure and tension) and the upward push of the flow is very strong until the flow reaches

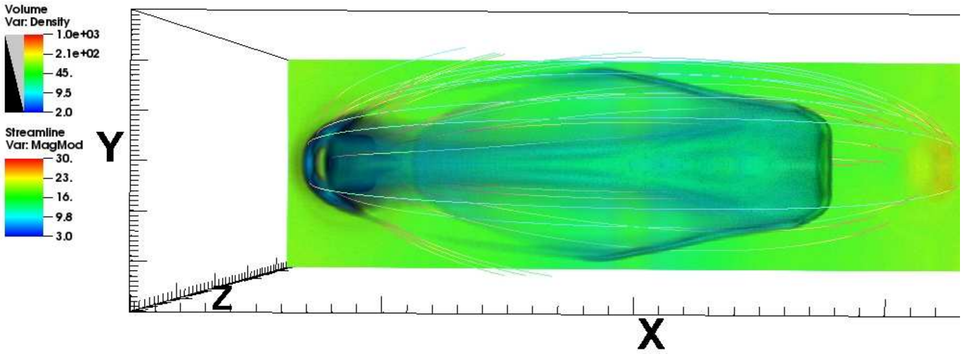

Figure 5.8: Simulation of the misaligned flow: top view of the density rendering (10^9cm^{-3}, logarithmic scale) at times t=320s in which a bundle of magnetic field lines is shown.

the apex of the magnetic channel at $t \sim 200$ s. After this time, the magnetic field starts to relax to the initial configuration while the flow falls on the other side the magnetic channel. The relaxation of the field lines acts as a press that flattens the flux tube and deforms the flow inside it even more. The flow expands laterally at $t \sim 320$ s (Fig. 5.8). The relaxation of the field is untidy and frays the flow. Due to this effect, as the flow moves along the tube, it splits becoming highly sub-structured at the end of the evolution at $t \sim 480$s (Fig. 5.7).

Overall, we observe that an initially cylindrical and uniform flow becomes laminar and filamentary basically as an effect of the initial misalignment of its direction to the field lines.

Fig. 5.9 and Fig. 5.10 compare density maps in different cross-sections at early times and emphasize the difference between the symmetric structure of the aligned flow and the strong bending of the misaligned flow. Fig. 5.10 shows how the thin dense shell all around the aligned flow is squashed all on the side of the curved field in the misaligned flow and eventually determines the laminar structure of the flow.

5.3 Discussion

In this Chapter, we use the same 3D MHD model presented in the previous chapters to analyse the dynamics of a continuous flow perfectly or not perfectly aligned to the field lines of a magnetic channel anchored to the solar surface. We can draw some preliminary considerations.

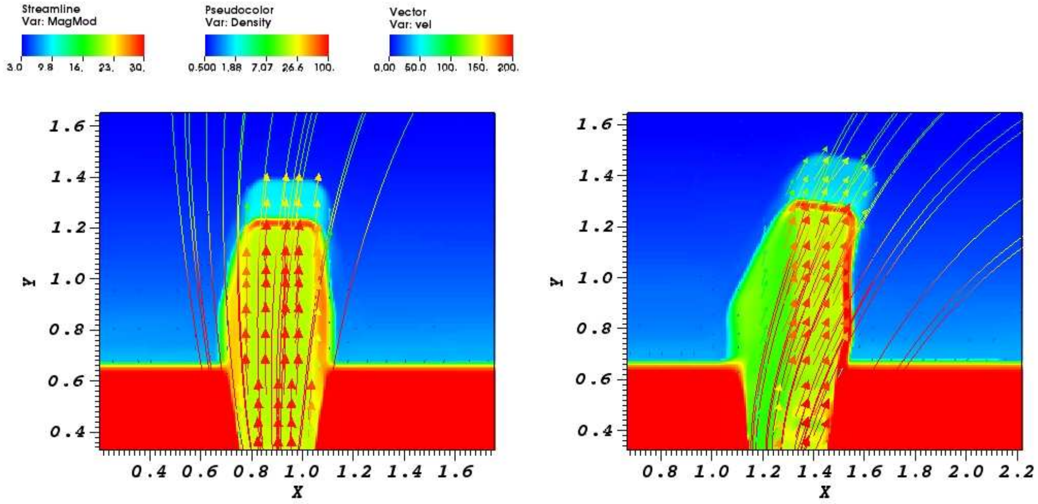

Figure 5.9: Density maps (10^9cm^{-3}, logarithmic scale) for the aligned (left) and for the misaligned flow (right) in which we show a bundle of magnetic field lines and the velocity field. They are XZ planes at $t = 20$s.

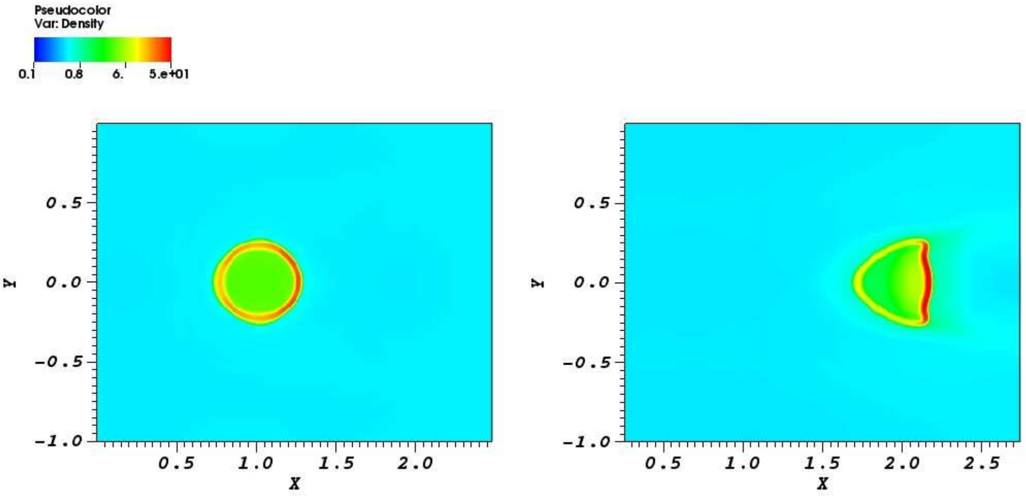

Figure 5.10: Density maps (10^9cm^{-3}, logarithmic scale) for the aligned (left) and for the misaligned flow (right). They are XY planes taken at $t = 100$s and at $Z = 2 \times 10^9$cm.

Summarizing, we find that the aligned flow travels mostly unperturbed along the magnetic channel, except for some expansion at the tip and for the formation of a dense outer shell. If instead the field lines are strongly curved and the flow is forced to change its direction to follow the magnetic channel, the evolution is significantly different. Because of the stiffness of the field, the flow is squashed to the side of the curved lines and converts into a dense laminar flow, strikingly different from the symmetric dense shell found when the alignment is perfect. As the flow travels through regions of weaker field, it causes some deformation of the field and its untidy back-reaction makes the flow split. The evolution has been described until the flow hits the chromosphere at the other side of the closed channel.

We expect that the result can somewhat change for different conditions in the model, but are unable to quantify without a relevant exploration of the parameter space. For instance, we might expect that a weaker field and/or a more tenuous ambient atmosphere should make the flow expansion easier and perhaps smooth down the dense shell of the aligned flow. A faster outflow in the curved loop should determine a stronger deformation of the field and we might expect an even larger backreaction and flow splitting.

The transformation of the initially cylindrical, symmetric and uniform flow into a strongly laminar and substructured one might explain the puzzling evidence of hedge-like downfalls observed with SDO/AIA. We might be simply in the presence of a relatively long-fed flow that is not launched in the direction of the local magnetic field, probably not particularly strong, and therefore considerably deviated by the field during its journey. A simple estimate of the ambient and flow conditions might confirm this hypothesis.

The results we found are general and could be applied to many flows moving in a magnetized medium: if the flow motion is not aligned to the magnetic field, the flow tends to be flattened and split by the deviation of the direction of motion. If the alignment is nearly perfect the flow simply travels along the field lines, without significant deformations, as expected for plasma strictly confined in magnetic coronal loops.

Chapter 6

Conclusions

In this thesis, we studied the propagation of cold and dense plasma in a magnetized medium. Our starting point was the observation of a spectacular eruption in June 2011 in which many dense fragments fell back on the solar surface far from the eruption site. Our target here was to study the fragments channelled by the magnetic field in the neighbourhood of active regions. We explored different dynamics, a series of downfalling blobs of plasma channelled by the magnetic field but also a continuous flow both propagating inside a closed magnetic structure in which they can be aligned or not to the field. We have built a fully three dimensional MagnetoHydroDynamic model that includes the physical process needed for a complete and exhaustive description of the plasma dynamics such as the thermal conduction, radiative losses, gravity and the magnetic induction.

In Chapter 3, we studied the downfall of fragments of plasma from the high corona to an active region. The observation showed that when the falling fragments approach the active region magnetic field, they are deviated, they fade and the deviating magnetic channel brightens before they reach its footpoint. The simulations showed that while the falling fragments are deviated and channelled by the field, they are disrupted. We found that the ram pressure of the fragments displaces and compresses differentially the field lines, which react back and shuffle the blobs, causing their disruption and explaining their fading. Their motion produces shocks that propagates ahead of the blobs along the field lines. These shocks brighten the entire magnetic channel ahead the blobs and before the blobs impact the loop foot-point as we see in the observation.

In Chapter 4, we investigated the key conditions that determine a significant disruption of the blobs. We compared two different falling dynamics. Either the blob's motion is perfectly aligned to an intense magnetic field or it is misaligned to a weaker field and the blobs are able to perturb it. We found that the blobs flowing along the field lines maintain their shape and therefore their identity, otherwise the blobs motion mixes the magnetic field lines that shuffle back the blobs.

In Chapter 5, we extended the study of the aligned/misaligned dynamics to continuous flows pushed upwards from the chromosphere into closed coronal magnetic structures. As preliminary results, we found that the flows moving strictly along the field lines are largely left unchanged. Instead, misaligned flows are squashed to the inside of the curved magnetic structure and become laminar and eventually also filamented by the untidy restoring of the perturbed magnetic field.

In summary, our model allowed us to capture the relevant properties and to provide us with a coherent and complete view of the dynamics of flows propagating in a magnetized medium. Moreover, we caught the new opportunities offered by a fully 3D MHD model with high resolution coupled to the access to huge HPC resources (e.g., Marconi/CINECA and Pleiadies/NASA) to highlight plasma perturbation mechanisms unexplored to our knowledge, and alternative to other well-known MHD instabilities.

As future developments, we consider to examine more in depth the nature and the cause of the filamentation, to add the radiative transfer in order to better describe the interaction with the lower atmosphere (the chromosphere), and to include more realistic initial conditions by studying the formation of the blobs from their initiation, e.g. the solar eruption.

As a perspective, our results might be of interest in a wide range of astrophysics and plasma physics applications, whenever the flow is able to perturb the magnetic field and the field is strong enough to react back. They can be relevant for any magnetized flows both confined and outgoing in the Solar Corona (e.g., eruptions, coronal rain, coronal mass ejections, siphon flows), but also for accretion flows or outgoing jets in forming stars, where the role of channelling magnetic field is increasingly acknowledged. This work can also be framed in the perspective of future achievements. The forthcoming Solar Orbiter and Solar Probe missions will put great effort in the study of the interaction of solar transients (e.g., CME) and of the variability of the outer interplanetary magnetic field, by means of in-situ measurements and of remote-sensing, and any information about the detailed structure and evolution of plasma outstreaming in the magnetized heliosphere will be important.

Appendix A

The PLUTO astrophysical code

A.1 The code

The PLUTO code (Mignone et al. 2007, 2012) is a modular Godunov-type code intended mainly for astrophysical applications and high Mach number flows in multiple spatial dimensions. The code embeds different hydrodynamic modules and multiple algorithms, providing a flexible and versatile modular computational framework, to solve the equations describing Newtonian, relativistic, MHD, or relativistic MHD fluids in Cartesian or curvilinear coordinates. The code has been developed at the Turin Astronomical Observatory in collaboration with the Department of General Physics of the Turin University (contact information of the main code developer: mignone@ph.unito.it). The code is freely available at http://plutocode.ph.unito.it under the GNU general public license.

PLUTO is entirely written in the C programming language and was designed to make efficient use of massive parallel computers using the message-passing interface (MPI) library for interprocessor communications. PLUTO can output data using the parallel HDF5 output (IO) library to simplify and manage the output of large amounts of data. The code has been ported to, and extensively tested with, different machines and operating systems, including Linux, Windows/Cygwin, Power Mac G5, Beowulf clusters, IBM SP4/SP5/SP6 /BCX/CLX, SGI Irix, IBM BluGene/P and others. The code is available to the scientific community since 2007 and was largely used in different context in astrophysics, from solar and stellar coronae, to supernova remnants, and to protostellar and extragalactic jets. Our group collaborates with the PLUTO developers to apply extensively the code to astrophysical environments (e.g. Orlando et al. 2011).

A.2 The Magneto-hydrodynamic module

PLUTO solves the magnetohydrodynamic (MHD) equations for an ideal compressible plasma, described in Chapter 2, in the following conservative form:

$$\frac{\partial \rho}{\partial t} + \nabla \cdot (\rho \mathbf{v}) = 0 \tag{A.1}$$

$$\frac{\partial \rho \mathbf{v}}{\partial t} + \nabla \cdot (\rho \mathbf{v}\mathbf{v} - \mathbf{B}\mathbf{B} + p_t \mathbf{I}) = \rho \mathbf{g} \tag{A.2}$$

$$\frac{\partial E}{\partial t} + \nabla \cdot ((E + p_t)\mathbf{v} - \mathbf{B}(\mathbf{v} \cdot \mathbf{B})) = \rho \mathbf{v} \cdot \mathbf{g} - n_e n_H \Lambda(T) + H - \nabla \cdot \mathbf{F}_c \tag{A.3}$$

$$\frac{\partial \mathbf{B}}{\partial t} + \nabla \cdot (\mathbf{v}\mathbf{B} - \mathbf{B}\mathbf{v}) = 0 \tag{A.4}$$

$$\nabla \cdot \mathbf{B} = 0, \tag{A.5}$$

where

$$\rho = \mu m_H n_H \tag{A.6}$$

$$p_t = p + \frac{\mathbf{B} \cdot \mathbf{B}}{2} \tag{A.7}$$

$$E = \rho\epsilon + \rho\frac{\mathbf{v} \cdot \mathbf{v}}{2} + \frac{\mathbf{B} \cdot \mathbf{B}}{2} \tag{A.8}$$

$$\mathbf{F}_c = \frac{F_{sat}}{F_{sat} + |\mathbf{F}_{class}|}\mathbf{F}_{class} \tag{A.9}$$

$$\mathbf{F}_{class} = k_{\parallel}\mathbf{b}(\mathbf{b} \cdot \nabla T) + k_{\perp}(\nabla T - \mathbf{b}(\mathbf{b} \cdot \nabla T)) \tag{A.10}$$

$$|\mathbf{F}_{class}| = \sqrt{(\mathbf{b} \cdot \nabla T)^2(k_{\parallel}^2 - k_{\perp}^2) + k_{\perp}^2 \nabla T^2} \tag{A.11}$$

$$F_{sat} = 5\Phi\rho c_s^3 \tag{A.12}$$

where ρ is the density per unit mass, $\mu = 1.265$ is the mean atomic mass (assuming solar metal abundances; Anders & Grevesse 1989), m_H is the mass of the hydrogen atom, n_e and n_H are, respectively, the electron and hydrogen number density, p_t is the total pressure, that is, the sum of the thermal pressure p and the magnetic pressure (the factor $1/\sqrt{4\pi}$ is absorbed in the definition of the magnetic field $\mathbf{B}$), E is the total energy density, that is, the sum of the thermal energy density ($\rho\epsilon$), the kinetic energy density and the magnetic energy, $\mathbf{v}$ is the plasma velocity, $\mathbf{g} = g_{\odot}\hat{\mathbf{z}}$ is the solar gravity, $\hat{\mathbf{z}}$ is the unit vector along the vertical direction, $\mathbf{I}$ is the identity tensor, T is the temperature, $\Lambda(T)$ is the radiative loss function for optically thin plasma, $\mathbf{F}_c$ is an anisotropic (i.e. along the magnetic field lines) flux-limited expression that varies between the classical and saturated thermal conduction regimes $\mathbf{F}_{class}$ and F_{sat} respectively, $k_{\parallel} = K_{\parallel}T^{5/2}$ and $k_{\perp} = K_{\perp}\rho^2/(B^2T^{1/2})$ are thermal conduction coefficients along and across the magnetic field, $K_{\parallel}$ and $K_{\perp}$ are constants, $\mathbf{b}$ is the magnetic unit vector, H is the heating function whose only role is to keep the unperturbed atmosphere in energy equilibrium, suppressed for $T < 10^4$ K, c_s is the sound speed for an isothermal plasma, Φ is a free parameter (< 1, Giuliani 1984) that determines the degree of saturation of the thermal conduction; we set $\Phi = 0.9$, which corresponds to quite an efficient conduction, more typical of coronal conditions (Cowie & McKee 1977). This set of equations is completed by the equation of state for an ideal gas:

$$p = (\gamma - 1)\rho\epsilon \tag{A.13}$$

where $\gamma = 5/3$ is the adiabatic index.

Appendix B

MHD shear instabilities

In this appendix, we estimate the length scale of two MHD instabilities that can arise where the dynamics involves two fluids at different density: Kelvin-Helmoltz and Rayleigh-Taylor instabilities. The estimates have been done for the model presented in Chapter 4, but similar results can be obtained for the other cases presented in the other chapters, because they share similar physical parameters.

B.1 Kelvin-Helmoltz instability

When a heavier fluid (blobs) in motion is sustained against a lighter fluid (the corona) by the magnetic field, Kelvin-Helmoltz instabilities can arise. They are suppressed when the magnetic field is strong enough to satisfy the condition (Priest 2014, and references therein)

$$\frac{B_-^2 + B_+^2}{4\pi \rho_- \rho_+} (\rho_- + \rho_+) \geq (U_- - U_+)^2 \tag{B.1}$$

where subscripts $-$ and $+$ denote the variables inside and outside the blobs, respectively, B is the magnetic field, ρ is the mass density, and U is the velocity.

In the misaligned case, the blob density ($n_b \approx 10^{10}\mathrm{cm}^{-3}$) is much higher than the coronal ambient density ($n_c \approx 3 \times 10^8$ cm^{-3}), the magnetic field intensity is ~ 3 G and does not change much at the interface of blob and corona, the ambient medium is static, Equation B.1 can be simplified to

$$\frac{2B^2}{4\pi n_b \mu m_H} \geq U^2 \tag{B.2}$$

where μm_H is the mean atomic mass. We obtain $3 \times 10^{15} > 10^{15}$, and an even larger difference for the aligned blobs where the magnetic field is 25 times more intense than in the misaligned case. In our simulations Kelvin-Helmoltz instabilities are therefore efficiently suppressed by the magnetic field.

B.2 Rayleigh-Taylor instability

The high ratio between the density of the blobs and the ambient corona could make the separation of the blob-to-corona layer subject to the Rayleigh-Taylor instability. The wave vector of such perturbations is smaller than a critical threshold given by (Priest 2014, and references therein)

$$k < k_c = \frac{4\pi \left(\rho_+ - \rho_-\right) g_\odot}{2B^2} \tag{B.3}$$

with subscripts as in Eq.B.1 and $g_\odot$ is the solar gravity. This critical value leads to a lower limit for the characteristic length of the perturbation, which we estimated to be $L_c = 2\pi/k_c > 10^{11}$ cm, for the misaligned case. This is much larger than the size of the blobs.

Bibliography

Alfvén, H. 1942, Nature, 150, 405

Anders, E. & Grevesse, N. 1989, Geochim. Cosmochim. Acta, 53, 197

Antolin, P. & Rouppe van der Voort, L. 2012, Astrophysical Journal, 745, 152

Antolin, P., Vissers, G., Pereira, T. M. D., Rouppe van der Voort, L., & Scullion, E. 2015, Astrophysical Journal, 806, 81

Ardila, D. R., Basri, G., Walter, F. M., Valenti, J. A., & Johns-Krull, C. M. 2002, Astrophysical Journal, 566, 1100

Argiroffi, C., Flaccomio, E., Bouvier, J., et al. 2011, Astronomy and Astrophysics, 530, A1

Argiroffi, C., Maggio, A., & Peres, G. 2007, Astronomy and Astrophysics, 465, L5

Athay, R. G. & Holzer, T. E. 1982, Astrophysical Journal, 255, 743

Beckers, J. M. 1968, Solar Physics, 3, 367

Bertout, C., Basri, G., & Bouvier, J. 1988, Astrophysical Journal, 330, 350

Brekke, P., Kjeldseth-Moe, O., & Harrison, R. A. 1997, Solar Physics, 175, 511

Brickhouse, N. S., Cranmer, S. R., Dupree, A. K., Luna, G. J. M., & Wolk, S. 2010, Astrophysical Journal, 710, 1835

Calvet, N. & Gullbring, E. 1998, Astrophysical Journal, 509, 802

Cargill, P. J. & Priest, E. R. 1980, Solar Physics, 65, 251

Carlyle, J., Williams, D. R., van Driel-Gesztelyi, L., et al. 2014, Astrophysical Journal, 782, 87

Chen, F. F. 1984, Journal of the British Astronomical Association, 95, 45

Chen, P. F. 2011, Living Reviews in Solar Physics, 8, 1

Colombo, S., Orlando, S., Peres, G., Argiroffi, C., & Reale, F. 2016, Astronomy and Astrophysics, 594, A93

Cowie, L. L. & McKee, C. F. 1977, Astrophysical Journal, 211, 135

De Pontieu, B., Hansteen, V. H., Rouppe van der Voort, L., van Noort, M., & Carlsson, M. 2007, Astrophysical Journal, 655, 624

de Pontieu, B., McIntosh, S., Hansteen, V. H., et al. 2007, Publications Astronomy Society Japan, 59, S655

De Pontieu, B., McIntosh, S. W., Carlsson, M., et al. 2011, Science, 331, 55

De Pontieu, B., McIntosh, S. W., Hansteen, V. H., & Schrijver, C. J. 2009, Astrophysical Journal, 701, L1

Dere, K. P. 2009, Astronomy and Astrophysics, 497, 287

Dolei, S., Bemporad, A., & Spadaro, D. 2014, Astronomy and Astrophysics, 562, A74

Doyle, J. G., Taroyan, Y., Ishak, B., Madjarska, M. S., & Bradshaw, S. J. 2006, Astronomy and Astrophysics, 452, 1075

Dupree, A. K., Brickhouse, N. S., Cranmer, S. R., et al. 2012, Astrophysical Journal, 750, 73

Edwards, S., Hartigan, P., Ghandour, L., & Andrulis, C. 1994, Astronomical Journal, 108

Fang, X., Xia, C., Keppens, R., & Van Doorsselaere, T. 2015, Astrophysical Journal, 807, 142

Field, G. B. 1965, Astrophysical Journal, 142, 531

Finn, J. M., Guzdar, P. N., & Usikov, D. 1994, Astrophysical Journal, 427, 475

Giuliani, Jr., J. L. 1984, Astrophysical Journal, 277, 605

Gullbring, E. 1994, Astronomy and Astrophysics, 287, 131

Gullbring, E., Calvet, N., Muzerolle, J., & Hartmann, L. 2000, Astrophysical Journal, 544, 927

Günther, H. M., Liefke, C., Schmitt, J. H. M. M., Robrade, J., & Ness, J.-U. 2006, Astronomy and Astrophysics, 459, L29

Hansteen, V. H., De Pontieu, B., Rouppe van der Voort, L., van Noort, M., & Carlsson, M. 2006, Astrophysical Journal, 647, L73

Herczeg, G. J., Walter, F. M., Linsky, J. L., et al. 2005, Astronomical Journal, 129, 2777

Huenemoerder, D. P., Kastner, J. H., Testa, P., Schulz, N. S., & Weintraub, D. A. 2007, Astrophysical Journal, 671, 592

Innes, D. E., Cameron, R. H., Fletcher, L., Inhester, B., & Solanki, S. K. 2012, Astronomy and Astrophysics, 540, L10

Johns-Krull, C. M., Valenti, J. A., & Koresko, C. 1999, Astrophysical Journal, 516, 900

Kastner, J. H., Huenemoerder, D. P., Schulz, N. S., Canizares, C. R., & Weintraub, D. A. 2002, Astrophysical Journal, 567, 434

Keenan, F. P., Thomas, R. J., Neupert, W. M., et al. 1996, MNRAS, 278, 773

Kleint, L., Antolin, P., Tian, H., et al. 2014, Astrophysical Journal, 789, L42

Klimchuk, J. A. 2012, Journal of Geophysical Research (Space Physics), 117, 12102

Kohl, J. L., Noci, G., Cranmer, S. R., & Raymond, J. C. 2006, The Astronomy and Astrophysics Review, 13, 31

Koldoba, A. V., Ustyugova, G. V., Romanova, M. M., & Lovelace, R. V. E. 2008, MNRAS, 388, 357

Lamzin, S. A. 1998, Astronomy Reports, 42, 322

Landi, E., Del Zanna, G., Young, P. R., Dere, K. P., & Mason, H. E. 2012, Astrophysical Journal, 744, 99

Landi, E., Raymond, J. C., Miralles, M. P., & Hara, H. 2010, Astrophysical Journal, 711, 75

Landi, E. & Reale, F. 2013, Astrophysical Journal, 772, 71

Langangen, Ø., Carlsson, M., Rouppe van der Voort, L., & Stein, R. F. 2007, Astrophysical Journal, 655, 615

Lemen, J. R., Title, A. M., Akin, D. J., et al. 2012, Solar Physics, 275, 17

Mackay, D. H., Longbottom, A. W., & Priest, E. R. 1999, Solar Physics, 185, 87

Madjarska, M. S., Vanninathan, K., & Doyle, J. G. 2011, Astronomy and Astrophysics, 532, L1

Mariska, J. T. & Dowdy, Jr., J. F. 1992, Astrophysical Journal, 401, 754

Matsakos, T., Chièze, J.-P., Stehlé, C., et al. 2013, Astronomy and Astrophysics, 557, A69

Mignone, A., Bodo, G., Massaglia, S., et al. 2007, Astrophysical Journal, 170, 228

Mignone, A., Zanni, C., Tzeferacos, P., et al. 2012, Astrophysical Journal, 198, 7

Orlando, S., Bonito, R., Argiroffi, C., et al. 2013, Astronomy and Astrophysics, 559, A127

Orlando, S. & Peres, G. 1999, Physics and Chemistry of the Earth C, 24, 401

Orlando, S., Peres, G., Reale, F., et al. 2005, Astronomy and Astrophysics, 444, 505

Orlando, S., Peres, G., & Serio, S. 1995a, Astronomy and Astrophysics, 294, 861

Orlando, S., Peres, G., & Serio, S. 1995b, Astronomy and Astrophysics, 300, 549

Orlando, S., Sacco, G. G., Argiroffi, C., et al. 2010, Astronomy and Astrophysics, 510, A71

Parker, E. N. 1953, Astrophysical Journal, 117, 431

Patsourakos, S., Klimchuk, J. A., & Young, P. R. 2014, Astrophysical Journal, 781, 58

Peres, G., Spadaro, D., & Noci, G. 1992, Astrophysical Journal, 389, 777

Pesnell, W. D., Thompson, B. J., & Chamberlin, P. C. 2012, Solar Physics, 275, 3

Petralia, A., Reale, F., & Orlando, S. 2017, Astronomy and Astrophysics, 598, L8

Petralia, A., Reale, F., Orlando, S., & Klimchuk, J. A. 2014, Astronomy and Astrophysics, 567, A70

Petralia, A., Reale, F., Orlando, S., & Testa, P. 2016, Astrophysical Journal, 832, 2

Pneuman, G. W. & Kopp, R. A. 1978, Solar Physics, 57, 49

Priest, E. 2014, Magnetohydrodynamics of the Sun

Reale, F. 2014, Living Reviews in Solar Physics, 11, 4

Reale, F., Orlando, S., Testa, P., Landi, E., & Schrijver, C. J. 2014, Astrophysical Journal, 797, L5

Reale, F., Orlando, S., Testa, P., et al. 2013, Science, 341, 251

Robrade, J. & Schmitt, J. H. M. M. 2007, Astronomy and Astrophysics, 473, 229

Rosner, R., Tucker, W. H., & Vaiana, G. S. 1978, Astrophysical Journal, 220, 643

Rueedi, I., Solanki, S. K., & Rabin, D. 1992, Astronomy and Astrophysics, 261, L21

Sacco, G. G., Argiroffi, C., Orlando, S., et al. 2008, Astronomy and Astrophysics, 491, L17

Sacco, G. G., Orlando, S., Argiroffi, C., et al. 2010, Astronomy and Astrophysics, 522, A55

Schmitt, J. H. M. M., Robrade, J., Ness, J.-U., Favata, F., & Stelzer, B. 2005, Astronomy and Astrophysics, 432, L35

Spitzer, L. 1962, Physics of Fully Ionized Gases

Telleschi, A., Güdel, M., Briggs, K. R., Audard, M., & Scelsi, L. 2007, Astronomy and Astrophysics, 468, 443

Teriaca, L., Banerjee, D., Falchi, A., Doyle, J. G., & Madjarska, M. S. 2004, Astronomy and Astrophysics, 427, 1065

Testa, P., Drake, J. J., & Peres, G. 2004, Astrophysical Journal, 617, 508

Tripathi, D. & Klimchuk, J. A. 2013, Astrophysical Journal, 779, 1

Tsiropoula, G. & Tziotziou, K. 2004, Astronomy and Astrophysics, 424, 279

Uchida, Y. & Shibata, K. 1984, Publications Astronomy Society Japan, 36, 105

Valenti, J. A. & Johns-Krull, C. M. 2004, Astrophysics and Space Science, 292, 619

van Driel-Gesztelyi, L., Baker, D., Török, T., et al. 2014, Astrophysical Journal, 788, 85

Vanninathan, K., Madjarska, M. S., Scullion, E., & Doyle, J. G. 2012, Solar Physics, 280, 425

Webb, D. F. & Howard, T. A. 2012, Living Reviews in Solar Physics, 9, 3

Winebarger, A. R., DeLuca, E. E., & Golub, L. 2001, Astrophysical Journal, 553, L81

Winebarger, A. R., Warren, H., van Ballegooijen, A., DeLuca, E. E., & Golub, L. 2002, Astrophysical Journal, 567, L89

Xia, C. & Keppens, R. 2016, ArXiv e-prints

Xia, C., Keppens, R., Antolin, P., & Porth, O. 2014, Astrophysical Journal, 792, L38